Fakultät für Maschinenwesen

Lehrstuhl für Aerodynamik und Strömungsmechanik

# Numerical investigation of leukocyte binding in the human vasculature

Babak Gholami

Vollständiger Abdruck der von der Fakultät für Maschinenwesen der Technischen Universität München zur Erlangung des akademischen Grades eines

Doktor-Ingenieurs

genehmigten Dissertation.

| | |
|---|---|
| Vorsitzender: | Prof. Dr. Oliver Lieleg |
| Prüfer der Dissertation: | |
| | 1. Prof. Dr.-Ing. Nikolaus A. Adams |
| | 2. Prof. Dr. rer. nat. Marco Ellero |

Die Dissertation wurde am 23.05.2018 bei der Technischen Universität München eingereicht und durch die Fakultät für Maschinenwesen am 20.11.2018 angenommen.

# Acknowledgments

First of all, I would like to deeply thank Prof. Dr. Marco Ellero for giving me the opportunity to work on the topic I liked, providing great insights and supervision throughout my PhD, and giving me the freedom to choose certain aspects of our research.

I would also like to express a very special gratitude to Prof. Dr. Nikolaus A. Adams for providing a constant support during my work. Apart from insightful scientific discussions, finishing this work without his support as the head of AER would have been impossible.

I am very grateful to Dr. Andrew Comerford for co-advising my PhD. I owe many of my learnings during my PhD to our discussions. I additionally would like to extend my gratitude to my colleagues and friends at TUM, in particular, Dr. Xin Bian, Dr. Adolfo Vázquez-Quesada, Dr. Xiangyu Hu, Dr. Stefan Adami, Dr. Sergey Litvinov, and Mr. Yilei Shi.

My deepest gratitude and acknowledgment goes to my father and my mother. You are the single most important reason behind all of this. Your love and support have been a constant source of courage in my life. I would like to thank my two brothers as well. I have learned a lot from you. You guys are pretty cool.

Finally, I would like to specially thank Atefeh. You listened to my endless analytics and encouraged me when I failed. Your love has been my beacon of inspiration and hope.

# Abstract

This work focuses on studying the initiation and development of atherosclerosis from a mechanobiological perspective. The topic is of great interest due to the significant pressure it puts on health and monetary systems. It has been identified as the underlying cause of approximately 50% of all deaths in the western world. The disease is categorized as an inflammatory response of human immune system and is often associated with hypercholesterolemia, hypertension, obesity, and infection. Even though the onset is not fully understood, it is well established that atherosclerosis predominately occurs in regions of disturbed flow. Moreover, it is evident that excessive adhesion of leukocyte to endothelium is an important step at the beginning of a long chain of events leading to atherosclerosis.

With that realization, this thesis aims to provide a framework to study the transportation of leukocytes in large arteries and their near-wall dynamics. This framework has to be capable of overcoming a number of difficulties. Firstly, hemodynamics of large arteries exhibits complex three-dimensional features, e.g. secondary vortex formations, that are highly time-dependent in body's pulsatile flow environment. These features are unique in each human based on their specific anatomy. The developed framework should be able to model such complex pulsatile flow in patient-specific arterial geometry. Secondly, accurate modeling of leukocyte transportation in bulk and near-wall region of large arteries is quite challenging as reaching a meaningful trade off between accuracy and computational cost is by no means easy. Time scales that govern motion of leukocytes in bulk and near walls are so different that it is impossible to represent both domains with one model. This framework should provide domain-specific modeling to accommodate accurate capturing of key features such as near-wall concentration of leukocytes and their interaction with endothelium. Finally, establishing a link between flow parameters and surface biology is difficult. While numerous experiments have pointed out certain dependencies, variety of flow features and their influence on the complex cell adhesion process is by far not fully understood. This framework should provide a flexible model to, given sufficient experimental data, reproduce and model adhesion kinetics.

To address these issues, a multiscale model based on the Lagrangian particle

model, smoothed particle hydrodynamics, is developed. SPH is very capable of handling complex flow structures. arbitrary geometries, and time-dependent flow boundaries. Moreover, it is straightforward to extend it for e.g. a non-Newtonian model for blood. The framework utilizes a hybrid definition of the domain where SPH particles are used to model both the flow and concentration of leukocytes in bulk. However, to address the issue of unfeasible computational costs, the near-endothelium transportation of leukocytes is modeled by a specific Lagrangian particle tracking model based on Basset-Boussinesq-Oseen equation. This representation is coupled with bulk concentrations at an interface sufficiently distanced from the endothelium. As a result, while regions in vicinity of walls enjoy great resolution of discrete cells, the overall cost of simulations is kept low. Lastly, a stochastic binding model is used to incorporate leukocyte-endothelium adhesion dynamics. This model couples flow variables with small-scale bond formation properties.

Initially, the multiscale model was tested without the stochastic model to validate the approach and measure the gain it brings in computational effort. Results showed very good agreement with those of a validation application at a much lower particle count. In particular, for a two-dimensional setup of a backward-facing step, it was shown that the multiscale model consistently provided a computational gain factor of 42. In the next step, the framework was tested against experimental cell adhesion data in a three-dimensional axisymmetric sudden-expansion geometry. The stochastic cell adhesion parameters were tuned to reproduce experimental results in one setup, and the framework was tested to produce results of other setups. In both stationary and pulsatile flow, wall adhesion profiles matched with good accuracy with the experiment. Overall, the framework showed great capability and potential to model complex flow and adapt to specific cell-receptor kinetics via adhesion model parameters.

# Contents

# 1 Introduction

Study of cellular events in living organisms, and underlying molecular processes of the living tissue, is an active area of research in several disciplines. Together, these processes form the chain of events leading to more sophisticated biological responses. In case of living organism's defense mechanisms, these responses are categorized as immune responses that have one goal, to protect the organism against diseases. Nevertheless, a number of such responses translate into diseases themselves. Atherosclerosis, the underlying cause of about 50% of deaths in the western world (Lusis, 2000), is a well-known example.

## 1.1 Motivation: progression and development of atherosclerosis

Atherosclerosis is an inflammatory response of body's immune system (Ross, 1993, Packard and Libby, 2008, Moore et al., 2013). It is characterized by progressive narrowing and hardening of medium in large arteries, eventually leading to ischaemia of the heart, brain, or extremities, resulting in infarction (Ross, 1999). Despite extensive investigations, the precise mechanisms involved in atherosclerosis, particularly in its early stages, are highly disputed. However, it has become evident that atherosclerosis is an inflammatory disease involving a complex manifestation of cellular processes that occur over years and decades (Libby et al., 2002, Ross, 1999).

It is believed that atherosclerosis is initiated by a number of known risk factors, such as high blood cholesterol, hypertension, obesity and more recently infection. Sites of atherosclerosis are very focal in nature occurring predominately in regions of disturbed flow, where nitric oxide production is reduced (Libby et al., 2002). These regions of the endothelial surface are able to over express vascular adhesion molecules, such as VCAM-1, that bind leukocytes and mononuclear cells to the surface. This adhesion to the surface is thought to be one of the initiating events in the formation of atherosclerosis (Ross, 1993).

The expression is thought to be caused by the presence of modified low density lipoproteins (LDL) in the arterial intima Steinberg (1997). Following attachment

to the endothelium, monocytes migrate into the sub-endothelial space via inter-endothelial spaces where they differentiate into macrophages. This is a normal part of our body's inflammatory response to fight infections. Within the intima, the macrophages release monocyte-chemoattractive protein-1 (MCP-1) Crowther (2005), Libby et al. (2002), which recruits further leukocytes into the sub-endothelial space. Furthermore, the activated macrophages also secrete cytokines that promote migration and proliferation of smooth muscle cells (SMC) from the media into the intima. Within the intima, LDLs undergo oxidation due to prolonged exposure to reactive oxygen species. Oxygenated LDL (oxLDL) is very atherogenic, promoting further expression of adhesion molecules, and is very chemotactic for macrophages (Crowther, 2005). Macrophages express scavenger receptors along their outer membrane and these recognize oxLDL. This uptake of the oxLDL by macrophages results in reduced mobilization. These lipid-laden macrophages are known as foam cells. The accumulation of foam cells and leukocytes within the intima leads to the formation of fatty streaks, which appear as yellow discolorations on the luminal surface Hegele (1996). The proliferating SMC, from macrophage activation, secrete extracellular matrix (ECM) proteins leading to the formation of a fibrous cap. Fibrous plaque is characterized by relatively high mechanical strength and is actually a defense mechanism that prevents further thickening and protruding of the plaque via remodeling of the fatty tissue. After prolonged periods the foam cells may die leaving a necrotic core.

It is well established that atherosclerosis is not evenly distributed throughout the human vasculature, but tends to be site specific, occurring preferentially on the lateral wall of bifurcations and inner and outer walls of arterial bends Asakura and Karino (1990), Fox et al. (1982), Gimbrone et al. (2000), Zarins et al. (1983). This was identified from experimental studies using arteries excised from humans during autopsy and the similarity between all of these studies was the type of hemodynamic environment. For example, in the study by Zarins et al. (1983), histological sections were taken of the excised arteries and the blood flow was modeled using laser-Doppler anemometry in a scale model. Flow characteristics were then statically correlated to intimal thickness. A major finding was that intimal thickening is associated with low wall shear stresses (WSS), flow separation and non-axially aligned velocity profiles, whilst areas subjected to moderately high WSS and where the flow is axially aligned were not affected. The natural progression of this study was to implement an unsteady (oscillatory) flow field due to cardiac flow waveform. This was performed by Ku et al. (1985) who found a positive correlation between oscillatory WSS and intimal wall thickening in a same scale model of the carotid bifurcation. Further studies agreed with the above findings, using arteries excised from other regions of

the body, firmly establishing a relationship between disturbed hemodynamics and atherosclerosis. The above suggests that arterial geometry, hence the hemodynamic environment, is a major factor in the localization of atherosclerosis and development of atherosclerosis. Despite establishment of this correlation, it has been reported that hemodynamic environment alone is far from enough in predicting early stages of the disease (Steinman et al., 2003).

Consequently, this work aims to study early stags of atherosclerosis with respect to small particle binding. To that end, a simulation framework is sought to model transport of leukocytes in large arteries, their near-wall dynamics, and particularly their binding dynamics on the arterial wall. Eventually, a clear understanding of the interplay between hemodynamics and leukocyte adhesion, and its role in onset of atherosclerosis is expected.

## 1.2 Challenges in modeling of arterial flow

Atherosclerosis is clinically silent before reaching its intermediate progression stages, often taking years to decades. On top of that, the disease could reach advanced stages, associated with formation of atherosclerotic plaque and narrowing of lumen, without being detected and treated accordingly. Such slow progression makes it difficult to fully understand influential factors in onset of the disease. Nevertheless, prolific adhesion of leukocytes, due to a dysfunctional endothelium, has been identified as a key event in initiation of atherosclerosis (Ross, 1993). Therefore, near-wall dynamics of leukocytes is the main subject of interest in this work.

This conclusion is strongly supported in literature. It has been widely established that atherosclerosis is not evenly distributed throughout the vasculature, rather it is localized to very specific sites suggesting a role for hemodynamics in its initiation (Caro et al., 1971, Nerem and Cornhill, 1980, Glagov et al., 1988, Asakura and Karino, 1990). Additionally, it has been noted that WBCs, specifically monocytes, bind preferentially under flow conditions characteristic of these above-mentioned sites (Pritchard et al., 1995, Skilbeck et al., 2001, Chiu et al., 2003, Hinds et al., 2001, McKinney et al., 2006, Rouleau et al., 2010). This binding is coupled with an increased expression of adhesion molecules, such as ICAM-1 and E-selectin, as has been observed in a number of in-vitro experiments (Hinds et al., 2001, Chiu et al., 2003, McKinney et al., 2006, Rouleau et al., 2010). Furthermore, the studies of (Pritchard et al., 1995, Hinds et al., 2001) and (Chiu et al., 2003) all noted differences in their experimental results when cells were biologically inactive, thus concluding that it is important to consider both the hemodynamics and the biological activity

of the wall. Elucidating this tentative link between disturbed hemodynamics and the initiation of atherosclerosis remains and on-going challenge.

To address the problem, the first question that comes to mind is the manner by which leukocytes are transported in blood. The least would to be to consider typical characteristic of human hemodynamics in large arteries. It has been shown by several studies (Ku et al., 1985, Ku, 1997, Zarins et al., 1983, Botnar et al., 2000, Thomas et al., 2005, Urquiza et al., 2006, Sazonov et al., 2011, Holdsworth et al., 1999) that the flow of blood in such arteries exhibit complex three-dimensional features. Separated flow, secondary vortex patterns, recirculating regions, etc. are a few of such features. Flow pulsatility of human hemodynamics must be considered too as it can completely alter flow regime within one pulse. Moreover, adaptivity of arterial wall to external factors such as temperature, activity, stress, etc. adds a new dimension to the complexity of the problem. In short, movement of leukocytes requires understanding the complex flow of blood (Chiu and Chien, 2011).

Considering the blood as a suspension of cells in plasma, movement and concentration of leukocytes could be heavily influenced by how they interact with other cells. For example, red blood cells have been shown to change the distribution of platelets and leukocyte (Eckstein and Belgacem, 1991, Karino and Goldsmith, 1977, Goldsmith and Spain, 1984) and force them toward the wall (Melder et al., 1991, Munn et al., 1996). Once close enough to the endothelium, WBC-EC interactions, manifesting in complex adhesion forces, gain significance. Quite expectedly, different cell types show specific adhesion behavior. Therefore, it appears that, as complex large artery hemodynamics is, it is not sufficient in studying the near-wall dynamics of leukocyte (Steinman et al., 2003). To address this issue, this work aims to provide a mechanobiological modeling framework that combines flow conditions with cell adhesion kinetics. In particular, the following challenges have to be addressed.

The first challenge is accurate simulation of the flow of blood in the entire arterial domain. While accurate modeling of fairly complex flow patterns is feasible with a reasonable effort, it is equally important to resolve near-wall flow features with very high accuracy (Hanzlik et al., 2008). Even though flow in extreme vicinities of the endothelium might not be as complex as in bulk, its accuracy substantially affects the accuracy of near-wall cell interactions such as rolling and adhesion. Due to extremely long initiation time scales of atherosclerosis, achieving acceptable accuracy in the entire domain with reasonable computational effort is especially challenging in this work.

Secondly, modeling leukocyte transport is either unfeasibly expensive or inaccurate. One approach is to use an Eulerian representation of leukocytes, e.g. in form of a concentration field. This approach was used in Lyczkowski et al. (2009) to model non-

uniform distribution of monocytes in flow. While their approach was not expensive, results were not particularly accurate. Alternatively, a Lagrangian approach could be employed to represent leukocytes as discrete particles in flow. The advantage of this method is its flexibility in predicting highly non-uniform distribution patterns, as it follows the nature of leukocyte in blood very closely. However, considering the number of particles needed to achieve accurate deposition results in large arteries, this approach is not an option. It was observed that, based on typical leukocyte concentration in blood and the characteristic size of large arteries, reaching a fully converged deposition profile requires inclusion of hundreds of millions of particles in a simulation (Gholami et al., 2014).

The last challenge is establishing a proper link between flow conditions and near-wall behavior of leukocytes. WBC adhesion represents a balance between the strength of adhesive bonds on the one hand and hemodynamic forces on the other. Therefore, near wall hemodynamic forces have a dual effect on the adhesion of WBCs (and other small blood-borne molecules). First, transport to and away from the surface of these small molecules is driven by local hemodynamic forces and residence time (Longest et al., 2003). Second, they adhere to the endothelium depending on the balance between local hemodynamic forces and the kinetics of association and dissociation(Rinker et al., 2001); this can be considered a stochastic process (Zhu, 2000). The latter is further complicated in the vasculature due to the ability of the endothelium to adapt its phenotype, signaling and gene expression according to the prevailing hemodynamic environment (Gimbrone Jr et al., 1997, Nerem et al., 1998, Chiu et al., 2009), thus hemodynamics and adhesive bond strength is interrelated. Understanding the intricate connection between hemodynamics and adhesion of WBC is an unresolved issue.

The complex interplay of unsteady flow, three-dimensional flow features, adhesion kinetics, etc. obstructs development of a clear cause and effect relation. For examples, it is shown that unsteady flow affects biological environment (Hsiai et al., 2003), however, it is not known if and how these conclusions can be extended to all cell types (Steinman et al., 2003, Lyczkowski et al., 2009). Previously a number of models have attempted to elucidate the separate role of disturbed haemodynamics and molecular adhesion to the endothelium. A variety of approaches have been proposed to achieve this goal (see for example (Rinker et al., 2001), (Comerford and David, 2008), and (Hossain et al., 2014)); although these models have different areas of interest the over-arching goal is to elucidate the role of haemodynamics and cellular/molecular adhesion and the association with the initiation of atherosclerosis. Furthermore, lack of experimental data, obtained in similar flow conditions, prohibits sufficient validation of existing cell adhesion models when used in conjugation with

a macroscopic flow model.

To overcome these challenges, a multiscale modeling framework is developed based on a Lagrangian particle solver. It allows easy manipulation of arterial geometry or adopting complex models for blood, as a non-Newtonian fluid. Dynamics of leukocytes is modeled through introduction of tracer particles to the computational field. As mentioned, typical spatio-temporal scales governing the problem are so distinct that it is computationally not feasible to simulate cell-endothelium interactions with conventional methods. Therefore, a dual continuous-discrete definition of leukocyte field is introduced to couple bulk-wall quantities is an extremely efficient manner. The discrete representation of the field is restricted to vicinities of wall to save computational work yet enable accurate and flexible near-wall modeling of leukocytes. WBC-EC interactions are simulated using a stochastic adhesion model that provide a link between hydrodynamics forces and adhesion kinetics. Finally, inflow/outflow boundary conditions are implemented for realistic replication of pulsatile blood flow.

## 1.3 Numerical modeling of atherosclerosis progression

Previously in literature a number of studies have considered the transport of leukocytes and other small blood borne particles in arterial geometries related to atherosclerosis Kunov et al. (1996), Tambasco et al. (2002), Buchanan et al. (2003) as well as intimal hyperplasia of a distal anastomosis Longest and Kleinstreuer (2003), Longest et al. (2004). Kunov *et al.* Kunov et al. (1996) studied particle transport in a 2D stenosis. Their method assumed Lagrangian volumes to have a uniform concentration of particles. This approach was primarily motivated by the fact that the platelet concentration in blood is unrealistically high from computational perspective. In this study, they also introduced the concept of "volumetric residence time". Tambasco *et al.* Tambasco et al. (2002) modelled small particles, such as platelets, using the same method as Kunov et al. (1996), in a stenosed carotid bifurcation. They reported that impractically fine meshes are required to capture complex geometric features in the near wall region using particle methods. Furthermore, particle trajectories were very sensitive to the resolution of the underlying velocity field, hence care must be taken when interpreting the outcomes as quantitative. Buchanan *et al.* Buchanan et al. (2003) performed transient particle dynamics in a model of the rabbit abdominal aorta. In this

method the particle transport equations for a dilute suspension of spherical particles were solved based on a precomputed velocity field. They determined that monocyte adhesion (calculated as the number of particles adjacent to a specific area of the wall) correlated with lesion development measured in cholesterol-fed rabbits and also with a number of traditional hemodynamics parameters. In Longest and Kleinstreuer (2003), Longest et al. (2004) the transport of micro-particles (in particular platelets) in an idealised and realistic end-end anastomosis were investigated. Although these are related to a surgical procedure the development of the diseased area will be similar processes. They determined high residence time in areas associated with intimal hyperplasia.

The aforementioned studies have highlighted the importance of Lagrangian simulations in studying particle deposition patterns in the initiation and development of atherosclerosis. However it has been also highlighted that the methods used are computationally expensive when considering transient flows in complex geometries. Smoothed Particle Hydrodynamics (SPH) is a popular Lagrangian method that has proven to be capable of handling such problems very suitably. It was originally developed for modeling compressible flow problems in astrophysics Gingold and Monaghan (1977), Lucy (1977), but later its applications were extended to a variety of engineering problems amongst which are: non-Newtonian fluids, free-surface flows, multiphase problems, micro/biofluidics, fluid-solid interaction, modeling solid material, etc. Recent developments and applications of SPH are reviewed in Monaghan (2012), Liu and Liu (2010). More specifically, SPH has been used by several groups to simulate blood flow and related applications. In a recent work, Shahriari *et al.* Shahriari et al. (2012) used SPH to model hemodynamics of heart's left ventricle with pulsatile inlet velocity. Similarly, Sinnott *et al.* Sinnott et al. (2006) investigated blood flow in realistic carotid artery bifurcation. Capillary flow and deformation of red blood cells in micro vessels were studied in Hosseini and Feng (2009), Tanaka and Takano (2004). Effect of blood properties, specifically hematocrit, on hemodynamics of microcirculation was studied in Tsubota et al. (2006). Authors of Müller et al. (2004a,b) used SPH to simulate interaction of fluid with solids and free surfaces with applications in virtual surgery simulators. Furthermore, Hieber *et al.* Hieber et al. (2004) extended the application of SPH in biomedical problems to study mechanical behavior of human organs.

In the present study we develop an advanced multiscale SPH approach that allows particle methods for hemodynamic simulations to be achieved in a tractable manner. As an example, Longest *et al.* Longest et al. (2004) uses a maximum of 500000 tracers in full domain in a realistic femoral anastomosis geometry to reach convergence. Considering the normal concentration of leukocytes in blood, ca.

$10^4/mm^3$, and typical size of large vessels, a fully converged near-wall profile requires computation of trajectories for hundreds of millions of tracers which is about 1000 times more. In contrast, we reduce the number of tracers through specific tracking of leukocytes only in close vicinity of walls. Even though this problem is extremely demanding, our approach brings substantial reduction of computation work.

## 1.4 Outline of the thesis

In chapter 2, the flow modeling component of the framework, using smoothed particle hydrodynamics method, is discussed. In particular, it is explained how this model brings flexibility to model the complex hemodynamics in large arteries while keeping the computational requirements manageable. In chapter 3, a full multiscale flow model is explained. In particular, the Lagrangian particle tracking is discussed to understand terms of the original formulation can be omitted to save computational work in the vicinity of walls. In chapter 4, kinetic modeling of short-range interactions of leukocytes with endothelium is outlined. The stochastic adhesion model used in this work is discussed in relation with other modeling approaches. Finally, in chapter 5, general purpose inflow and outflow boundary conditions for SPH are discussed. These conditions are required to make realistic pulsatile environment in patient-specific arterial geometries possible. Finally, all findings and conclusions of this work are briefly reviewed and discussed in chapter 6.

# 2 Smoothed particle hydrodynamics

As discussed in section 1.3, particle methods represent a valuable tool to simulate such complex problems as those represented by particulate flow of blood through a cardiovascular network. This is because of the unique properties of particle methods which allow for a Lagrangian description of material transport. However, a direct representation of blood in terms of real-sized blood cells suspended in a Newtonian plasma is feasible only on very small spatial/temporal scales. The large scale separation existing between biological components (order of $\mu$m) and typical vessel size in the macrovascular network (order of cm) prevents the use of mesoscopic particle methods (i.e. DPD (Hoogerbrugge and Koelman, 1992)).

A better strategy when dealing with flow in a macrovascular network is to keep the continuum viewpoint and couple it with a discrete representation of the leukocytes as test particles rather than real cells. This can be done by adopting a macroscopic particle method based on the Lagrangian solution of a suitable set of partial differential equations and by taking into account the distribution of microscopic cells by considering point-size test tracers moving in a *macroscopically evaluated* flow field. As a result, in this work an approach based on Smoothed Particle Hydrodynamics (SPH) ((Liu and Liu, 2003, 2010, Monaghan, 1992)) is used. SPH was originally developed for modeling compressible flows in astrophysics (Lucy, 1977, Gingold and Monaghan, 1977) and later applied to many fluid dynamics applications. It has also been used to model hemodynamics (Sinnott et al., 2006, Shahriari, 2011, Hosseini and Feng, 2009, Tanaka and Takano, 2004, Tsubota et al., 2006, Müller et al., 2004a, Hieber et al., 2004). SPH's capability to handle extremely complex flow conditions suites this nature of work very well.

## 2.1 General formulation

SPH uses a weighted interpolation to determine the values of a function $f$, and its derivative, at any point $\mathbf{r}$ in space. The weighting function is called the *smoothing*

*kernel* and is denoted by $W$. Hence, the integral form of the interpolant could be written as

$$\langle f(\mathbf{r})\rangle = \int f(\mathbf{r}')\, W(\mathbf{r}-\mathbf{r}', h)\, d\mathbf{r}', \tag{2.1}$$

where $\langle f(\mathbf{r})\rangle$ is an approximation to $f(\mathbf{r})$, and $h$ is the *smoothing length* of the kernel. There are infinite number of possible kernel functions. However, in practice, any kernel function have to satisfy two conditions. Firstly, as the *smoothing length* goes to zero, the kernel function must tend to the delta function, i.e.

$$\lim_{h\to 0} W(\mathbf{r}-\mathbf{r}', h) = \delta(\mathbf{r}-\mathbf{r}')\,. \tag{2.2}$$

Following Eq. 2.1, this condition gives:

$$\lim_{h\to 0}\langle f(\mathbf{r})\rangle = f(\mathbf{r})\,. \tag{2.3}$$

Secondly, the kernel should be normalized to give exact result for a constant function:

$$\int W(\mathbf{r}-\mathbf{r}', h)\, d\mathbf{r}' = 1. \tag{2.4}$$

Additionally, for the sake of computational efficiency, kernel functions are typically chosen to vanish after a finite distance. This property is called compact support.

Several types of kernel function can be found in the literature (Monaghan, 2012, Liu and Liu, 2003, 2010, Dehnen and Aly, 2012, Springel, 2010, Fulk and Quinn, 1996). Piece-wise continuous splines are the most common (Schönberg, 1946, Monaghan and Lattanzio, 1985). This type of kernel function has compact support and could be defined to be high-order derivative continuous (Monaghan, 2005).

### 2.1.1 Discrete formulation

The continuous integral interpolant, Eq. 2.1, could be written in the discrete form as the sum of function values over a discrete set of points, SPH particles. Assuming the summation over a finite number of particles, $N$, we have:

$$\langle f(\mathbf{r})\rangle \simeq \sum_j f(\mathbf{r}_j)\, W(\mathbf{r}-\mathbf{r}_j, h)\, \mathcal{V}_j. \tag{2.5}$$

$\mathcal{V}_j$, the discrete equivalent of $d\mathbf{r}'$, is the finite volume associated with particle $j$, hence:

$$\mathcal{V}_j = m_j/\rho_j, \tag{2.6}$$

where $m_j$ and $\rho_j$ are mass and density of particle $j$, respectively. As long as the kernel is continuous, Eq. 2.5 allows a continuous interpolation of function $f$ using its value at a finite number of disordered particles. In the same way, one could evaluate the derivatives of $f$ using Eq. 2.5:

$$\nabla\langle f(\mathbf{r})\rangle \simeq \sum_j f(\mathbf{r}_j)\,\nabla W(\mathbf{r}-\mathbf{r}_j,h)\,\mathcal{V}_j, \tag{2.7}$$

in which the kernel function is assumed to be differentiable. The significance of Eq. 2.7 is in that it uses only function values at discrete points, $f(\mathbf{r}_j)$ to calculate the derivative. However, this method is, by far, not the most suitable way to calculate derivatives. One could see the even though it uses an exact derivative of an analytical function, it does not vanish if $f$ is constant. In order to improve the accuracy, there are several methods to evaluate function derivatives in SPH (Monaghan, 2005).

Finally, it must be noted that the discrete formulation, Eq. 2.5, provides an approximation in comparison with the integral interpolant. Obviously, with increasing the number of particles within the kernel range, the associated error would decrease.

## 2.2 Lagrangian hydrodynamic modeling

Using the definitions provided in the previous section, we now move to determine the SPH formulation of the governing equations of our system. We first assume that full Navier-Stokes equations to fit our specific application. To describe the haemodynamics of large arteries, we assume that the blood in the bulk to be a continuous phase. Therefore, our system is governed by the isothermal Navier-Stokes equations which, written in a Lagrangian framework, have the following form (Batchelor, 1967)

$$\frac{d\rho}{dt} = -\rho\nabla\cdot\mathbf{v}, \tag{2.8}$$

$$\frac{d\mathbf{v}}{dt} = -\frac{\nabla p}{\rho} + \mathbf{F} + \mathbf{g}, \tag{2.9}$$

where $\rho$, $\mathbf{v}$, $p$, $\mathbf{g}$, and $\mathbf{F}$ are, material density, velocity, pressure, body force, and viscous force, respectively. Note that the convective term, $\mathbf{v}\cdot\nabla\mathbf{v}$ is absent in Eq. 2.9 as it only appears in an Eulerian representation.

Considering the range of velocities in major arteries of human body (Botnar et al., 2000, Gallo et al., 2012, Holdsworth et al., 1999, Ku, 1997, Ku et al., 1985),

incompressibility is an absolutely suitable assumption. The equation of state for a *nearly incompressible* fluid relating pressure to density, as given by Batchelor (1967) and Monaghan (1994), can be written as

$$p = p_0 \left[ \left( \frac{\rho}{\rho_0} \right)^{\gamma} - 1 \right], \tag{2.10}$$

where $p_0$, $\gamma$ and $\rho_0$ are parameters chosen based on a scale analysis (Monaghan, 1994, Morris et al., 1997) such that density variations are smaller than a prescribed value. Specifically, density variation $|\delta\rho|/\rho$ is quadratically proportional to the Mach number,

$$\frac{|\delta\rho|}{\rho} \sim \frac{v^2}{{c_s}^2}, \tag{2.11}$$

where $c_s$ is the speed of sound. According to Eq. 2.11, choosing a large-enough speed of sound ensures validity of the *nearly incompressible* assumption.

Furthermore, viscous forces for a Newtonian flow $\mathbf{F}$ reduce to

$$\mathbf{F} = \nu \nabla^2 \mathbf{v}, \tag{2.12}$$

where $\nu = \eta/\rho$ is the fluid kinematic viscosity and $\eta$ is the dynamic viscosity. Application of more complex equations describing the dynamics of non-Newtonian or viscoelastic fluids would be a valid consideration. Such behavior has already been studied in the framework of SPH (Ellero and Tanner, 2005, Vázquez-Quesada and Ellero, 2012). However, as haemodynamics of large macro-vessels can be quite accurately modeled by the standard Navier-Stokes equations with constant viscosity (Ethier and Simmons, 2007), we will use the Newtonian viscosity model, as in Eq. 2.12, in this work.

Following Eqs. 2.5 and 2.7, Eqs. 2.8-2.9 can be discretized using SPH, which allow evaluation of fluid quantities at any point in space (Monaghan, 1992). Eq. 2.8, namely conservation of mass, is automatically satisfied if particle density is evaluated as (see Espanol and Revenga (2003))

$$d_i = \sum_j W_{ij}, \tag{2.13}$$

where $d_i = 1/\mathcal{V}_j$ is the number density associated to SPH fluid particle $i$ and $W_{ij} = W(|\mathbf{r}_i - \mathbf{r}_j|, h)$.

Application of the SPH approximation to Eq. 2.9 produces the following equations for the particle positions and momenta (Espanol and Revenga, 2003, Vázquez-Quesada et al., 2009)

$$\begin{aligned}\dot{\mathbf{r}}_i &= \mathbf{v}_i,\\ m\dot{\mathbf{v}}_i &= -\sum_j \left(\frac{p_i}{d_i^2}+\frac{p_j}{d_j^2}\right) W'_{ij}\mathbf{e}_{ij} + 2\eta\sum_j \frac{W'_{ij}}{d_i d_j}\frac{\mathbf{v}_{ij}}{r_{ij}} + \mathbf{g}_i,\end{aligned} \tag{2.14}$$

where

$$\begin{aligned} r_{ij} &= |\mathbf{r}_i - \mathbf{r}_j|,\\ \mathbf{e}_{ij} &= (\mathbf{r}_i - \mathbf{r}_j)/r_{ij},\\ \mathbf{v}_{ij} &= \mathbf{v}_i - \mathbf{v}_j,\\ W'_{ij} &= \left.\frac{\partial W(r)}{\partial r}\right|_{r=r_{ij}}. \end{aligned}$$

Due to anti-symmetry under particle index exchange of the binary force contribution within the sums, Eq. 2.14 conserves automatically the total momentum (Ellero and Adams, 2011). Note that it is straighforward to write a generalized form of Eq. 2.14 to use a non-Newtonian viscosity model, a relevant assumption for cardiovascular flows (Ellero and Tanner, 2005, Ellero et al., 2002).

In order to implement time integration of Eq. 2.14, a time step is chosen based on three criteria:

$$\begin{aligned} dt_{\text{cfl}} &= 0.25h/c_s,\\ dt_{\text{visc.}} &= 0.125h^2/\nu,\\ dt_{\text{force}} &= \sqrt{h/f^{\max}}, \end{aligned}$$

where $f^{\max}$ is the maximal force per unit of mass acting on an SPH particle. The final time step would be the minimum of these time steps:

$$dt_{\text{SPH}} = \min\left(dt_{\text{cfl}}, dt_{\text{visc.}}, dt_{\text{force}}\right). \tag{2.15}$$

This equation points out that speed of sound should be chosen carefully as an arbitrarily large $c_s$ results in an excessively small time step. As a last remark, to update the positions and velocities of the SPH fluid particles, a modified explicit velocity Verlet algorithm is used (Bian et al., 2012, Groot and Warren, 1997). This scheme uses a velocity prediction step before integration positions.

## 2.3 Bulk diffusion

While small tracers are in the bulk, away from walls, their motion is modeled as a continuous phase. This approach has the advantage that by definition of a bulk concentration field $C(\mathbf{r}, t)$, tracers are *automatically* carried by our Lagrangian SPH particles. Hence, tracer concentration for SPH particle $i$ would be

$$C(\mathbf{r}_i, t) = N_i / \mathcal{V}_i, \tag{2.16}$$

with $N_i$ being the number of tracers associated to the fluid particle $i$ and $\mathcal{V}_i = 1/d_i$ the fluid particle volume. Note that $N_i$ could correspond to any distribution of tracers in the bulk. This makes it possible to impose a non-trivial distribution at the boundaries or as initial condition.

The SPH concentration field, defined in Eq. 2.16, satisfies exactly

$$\frac{\partial C}{\partial t} + (\mathbf{v} \cdot \nabla) C = 0. \tag{2.17}$$

In reality, we need to consider diffusion of tracer concentration due to the erratic motion of white blood cells induced by red blood cells (Goldsmith and Karino, 1977, Longest, 2002). Such behavior results in introduction of a diffusion coefficient, $D$, in Eq. 2.17:

$$\frac{\partial C}{\partial t} + (\mathbf{v} \cdot \nabla) C = D \nabla^2 C, \tag{2.18}$$

Incorporation of the diffusion term in Eq. 2.18 into the equations of motion for the SPH particles can be performed in two ways.

### 2.3.1 Smoothed dissipative particle dynamics

The SPH formulation presented in this chapter does not consider thermal fluctuations. This prevents SPH to be applicable in mesoscopic problems. On the other end of the spectrum, we have dissipative particle dynamics (DPD) (Hoogerbrugge and Koelman, 1992, Espanol and Warren, 1995, Groot and Warren, 1997) where thermal fluctuations are taken into account but does not provide a direct way to specify transport properties. Additionally, DPD lacks a well-defined physical scale and does not allow use of arbitrary equations of state.

Smoothed Dissipative Particle Dynamics method (SDPD), proposed by Espanol and Revenga (2003), combines SPH and DPD to overcome the shortcomings mentioned above (Vázquez-Quesada et al., 2009, Hu and Adams, 2006a). SDPD adds

random momentum fluctuations to the standard SPH equations in a thermodynamically consistent way. In this way, it adds a random force term to the momentum equation, Eq. 2.14, on top of pressure and viscous forces. As a result, the diffusive behavior is implicitly incorporated into the momentum equations through this stochastic. In the current context, this random term takes this form:

$$m d\tilde{\mathbf{v}}_i = \sum_j \left[ -8 \frac{k_B T \mu}{d_i d_j} \frac{W'_{ij}}{r_{ij}} \right]^{1/2} d\overline{\overline{\mathbf{W}}}_{ij} \cdot \mathbf{e}_{ij}, \tag{2.19}$$

where $k_B$ is the Boltzmann constant, $T$ temperature, and $d\overline{\overline{\mathbf{W}}}_{ij}$ is the traceless symmetric part of a matrix of independent increments of a Wiener process. The corresponding diffusion coefficient can be selected by matching the desired properties of the dispersed phase (Gholami et al., 2014). Using the analytical expression for the self-diffusion coefficient of SDPD (Litvinov et al., 2009), diffusion coefficient can be specified a priori as input parameter.

### 2.3.2 SPH discretization

In a different approach, one could discretize Eq. 2.18 and explicitly solve for tracer concentration as a SPH variable. This approach is motivated by the work done by Ellero et al. (2003). In that work dumbbells are created in each fluid particle to study polymer diffusivity. The number of dumbbells is treated as an additional variable that undergoes thermal fluctuations. A detailed derivation of the SPH discretization of the advection-diffusion equation could be found in Appendix E of Ellero et al. (2003). In case of the current study, the SPH discretization of the transport equation, Eq. 2.18, yields:

$$\dot{N}_i = 2D \sum_j \frac{W'_{ij}}{d_i d_j} \frac{1}{r_{ij}} \left( N_i d_i - N_j d_j \right), \tag{2.20}$$

where $N_i$ is the number of tracers carried by SPH particle $i$. Similar to the previous approach, the overall number of tracers is conserved throughout the simulation.

We have tried both of this methods in this work. The first approach, as demonstrated in Gholami et al. (2014), delivers good results and is straightforward to use. However, we later used the second approach as its suits the requirements of this study better (Gholami et al., 2015). Modeling of tracers' bulk diffusion using the second approach had the advantage that each SPH particle carries a meaningful tracer concentration at each time. In addition to the flexibility it brings in comparison to the first approach, this property could be desirable when the

wall undergoes structural changes, as a result of tracer accumulation, during the course of the simulation (Gholami et al., 2015). As studying the progression of an atherosclerotic plaque would require dealing with wall remodeling in later stages, the second approach, SPH discretization of advection-diffusion equation, is very fitting to current and future requirements of this work.

## 2.4 Kernel function

As mentioned earlier, piece-wise continuous splines are the most common family of kernels. However, there are several other kernel types. For example, a simple *Gaussian kernel* is stable and infinitely differentiable; however, it has no compact support. Such a kernel requires calculation of contributions of every particle in the simulation. This characteristic severely limits the use of this kernel in large applications with many particles. piece-wise continuous spline kernels provide a reasonable mix of smoothing properties and computational efficiency. Let's have a quick look at two common spline kernels: 2D normalized form of cubic spline,

$$W(\mathbf{r}, h) = \frac{10}{7\pi} \begin{cases} 1 - \frac{3}{2}(r/h)^2 + \frac{3}{4}(r/h)^3 & 0 \leq r/h < 1 \\ \frac{1}{4}(2 - r/h)^3 & 1 \leq r/h < 2 \\ 0 & r/h \geq 2, \end{cases}$$

and quintic spline,

$$W(\mathbf{r}, h) = \frac{7}{748\pi} \begin{cases} (3 - r/h)^5 - 6(2 - r/h)^5 + 15(1 - r/h)^5 & 0 \leq r/h < 1 \\ (3 - r/h)^5 - 6(2 - r/h)^5 & 1 \leq r/h < 2 \\ (3 - r/h)^5 & 2 \leq r/h < 3 \\ 0 & r/h \geq 3. \end{cases}$$

Fig. 2.1 shows a comparison of these two kernels. The quintic spline has four continuous derivatives, while the cubic spline has two. Smoother kernels provide better stability as stability properties of SPH depends strongly on the second derivative. For example, (Morris et al., 1997) showed that cubic spline kernel produces significant noise in pressure and velocity fields for low Reynolds number simulations. However, they showed that while quintic spline kernel remains stable, it is approximately twice as expensive as the cubic spline kernel.

In the current work, both cubic spline and quintic spline kernels were employed. Even though in many cases the difference between these two kernels was reduced to

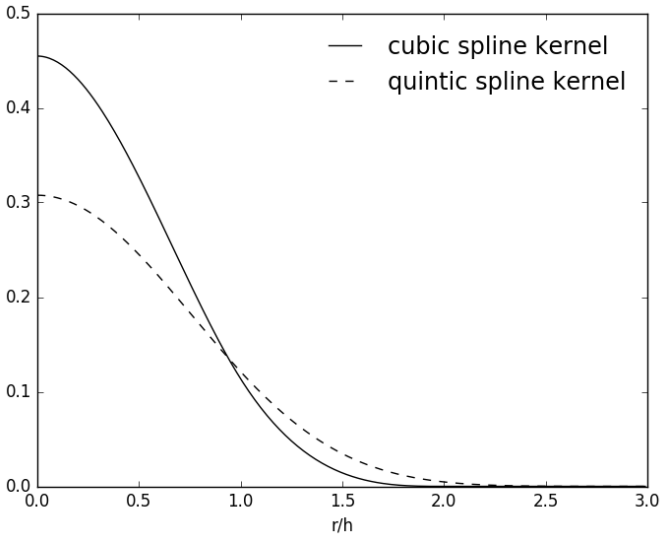


Figure 2.1: Comparison of cubic spline and quintic spline kernels - quintic spline is smoother, i.e. its first four derivatives are continuous, while cubic spline has two.

higher computational costs of the latter, quintic spline kernel still was chosen as the default kernel in many simulations. Due to its more stable nature, the quintic kernel seemed a more suiting choice for arterial flow where pressure waves in form of pulses drive the flow.

## 2.5 Numerical verification

Before moving on to the rest of the work, a number of well-established cases were tested with the implementation of the SPH to verify the validity of the code. In particular, flow in a lid-driven cavity, Couette flow, and Poiseuille flow were examined. Since capabilities of SPH in accurately simulating the flow for these case is already established, see (Morris et al., 1997, Ellero et al., 2002), this section focuses on a scenario that is relevant for the rest of the work.

For this purpose, a backward-facing step (BFS) geometry is used. This geometry is simple but the flow over BFS features fairly complex patterns such as sudden expansion and recirculation zone. Additionally, these flow features are highly relevant for the application targeted in this work. For example, a sudden expansion and subsequent recirculation zone are common in atherosclerosis-prone sites such as

aneurysms and carotid artery bifurcation. A 2D BFS geometry similar to that of (Issa, 2005) is tested. The computational domain, shown in Fig.2.2a has a length of 122.4 $mm$ and height of 10.1 $mm$. Two steps, one at inlet and one at outlet, are introduced. Each step has a length of 16.3 $mm$ and height of 4.9 $mm$. To validate the flow, velocity profiles at four sections along the domain are compared to Fluent simulations from (Issa, 2005). These four sections, P1 to P4, are positioned at 4.9 $mm$, 18.13 $mm$, 20.09 $mm$, and 49.98 $mm$ from the inlet. Flow Reynolds number, based on mean bulk velocity at inlet and twice the inlet height, is 100 which corresponds to a mean bulk velocity of 0.14 $m/s$.

As shown in Fig.2.2, velocity profiles in all four section show very good agreement with the reference solution. As mentioned earlier, the results of the SPH code is already verified using other well-known benchmark cases. However, in this work, it is particularly important that complex features such as recirculation zone are modeled accurately. It will be shown later than the problem of particle tracking is extremely sensitive to flow conditions. Presence of flow separation only makes the situation more critical. With this in mind, we move on to the next chapter where the challenge of modeling the discrete phase is discussed.

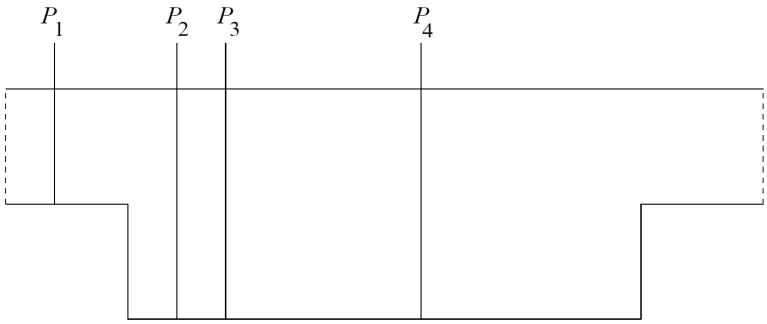


(a) Backward-facing step geometry

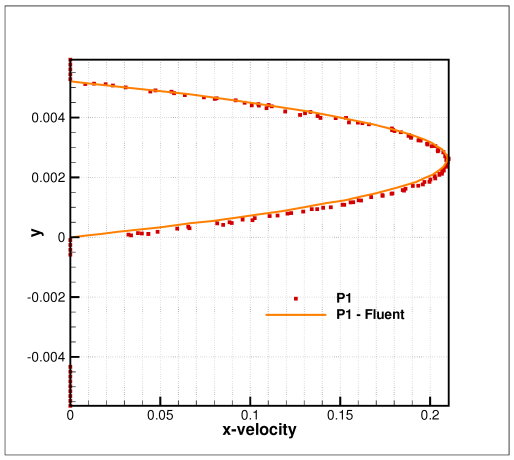


(b) at section P1

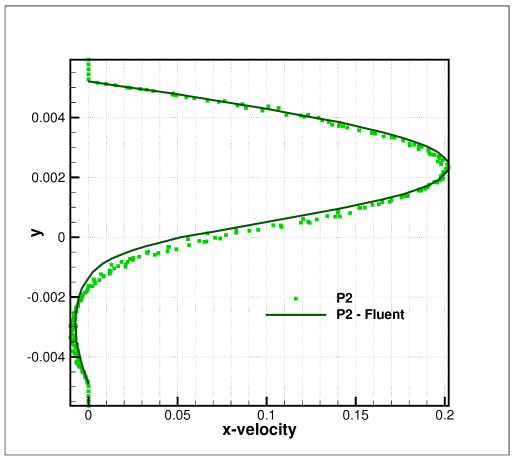


(c) at section P2

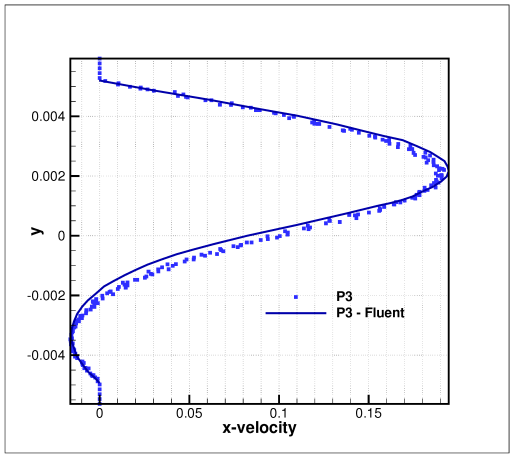


(d) at section P3

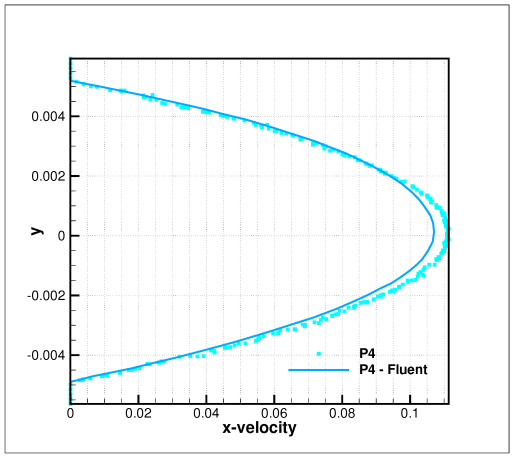


(e) at section P4

Figure 2.2: Comparison of the velocity profiles at different sections of the channel

# 3 Multiscale flow modeling

Among several numerical studies that have considered the transport of WBCs and other small blood borne particles in arterial geometries, a Lagrangian particle tracking (LPT) seems to be the standard approach (Kunov et al., 1996, Tambasco et al., 2002, Buchanan et al., 2003, Longest and Kleinstreuer, 2003, Longest et al., 2004). This is justified by the fact that the number of leukocytes in blood is normally much lower than that of red blood cells (less than 1% of whole blood compared to the 45% hematocrit) Alberts et al. (2002), so they have negligible influence on the dynamics of blood and can be reasonably described as passive tracers. Utilizing a standard LPT approach, trajectories of leukocytes are calculated by integrating equations of motion of the form:

$$\dot{\mathbf{x}}_k = \mathbf{u}_k \tag{3.1}$$

$$\dot{\mathbf{u}}_k = \mathbf{f}_k, \tag{3.2}$$

where $\mathbf{x}_k$, $\mathbf{u}_k$, and $\mathbf{f}_k$ are position, velocity, and force per unit mass of the tracer $k = 1, .., N_{\texttt{tracer}}$, respectively. The acting force ($\mathbf{f}_k$) is evaluated using the information from the fluid flow. From the knowledge of the tracers distribution, an average concentration field both in the bulk and in the near-wall region can be computed Longest et al. (2004). This standard approach is straightforward to implement in connection with a given discretization of the flow field, but it is computationally very expensive for the specific application targeted in this work. Indeed, when only information on the near-wall WBC concentration is required (which is the case relevant to atherosclerosis), it is inefficient to track WBC motion over the entire fluid domain. Moreover, a very large number of tracers must be considered in order to achieve a statistically relevant ensemble in the interesting near-wall region (typically a layer of few leukocyte diameters thickness) which is much smaller than the entire bulk control volume in macroscopic vessels. This drawback of standard LPT approaches leads to a prohibitively large number of tracers to be simulated with consequent computational bottleneck (Gholami et al., 2013, 2014).

In order to solve this problem, our proposed method is based on a splitting of the domain into two regions: the bulk flow and the near-wall region. Modeling solid

tracers in the bulk is based on a continuum approach and is done via advection/diffusion of a concentration field $C(\mathbf{r}, t)$ by using a Lagrangian fluid solver, namely Smoothed Particle Hydrodynamics (SPH) (Lucy, 1977, Gingold and Monaghan, 1977). Transport of such small tracers in flow conditions relevant in this work are characterized by very small Stokes number ($St_k = \tau_p U/d \ll 1$) and usually a very large Péclet number ($Pe = Ud/D \gg 1$). In this limit, diffusion is negligible and passive tracers follow similar pathlines as fluid particles in the bulk. As a consequence, their dynamics can be modeled on a continuum basis by using a bulk concentration field $C(\mathbf{r}, t)$. Thanks to the Lagrangian property of SPH, advection is implicitly modeled in such a way that the number of passive tracers within every SPH fluid particle can be considered to be constant during the flow. This allows to define a tracer concentration carried by each SPH particle similar to Eq. 2.16. Two approaches in continuous modeling of the tracers was discussed in Sec. 2.3. Those approaches cover the bulk dynamics of passive tracers.

On the other hand, in the near-wall region, discrete tracers are created allowing the application of a standard LPT only in a small portion of the domain. Separate treatment of tracers in each near-wall sub-domain is necessary in order to incorporate lubrication effects as well adhesive forces for which no-closed continuum equation for $C(\mathbf{r}, t)$ is available. Finally, continuum/bulk and discrete/near-wall solutions are coupled at the interface between the two domains enforcing conservation of mass. Since the particle tracking is limited to WBCs only in the near-wall region, our approach brings considerable speed-up to the simulation of WBC circulation. In this chapter, near-wall dynamics of tracers and the coupling scheme that brings the proposed multiscale method together are discussed.

## 3.1 Discrete phase: Lagrangian particle tracking

Transport of WBCs in blood is governed by significantly smaller time scales ($\tau_p = \rho_p d_p^2/18\mu$) compared to that of the bulk blood flow ($\tau_{\texttt{flow}} = d/U$), with $\rho_p$ and $d_p$ being tracers density and diameter, $d$ the diameter of the artery, and $U$ the flow velocity. As a result, our method adapts a discrete definition of tracers only in the near-wall region where, due to the complex tracer-wall interactions, a continuum description based on evolution equations for a concentration field is infeasible. Furthermore, it is straightforward to extend this approach to situations where realistic wall interaction models are considered, such as wall adhesive forces to represent the binding of leukocytes to the endothelial layer.

### 3.1.1 Basset-Boussinesq-Oseen equation

The role of flow parameters in onset and progression of many vascular diseases is extensively studies. Additionally, the transport of blood cells, as the normal mechanism to e.g. move oxygen and nutrition, trigger inflammatory response, and activate platelets, has received considerable attention. Among the studies that approach these problem from computationally, application of Lagrangian particle tracking (LPT) is modeling the transport of blood-borne particles is very common (Gholami et al., 2012).

For example, Kunov et al. (1996) used LPT to study platelet residence time in arterial geometries. Their work was motivated by the fact that activation of platelets could be triggered by hydrodynamics of flow, and in turn could lead to secondary side effects. Tambasco et al. (2002) investigated the accuracy of quantitative parameters, e.g. deposition patterns, residence time, that depend on particle trajectories. Their study addressed the issue that, for a calculating a *sufficiently accurate* path-dependent parameter, the resolution of the computed fluid field should be known in advance. In a different work, Buchanan et al. (2003) investigated formation of atherosclerotic lesion in a model abdominal aorta. They particularly focused on deposition patterns of monocytes in their model geometry as an initiating step in lesion formation. In addition to deposition, they used LPT to study other path-dependent fields such as wall shear stress (WSS), wall shear stress gradient (WSSG), and oscillatory shear index (OSI). Very similar works have been done that use LPT to compute particle trajectories and qualify particle for deposition (Longest and Kleinstreuer, 2003, Longest et al., 2004).

In all of the mentioned studies, the overall process could be broken down to three steps. First step is calculating the flow field. This step is mostly done *a priori* using a CFD package. There is virtually no restrictions on the methods by which the flow is simulated. In certain cases, experimental results could be used instead of the simulation. The second step is to track particles. Particle seeding specifies the sites where particles are released in the domain. Afterwards, the trajectories are computed using a form of the LPT. The final step is qualifying certain localities depending on the computed trajectories and the kind of phenomenon under investigation.

It is interesting to note that many studies pointed out extreme sensitivity of wall parameters that are computed from particle trajectories (Barton, 1995, Kunov et al., 1996, Tambasco et al., 2002). The inaccuracies could be associated with three factors. Firstly, the resolution of the underlying flow field. Tambasco et al. (2002), Barton (1996) showed how individual trajectories could differ significantly with small changes in flow field. Secondly, the equations by which the trajectories

are computed. A full form of the equation used to model the motion of small solid spherical particle is called Basset-Boussinesq-Oseen (BBO). To save computational effort, many studies consider a reduced BBO as not all terms are always significant. Therefore, the simplified equation must be carefully validated to avoid inaccuracies. The third factor is the discretization and solution of the adapted BBO equation. The first and last factors are practical issues that could be tackled by careful choice of numerical settings. Therefore, for the rest of this section, the focus would be on the BBO equation in relation with particle dynamics in large arteries.

The Basset-Boussinesq-Oseen equation specifies unsteady motion of small particles in flow. The current form is the result of several extensions on the original work Maxey and Riley (1983), Saffman (1965). For the sake of completeness, the BBO equation follows with a small description of each term. For a detailed discussion on each term and their derivation under different flow conditions a number of references are available Clift et al. (1978), Maxey and Riley (1983), Ounis and Ahmadi (1990).

$$
\begin{aligned}
m_p \frac{d\mathbf{u}}{dt} = & && (3.3)\\
& - (m_f - m_p)\,\mathbf{g} && (3.4)\\
& + m_f \frac{D\mathbf{v}}{Dt} && (3.5)\\
& + \frac{m_f}{2} \frac{d\,(\mathbf{v}-\mathbf{u})}{dt} C_{\mathrm{a}} && (3.6)\\
& + 6\pi\mu a\,(\mathbf{v}-\mathbf{u})\,C_{\mathrm{d}} && (3.7)\\
& + 2\pi\rho_f a^2 \nu^{1/2}\,(\mathbf{v}-\mathbf{u}) \left|\frac{v_n}{x_n}\right|^{1/2} C_{\mathrm{sgn}} C_{\mathrm{s}} && (3.8)\\
& + 6\pi\mu a^2 \int_0^t \frac{d\,(\mathbf{v}-\mathbf{u})}{dt^*} \frac{dt^*}{[\pi\nu\,(t-t^*)]^{1/2}} C_{\mathrm{h}}. && (3.9)
\end{aligned}
$$

$$
\begin{aligned}
C_{\mathrm{a}} &= 2.12 - \frac{0.1344}{Ac^2 + 0.12}\\
C_{\mathrm{d}} &= 1 + 0.15 Re^{0.687}\\
C_{\mathrm{h}} &= 0.48 + \frac{0.52}{(Ac+1)^3}\\
Ac &= \frac{|\mathbf{v}-\mathbf{u}|^2}{2a\left|\frac{d(\mathbf{v}-\mathbf{u})}{dt}\right|}
\end{aligned}
$$

As shown, BBO defines the motion of a spherical particle with radius $a$, velocity $u$, and mass $m_p$ as a function of Reynolds number $Re$, displaced fluid mass $m_f$, velocity $v$, density $\rho_f$, and viscosity $\mu$. In this formulation of BBO, the buoyancy term, Eq. 3.4, denotes forces due to differences in density of the particle and the carrying fluid in presence of gravity. The pressure term, Eq. 3.5, takes into account the difference in the motion of the fluid if the particle was not present. As shown by its sign, it is in the direction of the fluid motion. The virtual mass, Eq. 3.6, specifies deceleration of the particle due to acceleration of the surrounding fluid. Drag force is denoted by Eq. 3.7. Drag is the important force acting on the particle due to viscosity of the fluid. In this formulation Stokes drag is modified according to Clift et al. (1978) to account to wake behind particles in larger Reynolds numbers (Barton, 1995). Saffman lift, Eq. 3.8 derived by Saffman (1965), accounts for the lift force on the particle due to velocity gradient across it. This term becomes significant in regions of high shear stress, e.g. in vicinity of walls. Finally, the Basset force, Eq. 3.9, defines the extra drag due to formation of a boundary layer around the particle. According to Barton (1995), this term is often ignored in computational studies.

### 3.1.2 Near-wall particle tracking

A standard LPT scheme is used to model dynamics of discrete tracers in the near wall regions. Within the SPH fluid iteration step $dt_{\texttt{sph}}$, equations of motion for each tracer $k$ are integrated with an appropriately smaller time step $dt$ in the range of $\tau_p$:

$$\dot{\mathbf{u}}_k = \mathbf{f}_{k,drag} + \mathbf{f}_{k,lubr} + \mathbf{f}_{k,lift} + \mathbf{f}_{k,coll}, \tag{3.10}$$

$$\dot{\mathbf{x}}_k = \mathbf{u}_k, \tag{3.11}$$

where $\mathbf{f}_{k,drag}$ is the Stokes drag acting on the leukocyte, $\mathbf{f}_{k,lubr}$ and $\mathbf{f}_{k,lift}$ are wall drag modifications, and $\mathbf{f}_{k,coll}$ is a stochastic force which takes into account collisions with red blood cells.

Integration of position $\mathbf{x}_k$ and velocity $\mathbf{u}_k$ is performed using a first-order Euler scheme:

$$\mathbf{x}_k^{n+1} = \mathbf{x}_k^n + dt\mathbf{u}_k^n, \tag{3.12}$$

$$\mathbf{u}_k^{n+1} = \mathbf{u}_k^n + dt\mathbf{f}_k^n, \tag{3.13}$$

where $n$ denotes the discrete sub-iteration time and $dt$ is the integration time step. In our case, $dt \leq \tau_p \ll dt_{\texttt{sph}}$ for stable integration. As the feedback arrow implies in

Fig. (3.5), force calculation and integration steps are repeated enough times to reach the next SPH time step. Intermediate steps guarantee stability of the numerical scheme. Increased time steps can be achieved, for example, by using second-order improved Euler predictor-corrector methods coupled with adaptive time step size Longest et al. (2004). However, accurate calculation of near-wall trajectories is only possible by application of extremely small time step sizes. The stability issue is automatically solved as a result of such choice. As these issues have been overcome by a first-order Euler scheme, using a high-order tracking scheme does not seem to be worthwhile for this problem.

### Force calculation

Explicit form for the forces acting on the tracer particles in Eq. (3.11) follow from Longest et al. (2004). The Stokes drag for the $k$-th tracer is

$$\mathbf{f}_{k,drag} = \frac{1}{\tau_p}\left(\mathbf{v}_k - \mathbf{u}_k\right), \tag{3.14}$$

where $\mathbf{v}_k$ is the local SPH fluid velocity interpolated on the tracer position $\mathbf{x}_k$.

In the limit of $\mathrm{Re}_p = \rho_p U d_p/\mu \ll 1$ near wall drag modification $\mathbf{f}_{k,lubr}$ is derived by Cox and Brenner (1967), Goldman et al. (1967a,b), Loth (2000):

$$\mathbf{f}_{k,lubr} = \frac{1}{\tau_p}\left[\left(\left(\mathbf{v}_k - \mathbf{u}_k\right)\cdot\hat{\mathbf{n}}\right)\left(\frac{1.1}{\frac{h_p}{a_p}-1}\right)\hat{\mathbf{n}} + \left(\left(\mathbf{v}_k - \mathbf{u}_k\right)\cdot\hat{\mathbf{t}}\right)\left(\frac{0.7a_p}{h_p}\right)\hat{\mathbf{t}}\right], \tag{3.15}$$

in which $h_p$ is wall-normal distance and $a_p$ tracer's radius. Also, $\hat{\mathbf{n}}$ and $\hat{\mathbf{t}}$ denote wall-normal and wall-tangential unit vectors, respectively.

Saffman lift Saffman (1965) is dependent on the surrounding flow shear. Therefore, it increases in the near-wall region where tracer-wall separation is in the order of tracer radius. As a tracer approaches solid wall in the limit, Saffman lift increases to an extent that separates the tracer from the wall Longest (2002). Hence, this term is derived assuming a tracer-wall separation in the order of tracer radius,

$$\mathbf{f}_{k,lift} = \frac{-\rho a_p^2}{m_p}\left[u_s^2 \cdot I\left(\frac{h_p}{a_p}, \frac{\dot{\gamma} a_p}{u_s}\right)\right]\hat{\mathbf{n}}, \tag{3.16}$$

where $m_p$ is tracers' mass and $u_s$ wall-tangent slip-velocity,

$$u_s = \left(\mathbf{u}_k - \mathbf{v}_k\right)\cdot\hat{\mathbf{t}}. \tag{3.17}$$

Defining $\kappa = a_p/h_p$, $\Lambda = \dot{\gamma} a_p/u_s$, and $\dot{\gamma} \approx \frac{\mathbf{u}_k \cdot \hat{\mathbf{t}}}{h_p}$ the value of integral $I$ for a sphere reads:

$$\begin{aligned} I\left(\frac{h_p}{a_p}, \frac{\dot{\gamma} a_p}{u_s}\right) &= \left[1.7631 + 0.3561\kappa - 1.1837\kappa^2 + 0.845163\kappa^3\right] \\ &\quad - \left[\frac{3.24139}{\kappa} + 2.6760 + 0.8248\kappa - 0.4616\kappa^2\right] \Lambda \\ &\quad + \left[1.8081 + 0.8796\kappa - 1.9009\kappa^2 + 0.98149\kappa^3\right] \Lambda^2, \end{aligned} \tag{3.18}$$

which is an approximation to the numerical integration of asymptotic results from Cherukat and McLaughlin (1994).

Dispersional effects induced by the RBCs on leukocyte $k$ are represented by a random force $\mathbf{f}_{k,coll}$. This force can be taken into account by applying a random displacement, $\Delta\mathbf{x}_k$ produced by $\mathbf{f}_{k,coll}$ during one time step $dt$ and are generated randomly according to the following Gaussian probability distribution,

$$p\left(\Delta x_k^\alpha, \Delta t\right) = \frac{1}{2\sqrt{\pi D_p \Delta t}} \exp\left(\frac{-\Delta x_k^{\alpha 2}}{4 D_p \Delta t}\right), \tag{3.19}$$

where $\alpha = x, y, z$ denotes the Cartesian component and $D_p$ is the effective dispersion coefficient. Generated displacements are then superimposed on tracer positions.

In case of simplification of BBO, it is important to carefully consider validity of the reduced model. Eq. (3.10) in full form is discussed in extent in Maxey and Riley (1983). Compared to the full form presented above, virtual mass, pressure, and Basset terms are neglected. A thorough investigation of the relative significance of each term in a laminar flow over a backward-facing step is performed in Barton (1995). According to their findings, after drag and gravity, the pressure term becomes important for neutrally buoyant tracers, and the Saffman lift is significant near walls. The pressure term is, however, not in the same order as the other terms, since Eq. (3.10) is applied only at distances very close to walls.

### 3.1.3 LPT verification

In order to validate the final implementation of near-wall Lagrangian tracking, a pure LPT code is developed that uses exactly same routines for integration of tracers. This component initially fills the entire domain with tracers and does not integrate the base flow but reads it as a pre-computed input. To test the code, streamlines and tracer trajectories in a backward-facing step geometry with Re=400,

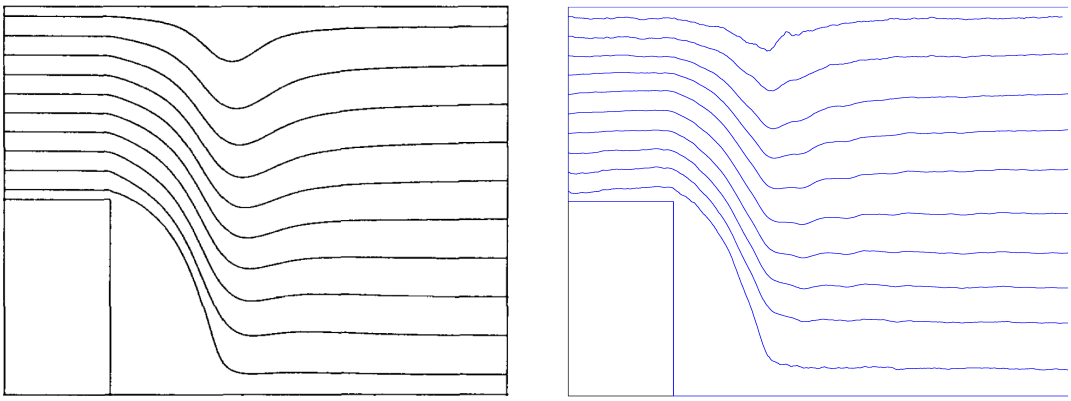

(a) Barton (1995) (b) SPH flow field

Figure 3.1: streamlines from 10 starting positions - Re=400

from Barton (1995), are presented in Figures 3.1 and 3.2. 3.1a and 3.1b show a good agreement; however, some dissimilarities are apparent. One must take this difference between velocity fields into account when comparing tracer trajectories. 3.2a shows trajectories of 10 tracers starting from the entrance of the channel. Figure 3.2b shows trajectories from the same starting position using SPH base flow and Barton's particle tracking. Therefore, these pathlines demonstrate the differences between base flows in SPH and Barton (1995), as mentioned before. In 3.2c, trajectories are calculated according to Longest et al. (2004). The only difference is that the deposition mechanism is still present, meaning that a particles deposits if its wall distance is less than or equal to its radius. Finally, in Figure 3.2d the deposition mechanism is left out and particles are free to move even at distances very close to the wall. Apart from the differences between base flows, which is not the concern here, trajectories seem to match very accurately.

## 3.2 Particle-tracer coupling

In this section we describe in detail the coupling between the solutions for the leukocyte concentrations obtained from the continuum phase and from the discrete phase. Solutions must be coupled together at the interface between the two domains enforcing conservation of mass. Several continuum-particle hybrid coupling methods have been developed during the past two decades Koumoutsakos (2005), Delgado-Buscalioni and Coveney (2003), De Fabritiis et al. (2006), Fedosov and Karniadakis

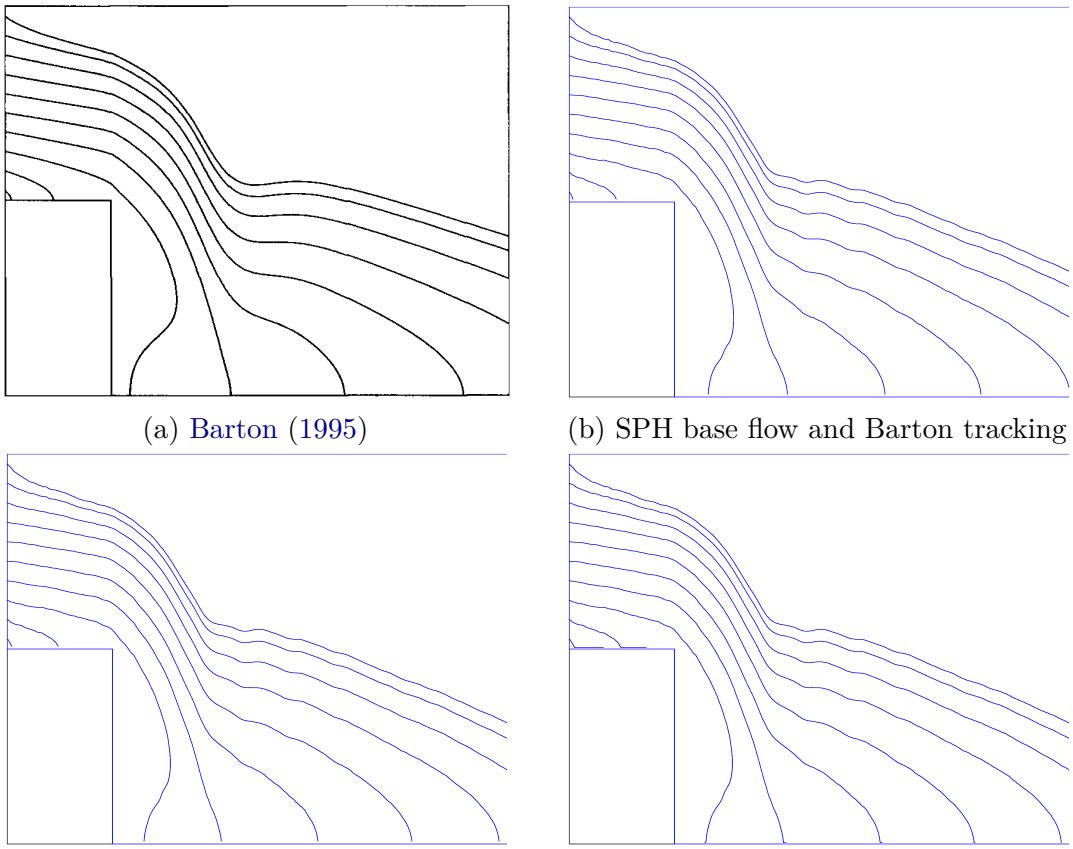

(a) Barton (1995)

(b) SPH base flow and Barton tracking

(c) SPH base flow, Lubrication forces close to walls, and near-wall deposition

(d) SPH base flow, Lubrication forces close to walls

Figure 3.2: tracer trajectories from 10 starting positions - Re=400, Stk=0.01

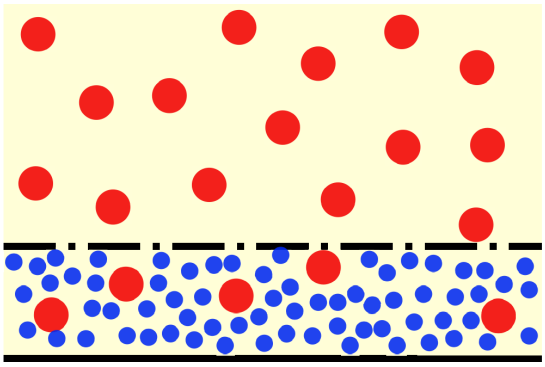

Figure 3.3: Near-wall configuration - red circles denote SPH particles, blue ones are tracers. Near-wall interface and wall are shown with dash-dot and solid lines, respectively.

(2009), many of which have received significant attention. In this work we aim for a two-way coupling scheme that strictly conserves tracers' mass. Our coupling scheme is based on communication of tracer concentration data at the near-wall interface. The interface, shown with dash-dot line in Fig. (3.3), is normally within a few tracer diameters from the wall. This distance is the range that tracers start to feel the presence of the wall Loth (2000), thus experience different dynamics than in the bulk. Therefore, a specific particle tracking for tracers is performed in the near-wall region. Conservation of tracer mass is guaranteed through definition of an integer-valued tracer count field on SPH fluid particles. This definition allows an efficient straightforward coupling scheme described in the following (according to Fig. (3.5)):

1. *Initialization*
   Each SPH particle $i$ is assigned an integer number of tracers $N^i_{\texttt{tracer}}$. This number indicates how many tracers SPH particle $i$ is carrying. Initialization can be performed at any time, therefore, it allows full control over introduction of tracers to the domain: seeding from multiple sources, arbitrary time/space-dependent injection, etc. Taking advantage of our Lagrangian framework, it is also easy to link initialization of tracers to domain boundary conditions. Uniform seeding from inlet is carried out by resetting $N^i_{\texttt{tracer}}$ to an initial value at inlet, hence a uniform concentration. Inhomogeneities in concentration develop from coupling with flow. As a result, realistic cases such as margination of leukocytes Fedosov et al. (2012) could be handled through assignment of higher WBC concentrations in the vicinity of wall boundaries.

2. *Extraction*
   As already discussed, actual tracers are only created in the near-wall region. Therefore, if SPH particle $i$ enters the near-wall region $N^i_{\texttt{tracer}}$ new tracers are extracted from it, as shown in Fig. (3.4a). These new tracers are created in the near-wall region according to a desired distribution. The distribution function is chosen with respect to SPH resolution and tracer size in order to obtain a physical continuous change in near-wall tracer concentration along the wall. Velocities are initialized according to the position of new tracers relative to wall. Total tracer mass is conserved as the total number of tracers, i.e. total number of tracers in the near-wall region $N_{\texttt{tracer}}$ plus the number of tracers carried by SPH particles $\sum N^i_{\texttt{tracer}}$, stays the same before and after extraction:

$$\begin{aligned} N_{\texttt{tracer}} &:= N_{\texttt{tracer}} + N^i_{\texttt{tracer}} \\ N^i_{\texttt{tracer}} &:= 0. \end{aligned}$$

3. *Discrete Phase Integration*
   LPT is performed for tracers in the near-wall region. Time step size is small enough to guarantee stability of the integration scheme.

4. *Insertion*
   A tracer that leaves the near-wall region should be deleted and inserted back into a nearby SPH particle as in Fig. (3.4b). The SPH particle that receives the tracer does not have to necessarily be the nearest particle. In fact, it is chosen according to a random distribution function based on the inverse particle-tracer distance. Therefore, artificial jumps of tracer count on a SPH particle compared to its neighboring particles, due to the discrete nature the coupling scheme, is smoothed out. Indeed, mass is preserved:

$$\begin{aligned} N_{\texttt{tracer}} &:= N_{\texttt{tracer}} - 1 \\ N^i_{\texttt{tracer}} &:= N^i_{\texttt{tracer}} + 1. \end{aligned}$$

Computational cost of a full LPT simulation with sufficiently large number of tracers is overwhelming Longest et al. (2004). The particle-tracer coupling method proposed in this work considerably reduces this cost while staying dynamic and well-tuned for a range of realistic vascular setups. More details will be discussed in the results section.

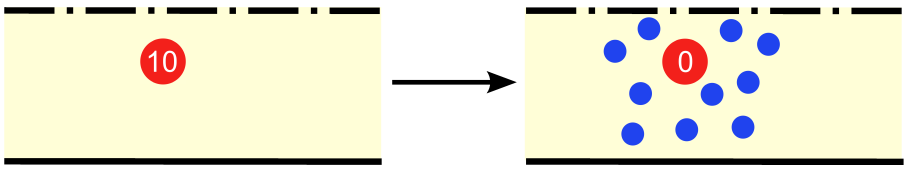


(a) Extraction - as a SPH particle which carries 10 tracers enters the near-wall region, 10 new traces are randomly created around it and the SPH particle is assigned zero tracers.

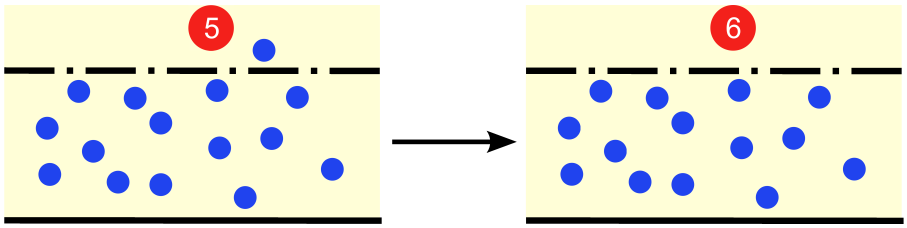


(b) Insertion - as a tracer leaves the near-wall region, it is inserted into a nearby SPH particle. The SPH particle is assigned an additional tracer.

Figure 3.4: Fundamental operations at interface for particle-tracer coupling - solid line represents wall, dash-dot line near-wall interface. Red circles represent SPH particles and blue circles tracer particles.

### 3.2.1 Code structure and algorithmic complexity

The overall structure of the numerical scheme is presented in Fig. (3.5). Time integration loop starts after the initialization steps for both SPH particles and tracers. The first step in each loop is to solve the base flow by integrating the SPH equations of motion, Eq. (2.14). Skipping details of SPH integration, tracer modeling steps, marked with a dashed block, take place in the following order:

1. *Particle-Tracer Coupling - Extraction*: quantities are communicated from SPH particles approaching the near-wall region to tracers.

2. *Force Calculation*: according to local flow field, forces acting on each tracer are calculated.

3. *Integration*: position and velocity of tracers are integrated. At the end of this step tracers are re-distributed in the domain according to their new position. Decomposition is implemented using the external PPM library Sbalzarini et al. (2006).

4. *Particle-Tracer Coupling - Insertion*: post-integration quantities are communicated from tracers to particles (two-way coupling).

An additional remark on the computational complexity of these operations is in order. Complexity of standard SPH, using optimization techniques such as a linked list cell method, is $O\left(N_{\texttt{sph}} * M\right)$, with $M$ being average number of SPH particles in a searching cell. As for tracers, initialization of tracer concentration is linear with the number of fluid particles $O\left(N_{\texttt{sph}}\right)$. It is performed along with initialization of other SPH quantities and therefore does not cause additional costs. Also, for cases such as injection from an inlet and time/space-dependent concentration, re-initialization takes place with imposition of boundary conditions for SPH particles, hence no costs. Extraction of tracers requires locating fluid particles relative to walls, which means that a linear operation in $N_{\texttt{sph}}$ is required to calculate the wall distance for each SPH particle. This step can be performed within the usual SPH force calculation. The force calculation for tracers requires the fluid velocity at each tracer position. Complexity of this operation should be $O\left(N_{\texttt{sph}} \times N_{\texttt{tracer}}\right)$ without and $O\left(M \times N_{\texttt{tracer}}\right)$ with cell list. Considering that $N_{\texttt{tracer}} \gg N_{\texttt{sph}}$, this process will dominate the complexity of the method. To overcome this, SPH velocity is interpolated to the near-wall interface grid with $N_{\texttt{int}} = O\left(N_{\texttt{sph}}^{\frac{n_d-1}{n_d}}\right)$ points, $n_d$ being

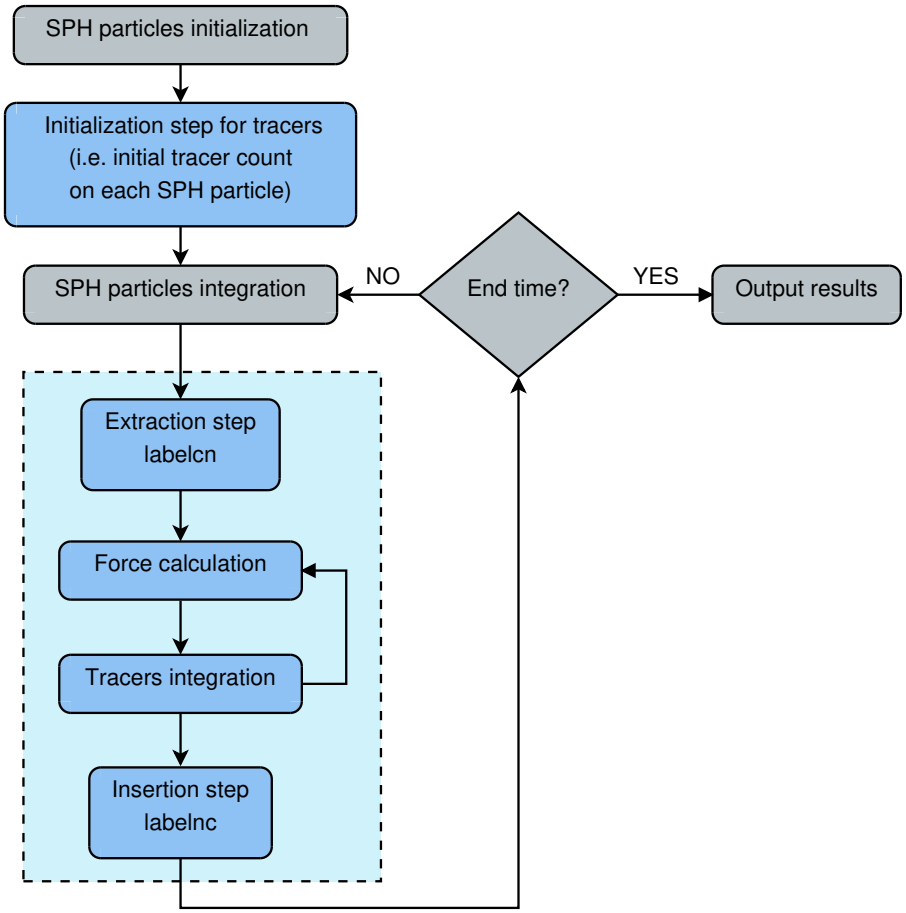


Figure 3.5: Flowchart of the Coupling code - steps regarding the coupling of tracers are marked with the dashed block.

number of dimensions, therefore $O\left(M \times N_{\texttt{int}}\right)$ operations. Assuming a linear velocity profile in the near-wall region, velocities at tracer position are determined with $O\left(N_{\texttt{tracer}}\right)$ operations. This assumption is safely valid due to the small width of the near-wall region relative to SPH resolution.

Finally, insertion needs assignment of probabilities to $M$ SPH particles within the cutoff radius of every tracer which leaves the near-wall region. Considering resolution of SPH particles compared to the width of the near-wall region, $M$ is small. As the number of tracers that leave the near wall region within each iteration is an order of magnitude smaller than $N_{\texttt{tracer}}$, it is safe to conclude that the insertion cost is far less than $O\left(N_{\texttt{tracer}}\right)$.

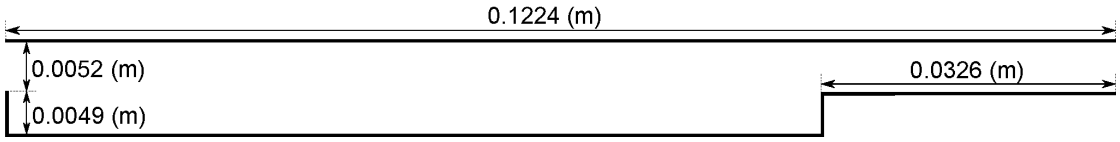


Figure 3.6: Backward-facing step geometry used for comparing results. Lengths are presented in meters.

## 3.3 Deposition patterns with multiscale model

In this section, deposition patterns from the particle-tracer multiscale model are discussed. For this purpose, a backward-facing step (BFS) geometry is used. The channel, as shown in Fig. (3.6), is defined based on the BFS geometry in Karino and Goldsmith (1977). The top and bottom walls are treated as no-slip and a periodic boundary condition for fluid particles is applied on the left and right boundaries. Dimensions of the domain are summarized in Table 3.1. Length of the channel is chosen large enough to reach a fully developed flow before the second step.

Table 3.1: BFS geometry

| BFS geometry | |
|---|---|
| length of the channel | 0.1224 $(m)$ |
| entry height of the channel | 0.0052 $(m)$ |
| length of each step | 0.0326 $(m)$ |
| height of each step | 0.0049 $(m)$ |

Fluid parameters are summarized in Table 3.2. For simplicity, the carrying fluid is assumed to have similar parameters as water. Application of blood as carrying fluid with a viscosity only four times larger than water would certainly not affect results qualitatively. Flow Reynolds number is chosen to be 23, the average Reynolds number in the sudden expansion geometry of Karino and Goldsmith (1977). It is based on twice the height of the inlet and the velocity at the middle of the inlet channel. With these parameters, stability conditions on the SPH time step prescribes $dt_{\texttt{sph}}$ = 2.13e-3 $(s)$. Tracers are assumed neutrally buoyant, and radius is in the same range as WBCs. The resulting momentum response time, $\tau_p$ =1.12e-5 $(s)$, is taken to be the time step size for tracer integration.

Additionally, a diffusion coefficient is selected to match the effective dispersion of

Table 3.2: flow and tracer parameters

| flow parameters | |
|---|---|
| density | 1000 $(kg/m^3)$ |
| viscosity | 0.001 $(Pa \cdot s)$ |
| timestep size | $\approx$ 2.13e-3 $(s)$ |
| **tracer parameters** | |
| radius | 7.1e-6 $(m)$ |
| density | 1000 $(kg/m^3)$ |
| diffusion coeff. | 1.5e-9 $(m^2/s)$ |
| momentum response time | $\approx$ 1.12e-5 $(s)$ |
| timestep size | $\approx$ 1.12e-5 $(s)$ |

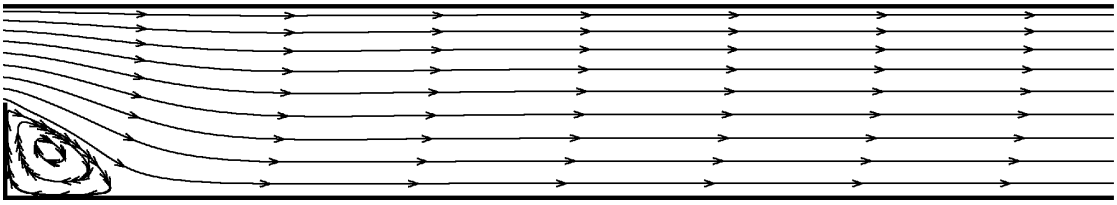

Figure 3.7: Flow streamlines over the backward-facing step geometry for Re = 23.

WBCs (see subsec. 3.3.2).

Although the backward-facing step is geometrically simple, it has the advantage that it incorporates several complex flow features observed *in vivo* such as flow expansion, detachment, attachment and a recirculation zone (see Fig. (3.7)) and therefore it represents the ideal case for clean comparisons.

### 3.3.1 Validation code

Results of the particle-tracer coupling scheme are validated using a second code developed specifically for this purpose. The *Validation* code is implemented in Fortran and fully parallelized using MPI. It uses snapshots of velocity field, obtained by ANSYS Fluent, as input to integrate tracer trajectories *over the entire fluid domain*. Different modes of initialization and boundary conditions are available. The Validation code has been mainly developed to solve some numerical issues faced by available commercial packages such as ANSYS CFX. A comparison of run times

between a similar Fortran code and CFX4.4 particle tracking algorithms for tracking of 500000 particles revealed that the former needs about 45 hours to complete while the latter take about 2000 hours Longest et al. (2004). We also tried to simulate similar scenarios with ANSYS Fluent, but the same difficulties were faced. Moreover, the in-house validation code uses an identical particle tracking routine, thus decoupling the comparison outcome from potential discrepancies between tracking models. In any case, the particle trajectories from the Validation code were compared to those presented in Barton (1995), and the results matched closely.

Fig. 3.8 demonstrate how concentration field evolves over time. Note that the concentration field is initially zero everywhere in the domain.

### 3.3.2 Diffusion coefficient

The diffusive behavior of the tracers in both simulation methods, SPH with particle-tracer coupling and Validation, are investigated by calculating the mean squared displacement (MSD) defined by:

$$\mathrm{MSD}(t) = \langle (\mathbf{r}(t) - \mathbf{r}(0))^2 \rangle, \tag{3.20}$$

where $\langle\rangle$ denotes averaging over all particles. For the Validation code, at zero flow velocity, an ensemble of 100 tracer particles evolve according to $\mathbf{f}_{coll}$ only and undergo a random walk process characterized by a diffusion coefficient $D_p = 1.5 \times 10^{-9} m^2/s$ in 2D. The simulation performs 10000 steps with $dt = 1.12 \times 10^{-3} s$. The calculated diffusion coefficient from the mean square displacement data, Fig. (3.9a), is $1.5 \times 10^{-9} m^2/s$ and matches the input parameter. Displacement steps are limited to 1000.

In the SPH simulation with incorporated momentum fluctuations, choosing $dt = 4.53 \times 10^{-3} s$, a similar diffusion coefficient for the fluid particles is achieved by taking $k_B T_{eff} = 1.9 \times 10^{-12} m^2 kg/s^2$ in Eq. (2.19). The resulting diffusion coefficient, Fig. (3.9b), equals $1.5 \times 10^{-9}$. In this case, in addition to limiting the maximum number of displacement steps to 1000, those with less than 100 steps are not considered in fitting. This is to avoid the ballistic regime and reach the diffusive regime which defined $D$.

### 3.3.3 Particle deposition

Excessive adhesion and deposition of leukocytes are thought to be relevant in the initiation of atherosclerosis. Exact conditions under which such abnormal deposition

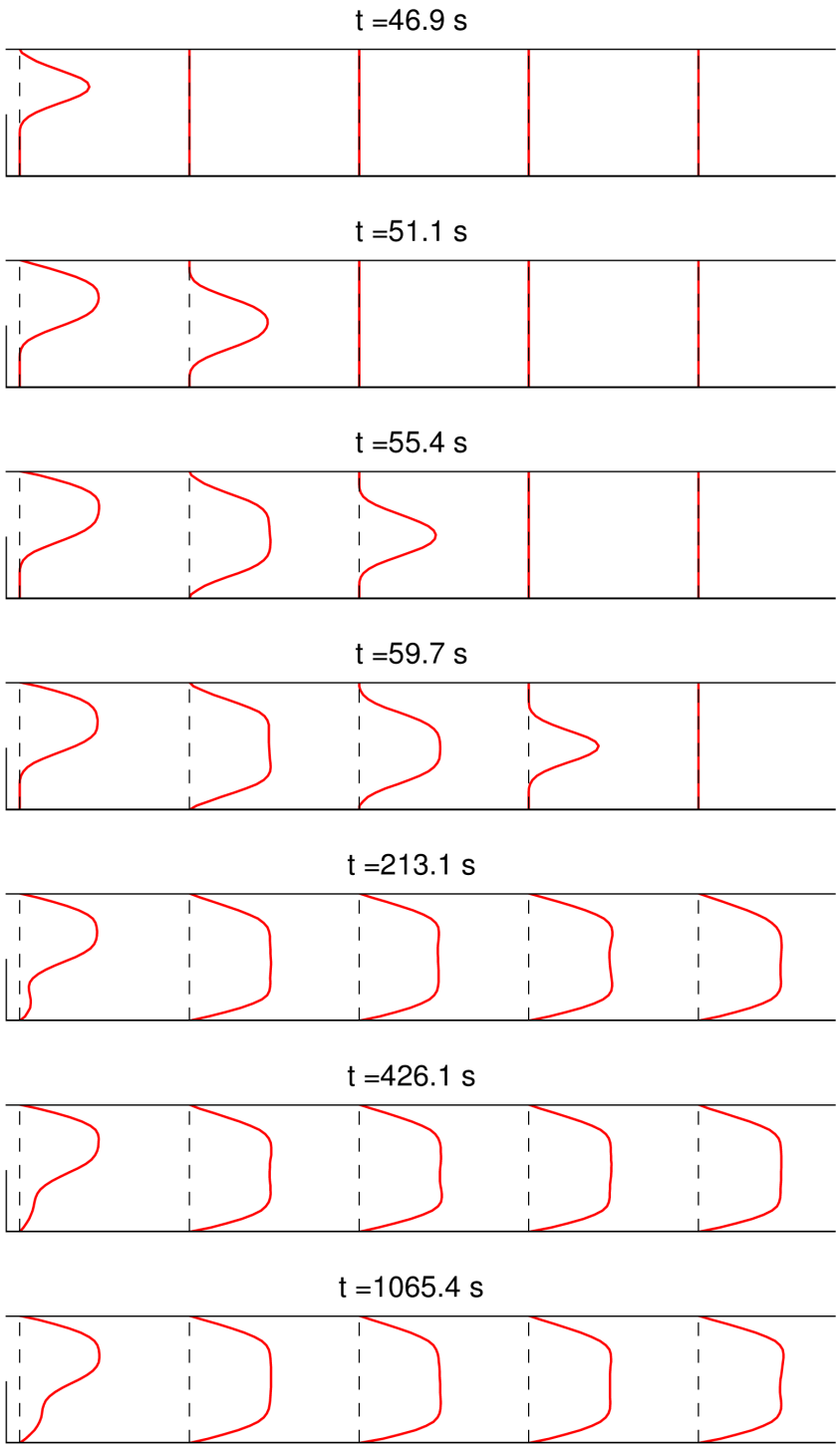


Figure 3.8: Evolution of concentration field for flow over the backward-facing step

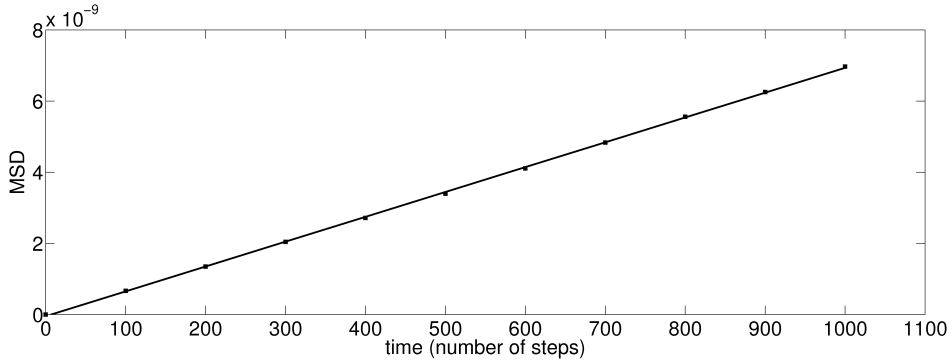


(a) Validation code - Only displacements with a maximum of 1000 steps are considered. The slope of line divided by $4 \times dt (= 4.48 \times 10^{-3})$ rounds to $1.5 \times 10^{-9}$.

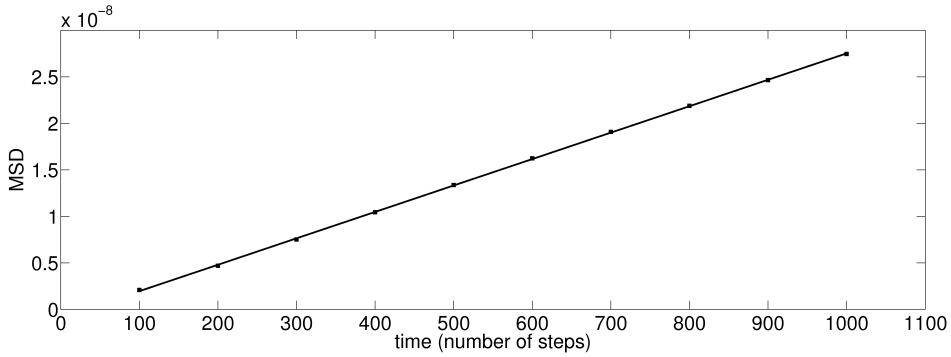


(b) SDPD code - Only displacements with a maximum of 1000 and a minimum of 100 steps are considered. The slope of line divided by $4 \times dt (= 1.812 \times 10^{-2})$ rounds to $1.5 \times 10^{-9}$.

Figure 3.9: Mean square displacement vs. time

takes place is not yet completely understood, but likely involves some sort of dysfunction of the endothelium in specific regions of the vasculature. However, it is still possible to define a deposition criterion for tracers based purely on the hemodynamics in the vicinity of the wall. Our criterion is based on wall normal distance. We assume that the probability of deposition is zero if a tracer is not located within a minimum distance from the wall. This distance is chosen to be one tracer diameter from the wall (center to wall). It should be noted that since this work is concerned with the disease in its early stages, the formation of macroscopic plaques, which takes years, does not need to be taken into account. Furthermore, plaque formation is a complex biological process occurring in the intima of the arterial wall, which is far more complex than simple accumulation and build up of leukocytes.

Since we work with discrete tracers in the near-wall region, the deposition criterion can be easily adapted according to specific requirements; for example, a deposition probability can be prescribed for tracers within the deposition range and Monte-Carlo acceptance-rejection methods can be used. A local elevation in deposition probability, for example, can then be imposed to model atherosclerotic lesions. This will be discussed in more detail in Sec. 3.5.

### 3.3.4 Near-wall deposition profile

Instantaneous deposition profile of tracers along walls is presented and compared between the coupling and validation codes in Fig. (3.10). At the inlet, tracers are uniformly injected into the domain. The number of tracers is controlled through definition of a tracer number parameter $N^i_{\texttt{tracer}}$ which defines the local tracer concentration. In case of the coupling code, this parameter defines the initial number of tracers carried by every SPH particle and, depending on the desired initial conditions, can be in general not constant. In the validation code, the same number of tracers is enforced by regulating the injection rate at the inlet.

Deposition profile shows two maxima (Fig. (3.10b)). Both peaks occur at sites of low wall shear stress; the first at the separation point slightly under the edge of the step and the second at the reattachment point. The first peak is considerably larger in size compared to the second. This is due to the downward flow at the edge of the step which strongly pushes tracers toward the wall. Furthermore, due to the large wall shear stress gradients around the separation point, this peak is very sharp. It is, therefore, extremely difficult to reproduce identical deposition profiles around this point. Comparison of profiles reveals that our method successfully captures the position and size of this peak. Moving towards the corner, results show qualitative

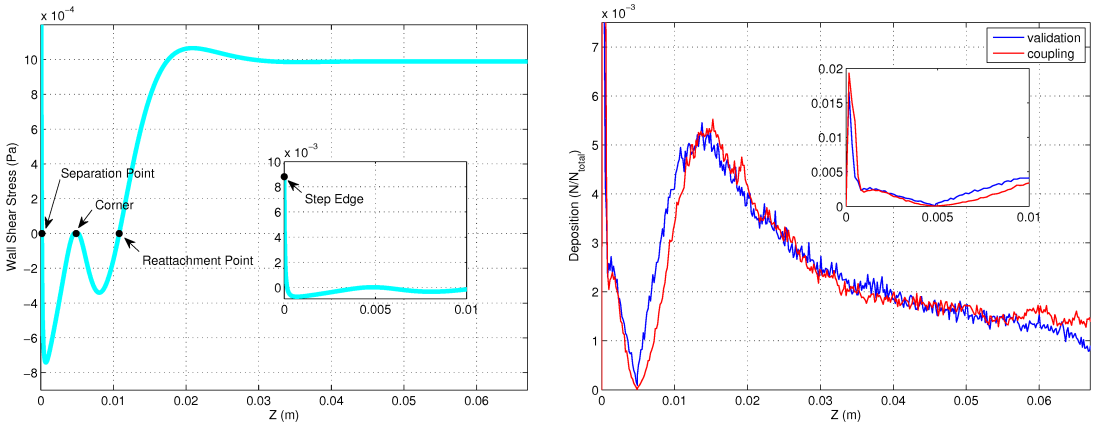


(a) Wall shear stress (b) Deposition profile

Figure 3.10: Wall shear stress (top) and tracer deposition profile (bottom) along walls in the BFS geometry - Tracer deposition is compared between coupling and validation codes. $Z$ represents wall-tangential coordinate starting from the edge of the step at inlet.

agreement; however, the validation code predicts a sharper drop after the separation point (Fig. (3.10b) subplot).

Increasing from zero at the corner, the deposition profile experiences a second peak around the reattachment point where wall shear stress is again close to zero. After this point, tracers tend to deposit less due to increasing wall shear stress. Even though the wall shear stress is zero at the corner, no deposition takes place. This is because tracers injected from the inlet have a very low chance of reaching the corner.

Considering the noisy nature of the solution, results show close agreement. The noise could be eliminated by averaging deposition profiles over time. However, snapshot data feature information on statistical accuracy of results which demonstrate the quality of near-wall profiles. This is particularly important in case of unsteady problems where time averaging is not an option. Hence, we present instantaneous wall quantity profiles in this work. Slight discrepancies are observed in the recirculation zone along the bottom wall which reflect sensitivity of solutions to the presence of a sharp edge (ill-conditioned problem); this however would not occur in realistic arterial geometries. Also, it is known that particle trajectories, and quantities derived from particle trajectories, are very sensitive to velocity field Tambasco et al.

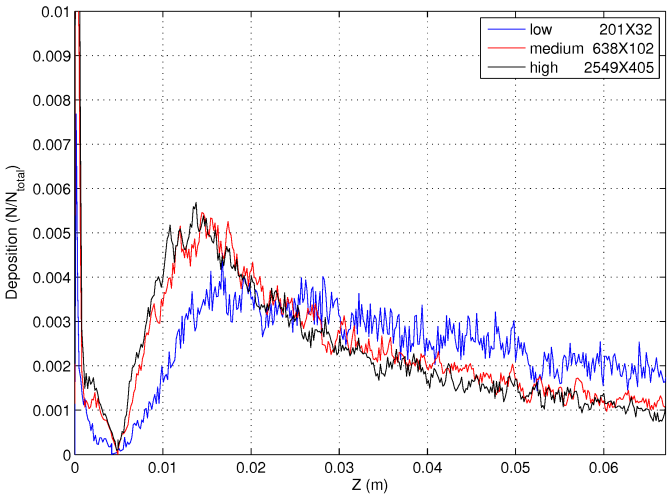


Figure 3.11: Comparison of wall deposition profiles for the validation code with high and low resolution for velocity field.

(2002), Prakash and Ethier (2001). We reached a similar conclusion by running the validation code with different velocity field resolutions (see Fig. (3.11)). Even though the velocity field is converged at a resolution as low as $201 \times 32$ grid points, the corresponding wall deposition profile is considerably different than converged profiles. This highlights the importance of full convergence in the velocity field for the accurate determination of deposition profiles. In the same manner, convergence of deposition profiles in number of SPH particles is demonstrated for the *coupling* code in Fig. (3.12). One should notice that the overall number of tracers is kept the same in results presented in Figs. (3.11) and (3.12), therefore, profiles are not smoother in higher resolutions of velocity field.

Convergence behavior of the coupling and validation codes in number of tracers is presented in Figs. (3.13) and (3.14), respectively. Near-wall deposition profiles converge to smoother curves as the resolution increases. A more quantitative investigation is carried out by defining the norm of the deposition residual as:

$$\langle N_{\mathtt{dep}} \rangle = \sqrt{\frac{1}{N_{\mathtt{int}}} \sum_{z=1}^{N_{\mathtt{int}}} \frac{1}{N_{\mathtt{avg}}} \sum_{n=1}^{N_{\mathtt{avg}}} \left( N^n_{\mathtt{dep}}(z) - \bar{N}_{\mathtt{dep}}(z) \right)^2}, \tag{3.21}$$

where $N^n_{\mathtt{dep}}(z)$ is the number of deposited tracers at interface cell $z$ at iteration $n$. $N_{\mathtt{int}}$ is the number of interface cells (same as interface grid), $N_{\mathtt{avg}}$ is the number of

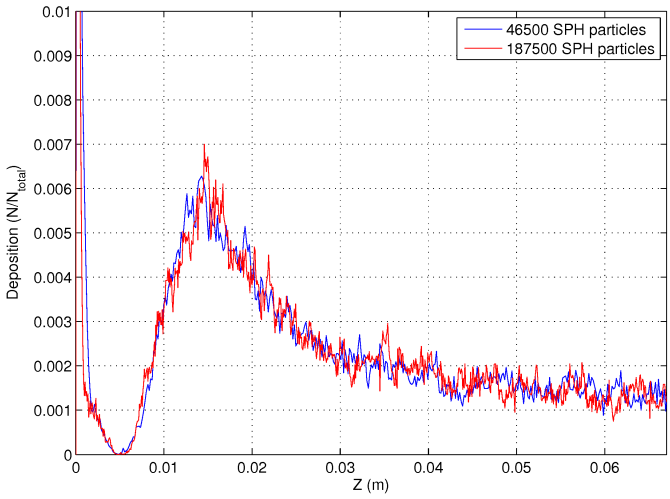


Figure 3.12: Comparison of wall deposition profiles for the coupling code with high and low resolution for velocity field.

iterations used for averaging, and $\bar{N}_{\mathtt{dep}}(z)$ is the average deposition count:

$$\bar{N}_{\mathtt{dep}}(z) = \frac{1}{N_{\mathtt{avg}}} \sum_{n=1}^{N_{\mathtt{avg}}} N^{n}_{\mathtt{dep}}(z). \tag{3.22}$$

Monitoring $\langle N_{\mathtt{dep}} \rangle$ over time, Figs. (3.13b) and (3.14b), reveals that higher tracer resolutions are associated with smaller residuals.

## 3.4 Computational gain

Computational gain of the coupling method over the validation method is investigated by comparing the number of tracers simulated in each scenario (Fig. (3.15)). In order to have statistically comparable results, both strategies (coupling and validation) are run long enough to reach approximately the same number of tracers at the steady-state in the near-wall region. Evolution of near-wall tracer count over time is presented in Fig. (3.16). In both cases, the number of tracers increase from the initial value of zero and reaches steady state at around the same time. At each resolution, both methods end up with approximately the same number of tracers along walls at steady state (Near-Wall Count column in Table 3.3). Near-wall tracer count is averaged over time to account for differences in the convergence behavior

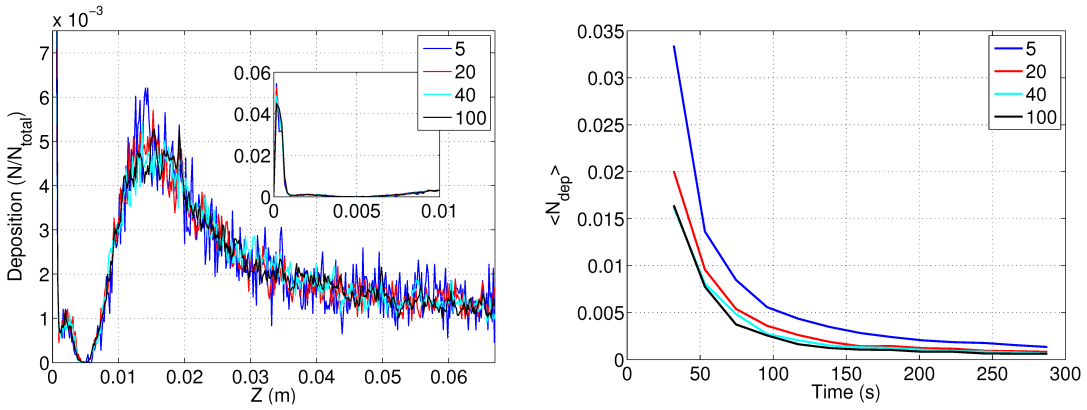


(a) Deposition profile (b) Norm of residual over time

Figure 3.13: Convergence behavior of coupling code at different resolutions.

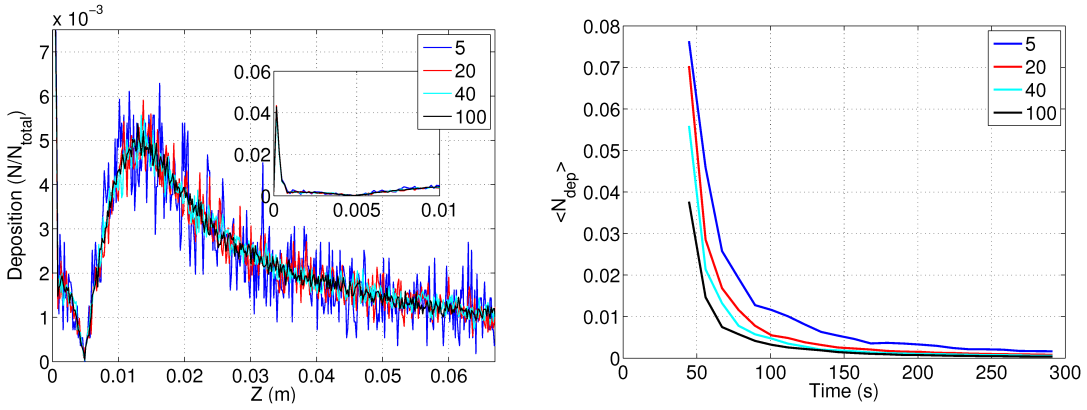


(a) Deposition profile (b) Norm of residual over time

Figure 3.14: Convergence behavior of validation code at different resolutions.

of the two approaches. The gain factor is determined by dividing the total number of tracers in the domain (Total Count column in Table 3.3) and correcting the result by the near-wall count ratio. As shown in Table 3.3, at each resolution the validation code requires at least 47 times more tracers to reach the same number of tracers in the near-wall region at steady state.

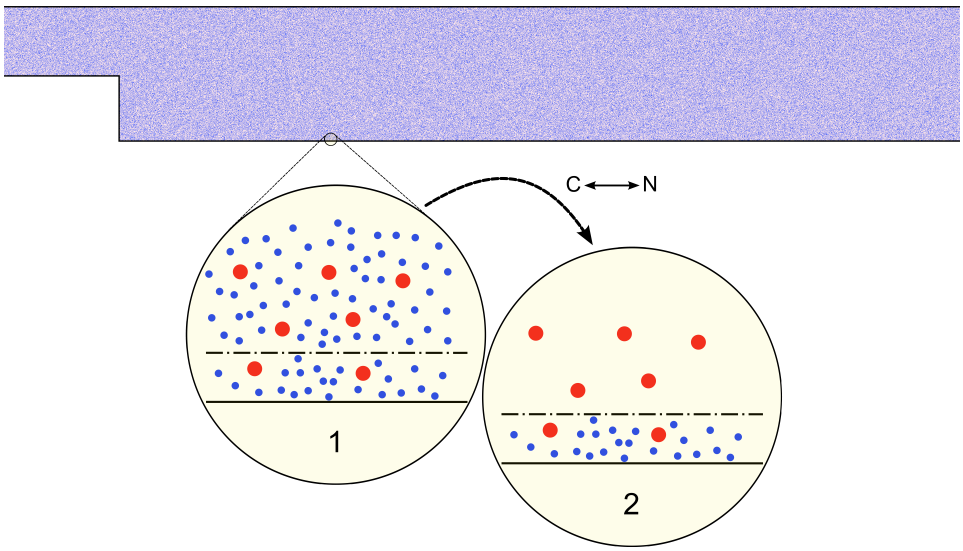


Figure 3.15: Near-wall region in the presented BFS geometry. *Validation* code computes trajectories of tracers anywhere in the domain (circle 1). However, exchange of concentration quantity at the interface makes elimination of tracers in the bulk possible. Therefore, *Coupling* code deals with tracer trajectories only in the near-wall region (circle 2).

Gain factor is independent of the resolution. Since the number of fluid particles is normally prescribed by physical constraints and accuracy goals of the application, a resolution-dependent gain factor would not be desirable. Hence, the coupling method does not restrict degrees of freedom of the problem to deliver the promised speedup. Instead, the gaining factor depends only on the ratio between the physical volumes representing the near-wall region and the vessel control volume. Obviously, in case of three-dimensional macroscopic vessels, this gaining factor can be substantially larger.

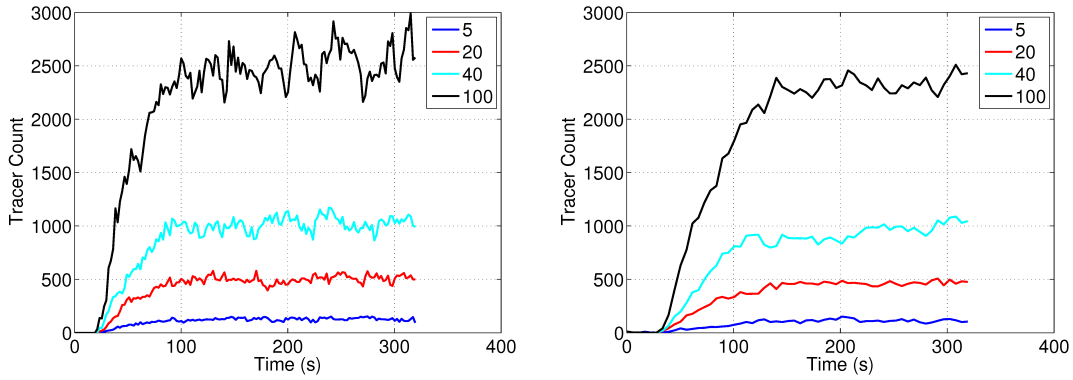


(a) Coupling method (b) Validation method

Figure 3.16: Evolution of near-wall tracer count over time at different resolutions.

Table 3.3: Time-averaged tracer count for each code at different resolutions

| Resolution | Method | Total Count | Near-Wall Count | Gain Factor |
|---|---|---|---|---|
| 5 | coupling<br>validation | 806<br>32034 | 106<br>85 | $\approx 49$ |
| 20 | coupling<br>validation | 3292<br>128730 | 418<br>349 | $\approx 47$ |
| 40 | coupling<br>validation | 6424<br>256571 | 847<br>722 | $\approx 47$ |
| 100 | coupling<br>validation | 16156<br>641238 | 2103<br>1765 | $\approx 47$ |

## 3.5 Local lesion

In real applications, the deposition mechanism is closely related to surface properties of both the particles and the walls. Variations in these attributes could, in a complex way, lead to abnormal alterations in deposition pattern and adhesive properties of the wall. As an example, in initiating stages of atherosclerosis, excessive adhesion of WBCs to the endothelium occurs as a results of upregulation of adhesive molecules in certain sites (endothelial dysfunction). In order to examine capabilities of the coupling method in delivering correct results in nontrivial cases, wall deposition rates have been manipulated in specific locations. Normally, tracers, providing they are close enough, have an identical chance of deposition at any site in the domain. In this case, we model formation of a lesion at a certain region by assigning

a higher chance of deposition to tracers in that vicinity i.e. we are assuming that the endothelium in this location has become dysfunctional. The lesion site is chosen to be of low hydrodynamic significance, meaning that we intentionally take a region with a low deposition value.

For the deposition profiles presented in Fig. (3.17) a 30% chance of deposition is set all over the domain with a continuous increase to hit 100% chance at $Z = 0.042$. As expected, both methods show a second peak at the maximum deposition position. The new peak is as large as the one at the reattachment point, however they form for different reasons. Increased deposition of tracers at the reattachment point is purely due to hydrodynamics; fluid flow towards the wall and low wall shear stress causes a large number of tracers to deposit. On the other hand, the second peak appears because of abnormal wall adhesive properties i.e. the wall biological response has altered. It is important to notice that even though the lesion site is "disadvantaged" because of being downstream of the reattachment point, it recruits same population of tracers. This stresses the potential importance of a realistic adhesion model since pure hydrodynamics would not be sufficient to predict wall deposition profile in real case abnormalities. As already mentioned, realistic probabilistic model for cell adhesion can be implemented based on Monte-Carlo acceptance-rejection methods and can be straightforwardly adapted to our approach.

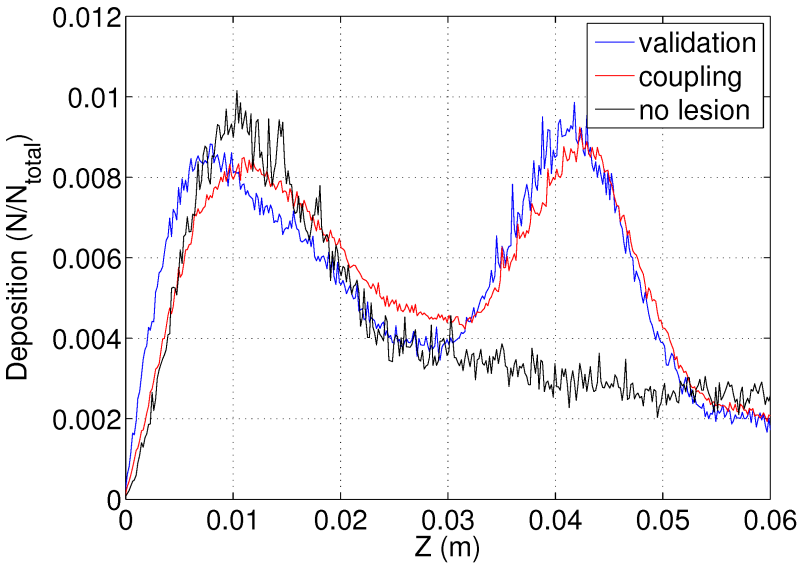


Figure 3.17: Comparison of deposition profiles in presence and absence of wall abnormalities - coupling and validation results match closely.

# 4 Kinetic adhesion modeling

It is well established that studying pathogenesis of arterial diseases, or any near-wall dynamics of blood cells for that matter, cannot be accurately carried out without considering chemical interactions among cells. Such chemical reactions manifest in form of several chemical bonds, which are essentially a stable attracting force between cells. Since these *adhesive forces* were, and still are, difficult to measure or quantify, many computational studies on cell dynamics settled for using simple models such as formulating a force-distance relationship.

Looking more closely into the dynamics of a pair of adhered cells, the adhesion could be the result of any number of bonds formed between pairs of receptor-ligand molecules on the surface of the cells. In addition to that, experimental studies suggest that formation of a single bond is a significant event in determining whether two cells adhere. Hence, cell adhesion should be viewed as a stochastic process (Hanzlik et al., 2008).

Reaction kinetics has been used extensively in biology to describe formation of bonds between receptor-ligand molecules (Bell et al., 1984, Evans and Ritchie, 1997, Zhu, 2000). Consequently, this concept is extended to study cell dynamics in the framework of larger simulations. The idea is to use reaction kinetics to relate binding affinity to the applied force acting on the cell (Tees and Goetz, 2003). There is considerable evidence to justify this choice. Particularly, underlying specific molecular interactions are short-ranged and the size of resulting bonds are typically an order of magnitude smaller than those of the adhering cells. Moreover, different adhesion molecules are involved at different stages of formation of a bond (Hammer and Apte, 1992). Thus, an overly simple adhesion criterion, e.g. based on cell-cell separation distance, does not capture the realistic receptor-ligand adhesion behavior.

In this chapter, development of kinetic cell adhesion models is reviewed and specific formulation in small systems, that fit the current work, are presented. The chapter is closed by studying result of cell adhesion is a stenosed sudden expansion model.

## 4.1 Modeling of kinetic cell adhesion

One of the first major studies to develop a modeling framework for cell adhesion and receptor-ligand bond formation is performed by Bell (Bell, 1978). Bell's model used chemical reaction kinetics to describe the relation between bond dissociation rates to the force applied on each bond. The use of reaction kinetics in modeling cell adhesion is motivated by the fact that the Brownian motion of molecules becomes significant in their interaction range (Zhu, 2000). Hence, the fate of pair of receptor-ligand molecules that are in close vicinity of each other cannot be determined solely based on their separation distance. Same applies to breakage of an existing bond.

Several future works were based on Bell (1978). Bell et al. (1984) expanded his work to take the competition between the formation of specific bonds and nonspecific repulsion due to electrostatic forces into account. Evans (Evans, 1985) developed a theoretical framework based on Bell's model to describe the membrane-membrane adhesion and separation behavior. Such a model would be used to compute adhesion forces between a biomembrane and a substrate. In a separate work, Dembo et al. (1988), Dembo (1994) expanded Evans (1985) by adding molecular bond kinetics to their tape-peeling theory to compute adhesion forces between the membranes. Furthermore, Hammer and Lauffenburger (1987) developed a dynamical model to predict the conditions under which cell-surface adhesion takes place in a shear flow. Their prediction were restricted to determining whether cell arrest happens after an initial collision. However, their model evolved into the *Adhesion Dynamics* method used in a number of studies to predict conditions for no adhesion, rolling adhesion, and firm adhesion (Hammer and Apte, 1992, Zhang et al., 2004, King et al., 2005).

### 4.1.1 Modeling approach

It was not until 1990 that probabilistic theory for kinetics was applied to cell adhesion (Zhu, 2000). Cozens-Roberts et al. (1990a) used a probabilistic description of receptor-ligand binding to describe a homogeneous population of pairs with different binding states. Similar to Hammer and Lauffenburger (1987), they assumed an exponential reverse kinetic rate and a constant forward rate. In contrast, Evans et al. (1991) proposed a power law for reverse kinetic rate. Hammer and Apte (1992) adopted a Monte Carlo (MC) approach to be able to easily combine the chemical kinetics with other macroscopic physical properties of the system.

An alternative to the MC approach (Hammer and Apte, 1992, Tees et al., 1993, Chen and Springer, 1999, Longest et al., 2004, Jadhav et al., 2005) is to obtain adhesion probabilities by solving the master equations (Zhu, 2000). One of the first

attempts in this direction was the work of Kaplanski et al. (1993) who obtained a numerical solution to the master equations for systems with less than ten bonds. Additionally, there has been a number of studies that obtained closed-form solutions of the master equations corresponding to different systems (Piper et al., 1998, Chesla et al., 1998, Long et al., 1999, Zhu, 2000).

### 4.1.2 Experimental work

Regardless of the method, all studies that use Bell's model need to confirm their findings based on experimental data.(Merkel et al., 1999, Li et al., 1999, Dustin et al., 1996, Pierres et al., 1995, Kaplanski et al., 1993). In the framework of atherosclerosis progression, Rouleau et al. (2010) studied adhesion of neutrophils to endothelial cells in an asymmetric stenosis geometry. Charoenphol et al. (2010) experimented on polymer particle adhesion to the inflamed endothelium. They studied the influence of particle size, presence of RBCs, and shear rate on particle adhesion. Hsiai et al. (2003) investigated monocyte-endothelium binding kinetics in an arterial bifurcation with oscillatory flow. An important finding of their study was establishing an association between the oscillatory flow and up-regulation of adhesion molecules that mediates monocyte-EC binding. Hinds et al. (2001) examined the effect of wall shear stress on U937 monocyte-like cells in an E-selectin-coated vertical model with stenosis and sudden expansion. Alon et al. (1997) investigated differences in rolling speed of leukocytes in L-selectin compared to E- and P-selectins by studying the dissociation of transient bonds for them.

An important finding of a number of these studies, that investigated properties of single bonds, (Florin et al., 1994, Alon et al., 1995, Piper et al., 1998, Chesla et al., 1998) was that a single bond, even when the rate of formation and breakage of bond is high, is a significant event in determining the fate of adhesion. Therefore, adhesion of two molecules is considered a stochastic phenomenon. Bell model parameters obtained from these studies could be used to create state diagrams regarding adhesion and rolling of leukocytes (Chang et al., 2000).

### 4.1.3 Parameter study

It should be noted that, in many cases, presence of convection in addition to diffusion makes prediction of kinetic rates more difficult (Zhu, 2000). This could specifically affect formation of the first bond, when convection brings interacting molecules closer (Chang and Hammer, 1999), and dissolution of the last, when convection moves them apart (Piper et al., 1998). As an example, Rinker et al.

(2001) investigated the effect of force, i.e. shear value, and contact time, i.e. inverse of shear rate, on monocyte endothelial adhesion. They obtained an enhanced rate of bond formation by increasing shear value at a fixed contact time. Experiments of Skilbeck et al. (2001, 2004) emphasized this point further that flow disturbances affects the adhesion of leukocytes. They performed experiments in a backward-facing step geometry to see how leukocyte binding reacts to disturbed flow and came to the conclusion that flow disturbance in regions with high WSS enhances leukocyte adhesion. Moreover, Zhu et al. (2008) identified two mechanisms that influence leukocyte adhesion in L-selectin-ligand interactions based on experimental data: (a) *transport-dependent acceleration of bond formation* and (b) *force-dependent deceleration of bond dissociation*.

Furthermore, as already stated, it has been shown by several groups that the adhesive behavior of cell could be influenced by a number of factors. To mention a few, concentration and proximity of rolling cells on rolling velocity was examined by King and Hammer (2001b). They also proposed a *hydrodynamic recruitment* mechanism in which cells from bulk are pulled toward the surface due to already-attached cells (King and Hammer, 2001a). As a result of their platelets adhesion modeling, Vasin et al. (2003) concluded that diffusion coefficient does not play a role in the adhesion of the platelets to the surface. The role of particle size on adhesion is studied by several groups (Worth Longest and Kleinstreuer, 2003, Jeong et al., 2013). The effects of disturbed flow on attachment of leukocytes to vessel walls were investigated by Skilbeck et al. (2001, 2004). Decuzzi and Ferrari (2008, 2006) studied adhesion of non-spherical nanoparticles to diseased vascular cells. Flow pulsatility and cell deformability have been reported to affect the adhesion (Dong et al., 1999, Khismatullin and Truskey, 2005, Khismatullin, 2009). Moreover, influence of receptor/ligand density, cell microvilli extension, and several other factors have been studied in a number of other studies (Moore et al., 1995, Norman et al., 1995, Shao et al., 1998, Park et al., 2002, Ramachandran et al., 2004, Chen et al., 2007, Sundd et al., 2011).

### 4.1.4 Simulation coupling

There has been several studies where the adhesion model is used in framework of a full simulation to investigate coupling of flow and adhesion parameters. Lei et al. (1996) used a convective-diffusion equation to study the transport of low density lipoproteins (LDLs) across the endothelium. Munn et al. (1996) investigated the role of RBCs on adhesion behavior of leukocytes. They found out the adhesion of WBCs could be affected by RBCs through (a) RBC forces on WBCs when near wall,

(b) changes in spatial distribution of WBCs in bulk, and (c) collision with RBCs. Sun et al. (2003), Sun and Munn (2005) came to a similar conclusion regarding the role of RBCs on leukocyte capture to the vessel wall. They used a two-dimensional lattice Boltzmann approach. Barber et al. (1998) studies U937 cell adhesion to human umbilical vein endothelial cells in a sudden expansion geometry featuring recirculating flow. Chapman and Cokelet (1998) studied the effect of Newtonian low-Reynolds flow passing over multiple adherent leukocytes in a cylindrical vessel with postcapillary size. Dong et al. (1999) used finite element to study the deformation and adhesion of leukocytes to endothelial cells.

David et al. (2001) studied deposition of platelets in stagnation point flow by controlling shear rate. Comparing results with experiments data from Affeld et al. (1995), they found that a WSS-dependent reaction rate at the wall gives closer agreement with the experiment results. Worth Longest and Kleinstreuer (2003) studied monocyte and platelet deposition in the tubular geometry from Hinds et al. (2001). They used a discrete particle model (DPM) approach with the fluid as continuum and spherical particles as the discrete phase. For cell adhesion, a first-order forward reaction rate was applied. They managed to get close local agreements with the experiment. However, due to the nature of their Euler–Lagrange scheme, they were limited to relatively small number of particles. In a related work, Longest et al. (2004) used the MC approach to qualify cells for adhesion in their study of monocyte transportation in a femoral anastomosis. Similar to Worth Longest and Kleinstreuer (2003), they used the Euler–Lagrange approach, but treated the plasma and RBCs as a non-Newtonian fluid.

Haun and Hammer (2008) performed both experiments and computational analysis studying the influence of molecule density and steady flow rate on adhesion of antibody-coated nanoparticles to intracellular adhesion molecule (ICAM-1) substrate. Lyczkowski et al. (2009) developed an Euler–Euler non-Newtonian multiphase approach to analyze adhesion of U937 monocyte-like human cells to an E-selectin-coated stenosis geometry (Hinds et al., 2001). They used first-order reactions to model attachment, rolling, and detachment of monocytes *in vitro*. Their coupled multiphase scheme is able to predict non-uniform spatial distribution of flowing monocytes, however, results were not particularly close to those of the experiment (Hinds et al., 2001). Kim and Rhee (2011) investigated effect of time-varying shear rate on the adhesion of antibody-coated nonparticles. Furthermore, they studied the influence of kinetic constant, as a function of ligand/receptor density, particle size, and flow shear force, on bond formation.

Using same methods to study cancer matastasis, Yan et al. (2012) investigated the effect of WSS and its gradient on adhesion of tumor cells to curved microvessels

experimentally and computationally. For the numerical part, they used a lattice Boltzmann approach and took bond association and dissociation into account. Jeong et al. (2013) studied binding of nanoparticles arterial wall with the attachment rate as a function of shear rate and particle size. In their study, particles showed a positive correlation with the shear rate when smaller than $600nm$ and a negative correlation when larger than $800nm$. Hossain et al. (2014) investigated deposition of spherical nanoparticles of three different sizes in a patient-specific arterial tree coated with ICAM-1, VCAM-1 and E-selectin. They used a time-dependent inlet velocity and the advection-diffusion equation to model the transport of particle within blood. They concluded that particle adhesion is the result of complex interplay between local WSS, receptor density, and particle distribution. Gholami et al. (2015) used SPH to simulate transport and adhesion of U937 monocyte-like cells in the E-selectin-coated stenosis geometry of Hinds et al. (2001). They overcame the limitation of the Lagrangian scheme in terms of the number of particle using their previous work (Gholami et al., 2014) that coupled bulk and near-wall quantities. Initially, they calibrated association rate parameters from Piper et al. (1998) using one set of the experimental data. Next they showed that deposition results could be reproduced with good agreement for both steady and pulsatile flows.

## 4.2 Adhesion kinetics in small systems

It was mentioned in the previous section that several probabilistic and deterministic kinetic models have been used in studying cell adhesion. However, it has been observed in several experiments that the nature of bond formation between a pair of receptor-ligand is stochastic (Cozens-Roberts et al., 1990b, Piper et al., 1998, Chesla et al., 1998). This is especially important when considering small systems. One way to model such *random* behavior is to solve the master equations for adhesion probabilities.

In this section, these equations are presented for small systems (McQuarrie, 1963), and solved to get a closed-form. To stays close to the scope of this work, let's consider adhesion of a cell to a surface, as shown in Fig. 4.1. As the cell approaches the surface, receptors and ligands that cover the surface and exterior of cell have the possibility to form bonds. However, even under strict controlling of the conditions, the number of bonds that form and break follows a stochastic pattern. As a result, the adhesion of the cell to the surface as a whole, is moderated by a random number of bonds. The idea is to solve the master equations to obtain $p_n$, probability of having $n$ bonds between the cell and surface.

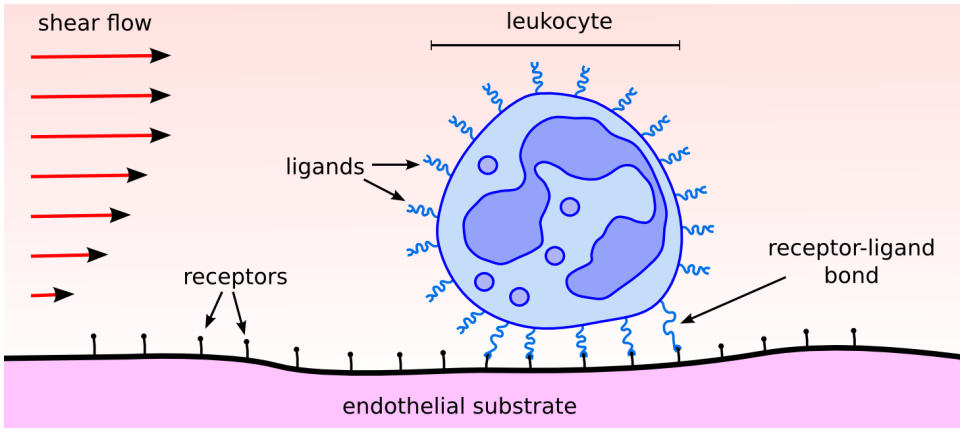


Figure 4.1: Adhesion of a leukocyte to endothelium - In presence of blood flow, a shear force is exerted on the cell. As the leukocyte approaches the endothelium, the probability of formation of a bond between ligands and receptors on their surfaces increase. It has been shown that formation of even one bond is a significant event in determining whether the cell adheres to the surface. Existing bonds could brake off due to the external force acting on them from the flow.

Considering a one-step reversible system kinetic system where $N_b$ bonds are produced from $N_r$ receptors and $N_l$ ligands, the rate of change of probability $p_n$ is defined as (Chesla et al., 1998):

$$\begin{aligned}\frac{dp_n}{dt} &= (n+1)^{N_b}\frac{k_r^{(n+1)}}{A_c^{N_b-1}}p_{n+1} \\ &- \left[\left(A_c m_r - \frac{N_r}{N_b}n\right)^{N_r}\left(A_c m_l - \frac{N_l}{N_b}n\right)^{N_l}\frac{k_f^{(n+1)}}{A_c^{N_r+N_l-1}} + n^{N_b}\frac{k_r^{(n)}}{A_c^{N_b-1}}\right]p_n \\ &+ \left[A_c m_r - \frac{N_r}{N_b}(n-1)\right]^{N_r}\left[A_c m_l - \frac{N_l}{N_b}(n-1)\right]^{N_l}\frac{k_f^{(n)}}{A_c^{N_r+N_l-1}}p_{n-1},\end{aligned} \tag{4.1}$$

where $n$ is the number of bonds between the cell and surface, $A_c$ contact area, $m_r$ surface density of receptors, and $m_l$ surface density of ligands. $k_f$ and $k_r$ are forward and reverse reaction rate constants, respectively. Moreover, the superscript $n$ implies that these reaction rate constants depend on the force acting on the bond. This equation assumes the formation of breakage of bonds to be a Markovian process, i.e. it has no memory of the past. It is worth mentioning that, in some

studies, the breakage rate is reported to depend on force history (Marshall et al., 2005). Additionally, Eq. 4.1 assumes uniform probability of bond formation for all receptor-ligand pairs in the contact area, and uniform breakage probability for all existing bonds (Piper et al., 1998).

As can be seen, the rate of change in $p_n$ is divided in three terms. The first and last terms are probability influxes, hence positive. They both account for formation of n bonds through either breakage of one bond in a system with $n+1$ bonds, i.e. first term, or addition of one bond to a system with $n-1$ bonds, i.e. third term. The second term represents two scenarios: breakage or formation of a bond in a system with $n$ bonds. In either case, the system ends up with more or fewer bonds, hence the second terms has a negative sign.

To continue, Eq. 4.1 is written for a more specific case where a bond is formed from strictly one pair of receptor-ligand, i.e. $N_r = N_l = N_b = 1$:

$$\begin{aligned}\frac{dp_n}{dt} &= (n+1)\, k_r^{(n+1)} p_{n+1} \\ &- \left[ (A_c m_r - n)\,(A_c m_l - n)\,\frac{k_f^{(n+1)}}{A_c} + n k_r^{(n)} \right] p_n \\ &+ \left[A_c m_r - (n-1)\right]\left[A_c m_l - (n-1)\right]\frac{k_f^{(n)}}{A_c} p_{n-1}\end{aligned} \tag{4.2}$$

Piper (1997) solved this equation in steady state using mathematical induction to get a closed-form solution for the probability of having exactly $n$ bonds, $p_n$. By normalizing the sum of all $p_n$ to unity, they obtained a closed-form for the probability of having no bonds:

$$p_0(f) = \left[1 + \sum_{n=1}^{A_c m_{\min}} \frac{1}{A_c^n} \binom{A_c m_r}{n} \binom{A_c m_l}{n} \prod_{m=1}^{n} m K_a\left(\frac{f}{m}\right)\right]^{-1}, \tag{4.3}$$

where $m_{\min} = \min(m_r, m_l)$. Appearance of $m_{\min}$ is justified by the fact that the number of bonds is limited by the minimum of receptor and ligand population.

The term $K_a(f/m)$ in Eq. 4.3 is called the binding affinity and is defined as the ratio of forward to reverse rate constants, i.e. $K_a(f/m) \equiv k_f^{(m)}/k_r^{(m)}$. Piper et al. (1998) proposed the following form:

$$K_a\left(\frac{f}{m}\right) = K_a^0 \left[1 + c\left(\frac{af}{mk_BT}\right)^d\right]^{-1} exp\left[-\left(\frac{af}{mk_BT}\right)^b\right], \tag{4.4}$$

where $K_a^0$ is the ratio of association to dissociation rates in absence of force, $k_B$ the Boltzmann constant, and $T$ temperature. The model is characterized by four parameters: $a$, $b$, $c$, and $d$. $k_BT/a$ serves as a reference scale for force term $f$. Parameters $b$ and $c$ are used to determine a power law (Evans et al., 1991) or exponential law (Bell, 1978), and parameter $d$ is associated with flexibility of formed bonds. Even though the exponential law has proven sufficient in several cases, Piper et al. (1998) showed advantages of the power law over the exponential law.

For the case presented in this work, it is assumed that the number available receptors and ligands in the contact area exceeds the population of bonds by far. Such an assumption allows to simplify the steady-state solution, Eq. 4.3, by neglecting $n$ compared to $A_cm_r$ and $A_cm_l$:

$$p_0\left(f\right) = \left[1 + \sum_{n=1}^{A_cm_{\min}} \frac{1}{n!} \prod_{m=1}^{n} m_r m_l A_c K_a \left(\frac{f}{m}\right)\right]^{-1}. \tag{4.5}$$

Hence, the probability of the cell having at least one bond is $P_a = 1 - p_0$. Replacing in Eq. 4.5 gives:

$$P_a = 1 - \left[1 + \sum_{n=1}^{\infty} \frac{1}{n!} \prod_{m=1}^{n} m_r m_l A_c K_a \left(\frac{f}{m}\right)\right]^{-1}. \tag{4.6}$$

As mentioned, $A_cm_{\min}$ is much larger than the number of bonds. Therefore, the upper limit of the sum in Eq. 4.6 is replaced by infinity. This allows to characterize the adhesion behavior of the cells with five parameters: $a$, $b$, $c$, $d$, and $K^0$ $(= m_r m_l A_c K_a^0)$. For the simulations used in this work, a Monte Carlo acceptance-rejection method is used to reproduce this distribution.

## 4.3 Cell adhesion in stenosed sudden expansion model

In order to understand how cell adhesion, represented by Eq. 4.6, is introduced to our multiscale coupling method, Fig. 4.2 should be considered. The bulk (gray area) contains only SPH particles. SPH dynamics and bulk tracer concentration are modeled as described in chapters 2 and 3. The near-wall region (blue area) is where tracers are created. In our application its width is at least one order of magnitude smaller than characteristic length of the bulk. Stokes forces, wall corrections, and Brownian motion dominate tracer dynamics in this region. Numerical modeling of

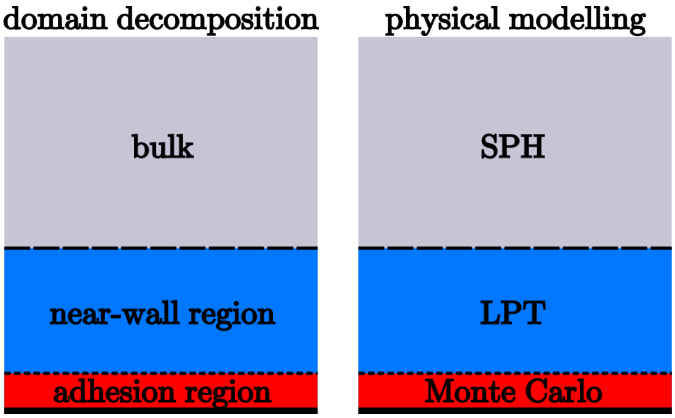


Figure 4.2: Composition of physical and computational domain.

tracers is carried out by specific LPT, Eqs. 3.10 to 3.13. The adhesion region (red area) is where the tracers are so close to the surface that adhesion forces start to become significant, i.e. cell-cell bond formation is likely. For tracers in this region, probability of adhesion is evaluated using Eq. 4.6.

### 4.3.1 Adhesion probability and dislodging force

Capabilities of the adhesion model are demonstrated in the following where the effect of inhomogeneous force on adhesion probability is shown for a simple *steady forcing*. This gives an overview on the effect of the adhesion model parameters on the overall deposition profiles and provides an initial guess for the optimal selection of the tracers' binding avidities. The dislodging force is calculated along the pathline of a fluid element moving in the vicinity of wall in the 3D stenosed sudden expansion geometry (see Fig. 4.3) using wall shear stress and wall distance (Fig. 4.4). This geometry is used in this work to simulate near-wall cell dynamics and validate the results against those of Hinds et al. (2001).

In the entrance region the force is approximately constant. As the geometry contracts ($x = -3$) the dislodging force increases, due to flow acceleration, and maximizes at the end of the contraction ($x = -1$). Through the throat of the stenosis ($-1 < x < 0$), which is of constant diameter, there is a small decrease in the force. At $x = -1$ the geometry expands, leading to a small jump in the force that then immediately drops to approximately zero; flow separates from the wall. Downstream of the expansion the force rises slightly due to retrograde flow. Finally the force drops to almost zero at the location of flow attachment ($x \sim 1.5$). In

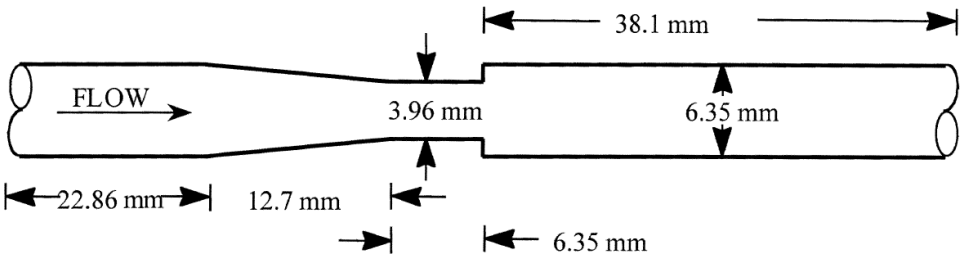


Figure 4.3: Three-dimensional stenosed sudden expansion geometry. The figure is taken from Hinds et al. (2001).

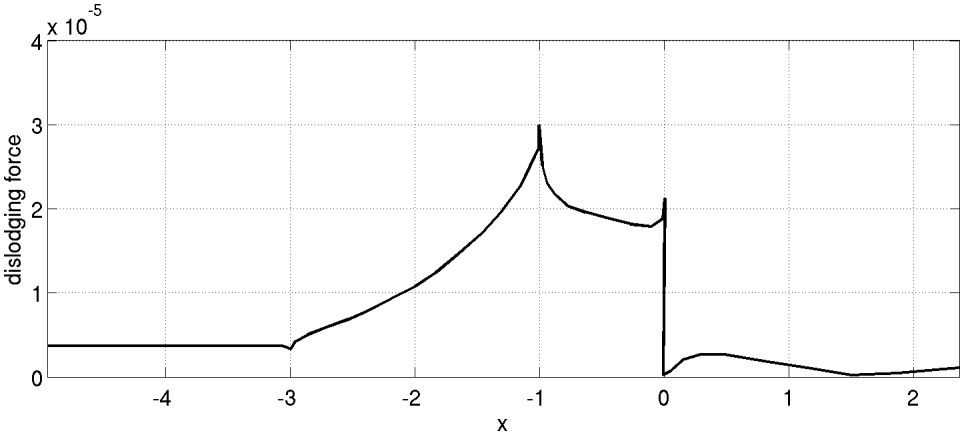


Figure 4.4: Dislodging force along a pathline in the vicinity of wall obtained from flow simulation in the 3D stenosed sudden expansion geometry (Hinds et al., 2001)

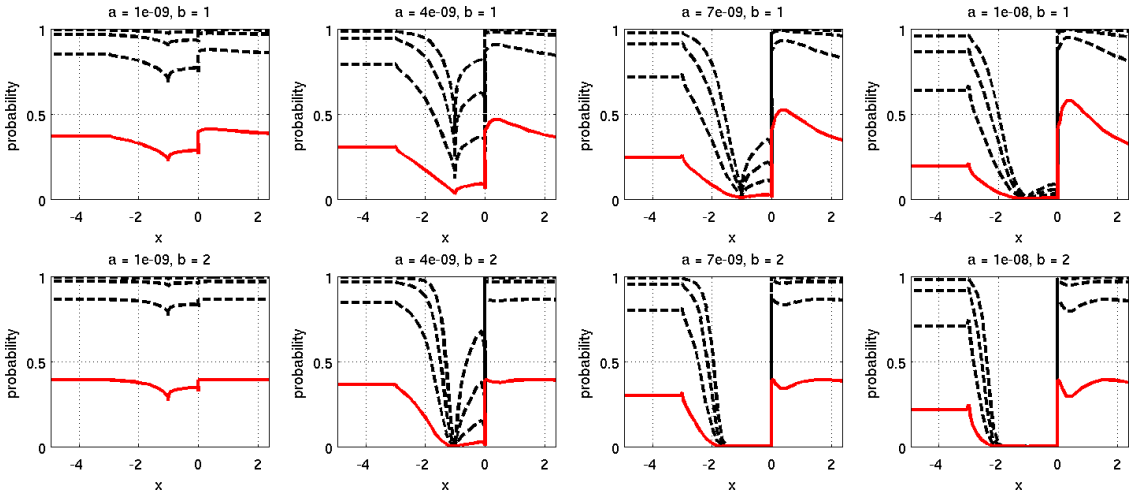


Figure 4.5: Investigation of adhesion probability along the wall for the exponential law - Adhesion probability for a particle moving along the wall-adjacent pathline is shown in the vertical axis. $K^0$ ranges from 0.5 (the solid red line) to 5.0.

Figs. 4.5 and 4.6 adhesion probability is plotted against streamwise coordinate for several values of parameters $a$ and $b$ for an exponential and power law, respectively. Furthermore, probabilities are evaluated for different values of $K^0 (= m_r m_l A_c K_a^0)$ in each subplot to fully cover the parameter space. Values of $a$ are chosen according to the range of values for force in Fig. 4.4. Parameter $b$ is set to both 1, as in Bell (1978), and 2, as in Dembo (1994). By setting $c$ to 1 the power law is switched on. For simplicity, $d$ is chosen similar to $b$.

As expected, probabilities decrease by increasing force in both models. As $a$ increases, i.e. range of force decreases, the probability drops for higher forces. $b$ and $d$ both exaggerate the sensitivity to force. However, the power law offers more control over the outcome of the model; compared to exponential law, it shows higher sensitivity to force with similar parameters. In any case, upon utilizing this adhesion model, both laws could be employed easily.

The detachment probability can be prescribed in a similar manner to allow for adherent WBCs to detach from the endothelium. Model parameters can be calibrated by fitting deposition profiles with available experimental results. For example, a number of experimental setups ara available in the literature. Some examples include: a steady gravity-driven flow of U937 cells in an E-selectin coated-geometry (Hinds et al., 2001); neutrophil adhesion in an asymmetric stenosis model

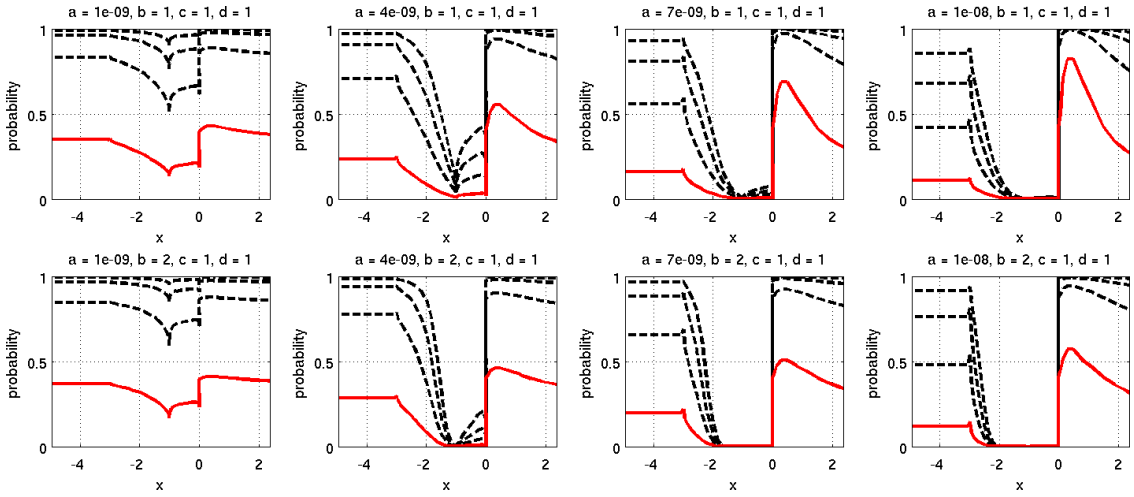


Figure 4.6: Investigation of adhesion probability along the wall for the power law - Adhesion probability for a particle moving along the wall-adjacent pathline is shown in the vertical axis. $K^0$ ranges from 0.5 (the solid red line) to 5.0.

(Rouleau et al., 2010); adhesion of WBCs to vessel wall in 3D backward facing step models has also been under focus (Skilbeck et al., 2004, Chiu et al., 2003); and leukocyte adhesion in shear flow(Simon and Goldsmith, 2002).

As demonstrated, the stochastic biological adhesion model offers enough degrees of freedom to reproduce realistic adhesion dynamics in a variety of problems introduced in this section. For validation of the final model, we take advantage of parameter estimation modeling to march the corresponding large parameter space.

### 4.3.2 Flow conditions

In this section simulation of the cell-dynamics in the in vitro setting presented in Hinds et al. (2001) is discussed. This study provides sufficient data related to residence time, adhesion and relative surface concentration of U937 cells flowing through a stenosed axisymmetric sudden expansion (see details of geometry in Hinds et al. (2001)). This geometry leads to spatially varying wall shear stress at the surface and allows for the investigation of the relationship between haemodynamic parameters and cell deposition. In the experimental model the surface of the model was coated with E-selectin, in order to facilitate binding of U937 cells at higher flowrates. E-selectin was chosen to replicate the mechanochemical environment in

Table 4.1: Flow and tracer parameters.

| Parameter | Value |
|---|---|
| Density | 1 $(g/cm^3)$ |
| Viscosity | 0.008 $(g/cm \cdot s)$ |
| Timestep size | $\approx$ 1.024e-4 $(s)$ |

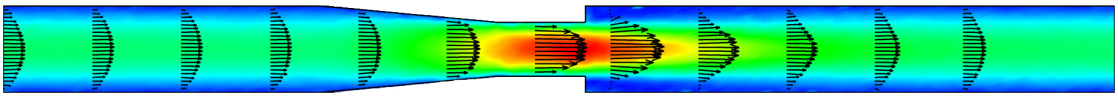

Figure 4.7: Cross section velocity field at Re = 100 in the three-dimensional stenosed axisymmetric sudden expansion geometry used in Hinds et al. (2001) to analyse U937 cell dynamics and deposition

regions prone to atherosclerosis.

The full three dimensional surface geometry has been created and imported as an input file into our SPH code. From this point several flow scenarios are simulated in order to estimate adhesion parameters and validate results against experiment data of Hinds et al. (2001). In particular, we model two cases under steady conditions (Reynolds numbers 100 and 140). Flow parameters for these cases are summarized in Table 4.1.

Hydrodynamic simulations are run along with the multiscale coupling SPH method to extract both the flow field and cell deposition. Fig. 4.7 shows a sketch of the simulated geometry at Re = 100 together with a section indicating the local magnitude of the fluid particle velocity in the expansion region. Convergence of the local velocity profile as well as near-wall concentration profile was obtained.

Fig. 4.8 shows the composition of the physical / computational domain in presence of SPH and tracer particles. As our multiscale SPH-tracer method prescribes, tracers (black dots) exist in the vicinity of walls only. Note that due to a higher ratio in 3D between the entire volume occupied by the flow device and the small near-wall surface layer, an increased speed-up of the novel multiscale SPH code can be achieved compared to the values previously reported for the 2D BSF geometry in Gholami et al. (2014).

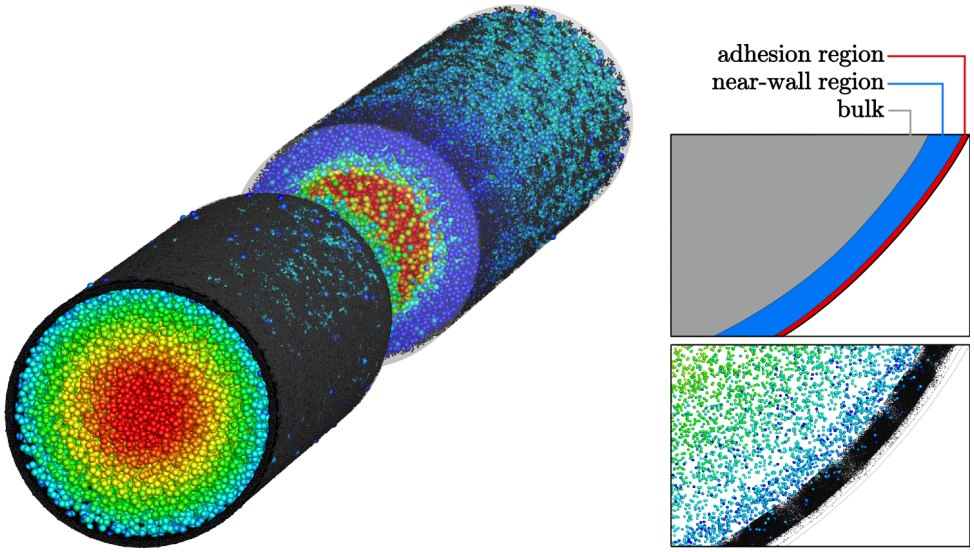


Figure 4.8: Demonstration of the tracer-particle coupling method - SPH particles are depicted as spheres colored with velocity magnitudes. Tracers are shown with black dots. It is clear that tracers are introduced close to walls. The three computational regions can be clearly distinguished.

### 4.3.3 Wall adhesion profiles

In this section, wall adhesion profiles delivered by our multiscale coupling method are presented and discussed. First, deposition profiles are obtained without using the stochastic adhesion model. WBC deposition criterion in this set of simulations is defined solely based on wall normal distance. After that, parameters of the stochastic adhesion model are estimated and new deposition profiles are obtained using that model. Differences betweens solutions and improvements resulted from using the adhesion model will be discussed.

For the first simulation, we assumed constant homogeneous probability of deposition for a tracer located within a minimum distance from the wall. This distance is chosen to be one tracer diameter from the wall. However, since we work with discrete tracers in the near-wall region, the deposition criterion can be easily adapted according to specific requirements; for example, a deposition probability can be prescribed for tracers within the deposition range and Monte-Carlo acceptance-rejection methods can be used. A local elevation in deposition probability, for example, has been imposed in Gholami et al. (2014) to model plaque growth

It should be stressed that, at this stage, we obtain information about the local

wall deposition profiles for cells interacting only hydrodynamically with the walls. This is because cell-wall interactions have been validated in our code for lubrication, lift and drag terms. Utilizing this approach, the adhesion profiles shown in Figs. 4.9 and 4.10 are obtained. After development of flow, tracers start to adhere to walls. In the accelerating section they are pushed towards the surface, which enhances wall adhesion significantly. In the stenosed section, tracers are directed away from walls, thus adhesion rates experience a drop. However, with redevelopment of flow, normal adhesion continues. After the sudden expansion, some of the tracers, over time, get trapped in the recirculation region and start attaching to wall, which causes a peak in adhesion profile.

Adhesion results are presented in a more quantitative way by circumferential averaging the deposition data, see Fig. 4.9. As demonstrated in Gholami et al. (2014), these results are hydrodynamically (in terms of SPH particle discretization) and statistically (in terms of tracer count) converged. Moreover, we showed that our method is able to extract deposition profiles with higher accuracy and much smaller fluctuations in comparison to other methods, e.g. full domain LPT in Longest et al. (2004).

It should be noted that even though adhesion profile obtained from our method is consistent with hydrodynamical aspects of the problem, e.g. wall shear stress, it does not agree with findings of the experiment. As an example, in the tapered section, coupling results show enhancement of adhesion due to tracers being pushed towards walls. However, in the experiment, due to high WSS, attachment of monocytes to the walls is decreased. This highlights the important conclusion that simulation of haemodynamics alone is not sufficient for such a complex problem, thus wall adhesion dynamics of blood particles must be taken into account. Full reproduction of the *in vitro* results demands introduction of the stochastic biological adhesion model which requires a modification of the probabilistic deposition strategy used in Gholami et al. (2014).

The stochastic adhesion model is characterized by the five parameters of Eq. (4.4), $a$, $b$, $c$, $d$, and $K^0 (= m_r m_l A_c K_a^0)$. Adhesion data presented in Fig. 4.9 is used to estimate these parameters. We started the estimation process by adapting $a$ according to the range of forces exerted on tracers in the adhesion region. Secondly, for the resulting range of $a$, $K^0$ and $b$ were optimized. Therefore, the dimensions of the optimization process is reduced. A semi-exhaustive search is then carried out on the parameter space for the $\mathrm{Re} = 100$ case to find a matching solution.

The resulting adhesion model (Table 4.2) was capable of closely reproducing the experimental results for $\mathrm{Re} = 100$ (see Fig. 4.11a). From this result, it is clear how important a finely-tuned adhesion model is for accurate reproduction of in-vitro

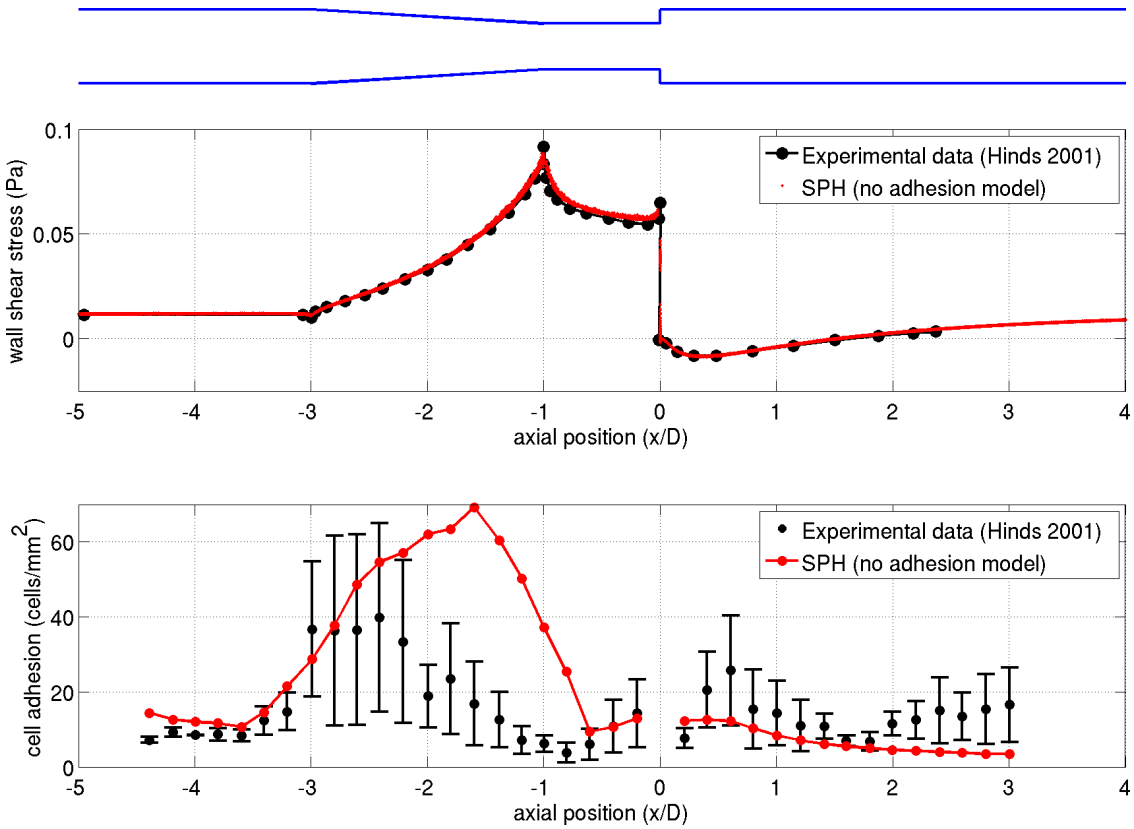


Figure 4.9: Comparison of simulation data with experiment at Re = 100. Top: taper geometry outline. Middle: comparison of wall shear stress (WSS) between our simulation of results of Hinds et al. (2001). Bottom: comparison of cell adhesion data.

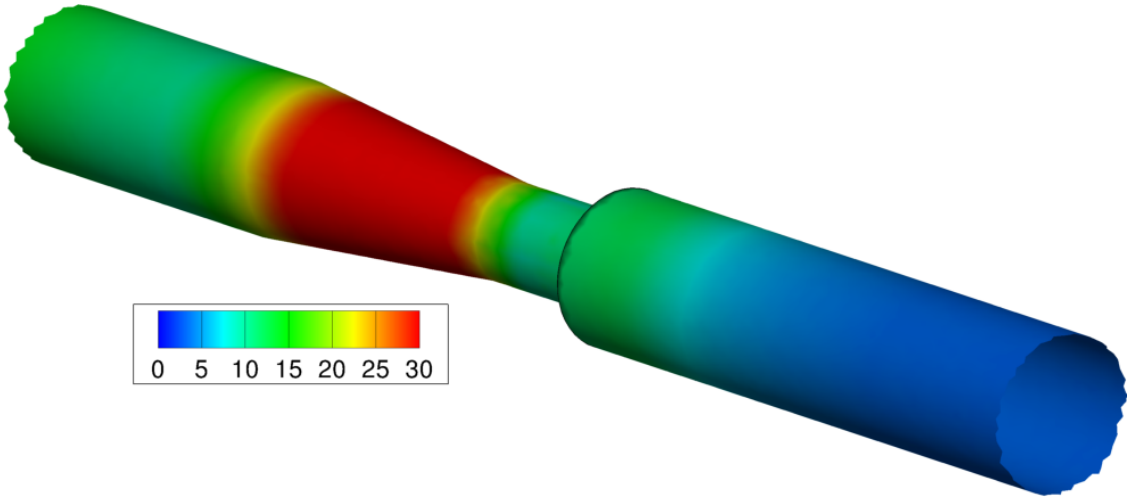


Figure 4.10: Contours of pure hydrodynamics cell adhesion on walls of 3D taper geometry.

Table 4.2: Parameters of the adhesion model based on Eq. (4.4).

| Adhesion parameter | Value |
|---|---|
| $a$ | 3.2224e-09 $(cm)$ |
| $b$ | 10 |
| $c$ | 0 |
| $d$ | 1 |
| $K^0$ | 5.0 |

adhesion(compare Fig. 4.11a with Fig. 4.9). The rate of adhesion in the taper region demonstrates a very close fit to the experiment. Consequently, now a larger number of cells enter the sudden expansion region which has led to an accurate prediction of adhesion peak in this region.

Fig. 4.11b presents a detailed comparison of simulation and experiment results for Re = 140, where adhesion parameters come directly from the previous Re = 100 case, i.e. with no fine-tuning. The results are in very close agreement, which demonstrates the accuracy and flexibility of our proposed method. A similar analysis of the interplay between flow velocity and adhesion criterion could be made. However, in this case the combination of effects results in a smaller peaks with less margin. Three-dimensional deposition contours (see Fig. 4.11 bottom) confirm that

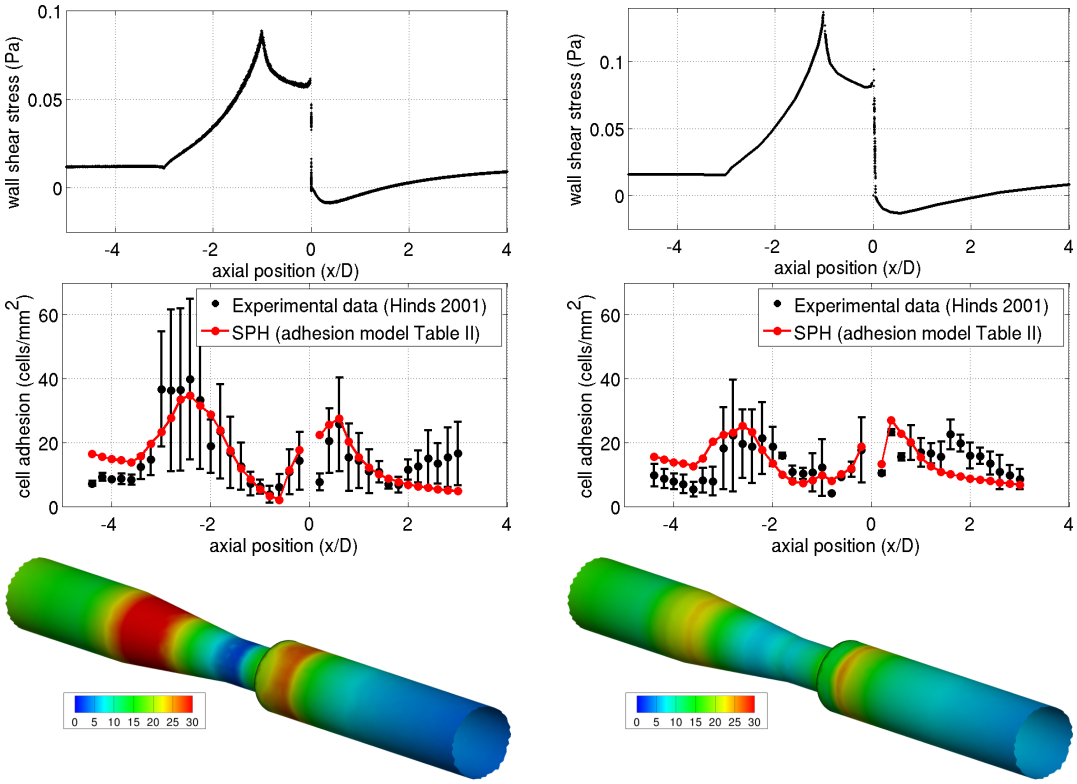


(a) Re = 100 (b) Re = 140

Figure 4.11: Comparison of cell adhesion data between simulation and the experimental data of Hinds et al. (2001) at different Reynolds numbers - wall shear stress (top) is aligned with cell adhesion (middle) to emphasize how non-uniform adhesion probabilities affect deposition behavior. At the bottom, contours of cell adhesion on walls are presented.

for the higher Reynolds number, flow velocity starts to dominate and cause a more or less flat profile compared to the case with lower Reynolds number.

Before continuing, the significance of these results should be emphasized. As pointed out earlier, there are several factors that make it extremely difficult to produce *accurate* results in a problem like this. A number of features are incorporated in our model that allows us to simulate accurate near-wall dynamics. Furthermore, we have managed to maintain the accuracy while keeping the size of the problem small. Lyczkowski et al. (2009) simulated the same problem using a multiphase CFD model coupled with an adhesion model based on receptor-ligand binding. They used ANSYS Fluent to simulate the blood as a non-Newtonian fluid and employed extremely small mesh size (20 $\mu m$) close to walls which is the monocyte diameter used in their simulations. Even though they managed to qualitatively demonstrate the significance of a well-developed adhesion model on near-wall monocyte dynamics, the accuracy of their results, Figs. 7 and 8 in Lyczkowski et al. (2009), is not comparable to ours in this article.

For the results presented in this chapter, near-wall tracer counts ranging from 15,000 to 75,000 were used. Considering the size of the near-wall region and only a uniform distribution of tracers over the total volume of the stenosed sudden expansion geometry, these numbers would map to a lower limit approximation of 170,000 to 850,000 tracers in the whole domain matching the cell density of $5 \times 10^5$ cells/ml used in Hinds et al. (2001) very closely. In reality, non-uniform distribution of blood-borne particles yields much larger total cell counts. Comparing these cell count estimations to similar works that use Lagrangian model, e.g. Worth Longest and Kleinstreuer (2003) with 40,000 and Kim et al. (2006) with 12,000, reveals the computational gain of our multiscale model. Additionally, due to a higher ratio in 3D between the entire volume occupied by the flow and the small near-wall surface layer, a greater amount of computational work is saved compared to the 2D case. Thus, an increased speed-up of the novel multiscale SPH code can be achieved with respect to the values previously reported for the BSF geometry (presented in Gholami et al. (2014)).

We will come back to this simulation in the next chapter where identical adhesion parameters will be applied to a transient flow.

# 5 Inflow/outflow boundary conditions

Human vasculature features tremendous size and complexity. Exploring these aspects of our vascular system has led to a better understanding of the underlying mechanisms and uncovered many of its mysteries. These findings have been translated into physical and mathematical models to make simulation of human hemodynamics possible. Nevertheless, it has been established that our current technology is far from sufficient to model this vast system of arteries, capillaries, and veins as a whole (Grinberg et al., 2009). To that end, restricting the computational domain to only regions of interest and employing proper inlet/outlet boundary conditions to account for up-/downstream effects is a must.

## 5.1 Inflow/outflow treatment of arterial flow

Obtaining accurate quantification of parameters in the flow of blood is very vital in understanding the overall behavior of our circulatory system. In case of any cardiovascular disease, such a knowledge is the first step in deciding the course of treatment or identifying the underlying pathogenesis (Taylor and Draney, 2004). Of course, this concern is not limited to hemodynamics, but could be extended to almost any flow simulation in human body.

One of the issues that appears to be common among many of biomedical engineering flow simulations, particularly in cardiovascular networks and bronchial trees, is unknown or inaccurate flow measures at sections of interest. Such lack of knowledge has often led to incorrect and unrealistic assumptions at boundaries, which in turn affects simulation results dramatically (Soni and Thompson, 2012, Nowak et al., 2003, Zhang et al., 2005).

Flow conditions could be particularly sensitive to the choice of boundary conditions in flow partitioning and particle deposition in bifurcations. There are several examples in the literature where the impact of boundary treatment is studied in such scenarios, e.g. see (Yin et al., 2010, Wall and Rabczuk, 2008, Spilker et al.,

2007, Luo et al., 2007, Formaggia et al., 2006, Sherwin et al., 2003). It is important to note that findings of these studies, i.e. suitability of certain boundary treatment methods, differ based on the application and flow specifications. Therefore, there is no *one* solution.

In the context of arterial networks, Grinberg and Karniadakis (2008) divided main outflow boundary approaches in four groups. *Constant pressure* approach is a reasonable choice for steady and single-outlet unsteady simulations (see Soni and Thompson (2012), Comerford et al. (2010), Walters and Luke (2010), Gemci et al. (2008) However, applying same pressure for different outlets results in incorrect splitting of flow since the resistance of downstream vasculature, i.e. outside the domain of interest, is neglected. *Resistance* boundaries assume pressure and flow rate are linearly dependent. In contract to the *constant pressure* approach, this method could be applied to unsteady cases with multiple outlets, however, it is more expensive (see Formaggia et al. (2006), Sherwin et al. (2003)). The third approach is *Windkessel model* boundaries that are available for steady and unsteady simulations. Similar to *Resistance* approach, this method could become unstable due to close correlation between flow rate fluctuations and pressure oscillations (Grinberg and Karniadakis, 2008, Ismail et al., 2013b). Finally, the *impedance* boundary approach is based on analytically solving linearized flow equations in a one-dimensional network of arteries (Olufsen, 1999, Grinberg et al., 2009) This approach has been reported to be the most suitable to take downstream wave reflection into account (Vignon-Clementel et al., 2006).

Besides these approaches, other methods have been developed and used to address the outflow boundary condition problem. In a number of works, velocity or flow rate have been applied at the outlet (see Werder et al. (2005), Nowak et al. (2003), Calay et al. (2002). Coupling with model of reduced dimension has been used a numerous studies Ismail et al. (2013a), Urquiza et al. (2006), Formaggia et al. (2007), Malossi et al. (2011), Blanco et al. (2007). As an example, due to unknown pressure conditions at outlet, Vignon-Clementel et al. (2006) used coupling of boundary properties to a downstream reduced, i.e. lumped or 1D, model to simulate blood flow in complex geometries. To circumvent impractically large computational costs, the reduced-order model could be used to provide boundary conditions for a full three-dimensional representation of the domain of interest. Finally, some work has been dedicated to stabilization of existing boundary treatment methods. For example, Moghadam et al. (2011) studied different approaches, namely adding stabilization term, using normal velocities, and reconstructing velocity profile, to control backflow divergence at outlets. The latter approach has been addressed in other literature as well (Veneziani and Vergara, 2005, Formaggia et al., 2002).

Regarding inlet conditions, prescribing flow rate or velocity has been the main approach (Shahriari, 2011, Freitas and Schröder, 2008, Zhang and Kleinstreuer, 2002). In both steady and transient simulations, it is common to use fully-developed velocity profiles, i.e. parabolic in steady or Womersley's profiles in time-varying simulations, as inlet condition (Sazonov et al., 2011, Soni and Thompson, 2012). It should be noted that Womersley's velocity profile should in general be treated as an approximation Grinberg et al. (2009). However, Moyle et al. (2006) made experiments to find out whether assuming fully developed axial flow at entrance is valid for modeling realistic carotid bifurcations. They concluded that, accurate reconstruction of geometry with a sufficient entrance length prevails over measuring 3D inlet velocity profile. Nonetheless, there are many other cases where this conclusion does not hold, e.g. see Peterson and Plesniak (2006), Yang et al. (2006). Alternatively, Neumann boundaries have been used as inlet conditions, see Xia et al. (2010), Kim et al. (2009b). Instabilities associated with this type if inlet condition are mentioned in Kim et al. (2009a).

In cases where more complex flow features, such as three-dimensional effects, bifurcation, secondary flow profiles, etc. play a crucial role in the overall behavior of the system, models similar to the aforementioned 1D-lumped coupled approaches are unable to provide sufficient insight Vignon-Clementel et al. (2006). Consequently, in the current work, a full three-dimensional modeling of the blood flow is carried out. Considering this work focuses on major arteries, this choice is absolutely necessary and computationally feasible.

Availability and implementation of these boundary condition should still be addressed. In the context of particle methods, Lykov et al. (2015) mentioned two issues regarding the open boundary treatment. Firstly, outlet flow conditions is mainly unknown, despite known inlet conditions in single phase flow (see also (Lei et al., 2011)). Secondly, in more realistic scenarios such as mixture of blood cells, even the inlet conditions are unknown or unfeasibly expensive to impose. As a result, due to lack of knowledge and/or better models, periodic conditions have been applied in several scenarios (Fedosov et al., 2012, 2011, Hossain et al., 2014), while non-periodic conditions are less often utilized. For a more elaborate list of such simulations, see Lykov et al. (2015)

### 5.1.1 SPH implementations

Regarding the state of the art in SPH, development of inflow and outflow boundary conditions has received more attention only recently, but this area is yet to become mature. Due to the meshfree nature of SPH, similar difficulties in defining open

boundary treatment, as those mentioned previously, prevail. Shahriari et al. (2012) associated challenges in developing proper inflow and outflow boundary condition in SPH with two issues: insufficient kernel support for near-boundary particles, and approximate representation of boundaries due to moving Lagrangian particles.

These issues have been addressed differently in the community. Khorasanizade and Sousa (2016) summarized existing approaches into three main groups. Firstly, application of the method of characteristics to model open boundaries. As an example, Lastiwka et al. (2009) proposed a method based on this approach to model non-reflecting boundaries. The second approach is introducing a buffer layer of particles at the boundaries of the domain. Variations of this approach are used often, e.g. in Flekkøy et al. (2005), Lykov et al. (2015), Gholami et al. (2015). The third main approach is based on using semi-analytical methods to determine boundary values Kulasegaram et al. (2004), Ferrand et al. (2013). Additionally, application of other approaches, e.g. variable forces at boundaries, have been reported in the literature Vignon-Clementel et al. (2006), Lei et al. (2011).

To conclude this section, relevant literature regarding application and development of inflow/outflow boundary conditions in SPH is reviewed in the last decade. Sinnott et al. (2006) simulated the pulsatile flow in a carotid artery bifurcation using SPH. They imposed time-varying velocity profiles at the inlet to account for the pulsatility of the flow. For outlet boundaries, they used a constant pressure, 10kPa at both internal and external carotid arteries. However, they did not discussed simulation stability and validity of their results. Lastiwka et al. (2009) proposed a SPH characteristic-based non-reflecting boundary condition that allows imposition of analytical inlet and outlet conditions at boundaries through definition of ghost particles. Their development was, however, based on a uniform single-phase velocity condition on straight boundaries. Hosseini and Feng (2011) proposed a pressure-correction scheme to calculate accurate pressure close to open and wall boundaries. Their approach showed good result for a number of standard cases. However, admittedly, demonstration for more complex cases was missing.

In a related work, Lei et al. (2011) developed a time-dependent boundary treatment in the context of Dissipative Particle Dynamics (DPD) for no-slip walls and fully-developed outflow boundaries. They used a force-adaptive approach and showed that their method performs well when velocity and pressure are in-phase. It is also worth mentioned the review work by Sazonov et al. (2011) where a complete modeling pipeline for simulation of hemodynamics in arterial networks is reviewed. Particularly, they outlined a detailed process to generate inlet and outlet flow conditions in patient-specific geometries. Their approach is based on calculating Womersley's profiles from known maximal velocity and flow rate at inlets and

outlets.

Shahriari et al. (2012) used the buffer particle approach of model pulsatile flow in two-dimensional left heart ventricle. They reported their outflow BC to be *not strictly non-reflecting* but adequate for their 2D heart cavity simulation. According to Vignon-Clementel et al. (2006), as wave reflection naturally occurs in cardiovascular networks, no wave reflection boundaries are not necessarily a viable option. Federico et al. (2012) used ghost particles to model inflow and outflow in a 2D open channel. Their results matched analytical solutions; however, similar to many of the aforementioned studies, their simulations featured only one inlet and one outlet.

Extending Ferrand et al. (2013), a semi-implicit open BC was proposed by Kassiotis et al. (2013). They demonstrated suitability of their approach for complex geometries. Similarly, Leroy et al. (2016) extended the unified semi-analytical boundary condition technique to incompressible SPH (ISPH). They only showed results for 2D dam break and circular 3D pipe flow.

Using ghost buffers for open boundaries seems to be explored more extensively compared to other methods Hou et al. (2014), Domínguez et al.. Lykov et al. (2015) developed a *general framework* inflow/outflow boundary treatment for multiphase particle flow. They assumed a fully-developed profile at inlet and applied adaptive forces at outlets to maintain mass flow. Particularly, they used a generation region for ghost particles at inlets that interacts with the interior only in the forward direction. Moreover, they showed results of 3D arterial flow with multiples inlets and outlets. More recently, Khorasanizade and Sousa (2016) extended previous work (Khorasanizade et al., 2012) and introduced inflow/outflow BCs for ISPH using buffer regions. They successfully showed stability and accuracy of their approach in modeling flow around square cube. Hirschler et al. (2016) also developed an open boundary condition for ISPH that uses *mirror particles* for both open velocity and open pressure boundaries. They demonstrated several cases such as the standard flow around cylinder, flow acceleration due to pressure pulsation, and flow in a porous network with multiple outlets.

## 5.2 Boundary treatment with ghost particles

It was mentioned in the previous section that handling open boundaries using ghost particles is quite common in SPH. In many applications implementing such boundary conditions was avoided by using periodic boundaries. Particular advantages associated with periodic BCs, e.g. no extra particle treatment at boundaries and

full kernel support at boundaries, justified their application in many studies. For transient simulations, this approach was extended to use time-dependent body force to match the time-dependent mass flow. However, when realistic arterial geometries are considered, periodic treatment is not an option anymore. To that end, the ghost particle approach extends the computational domain with a few layers of ghost SPH particles to allow an more elaborate handling of the boundaries. This is shown in a schematic of the carotid artery bifurcation, see Fig. 5.1, where inlet and two outlets are extended.

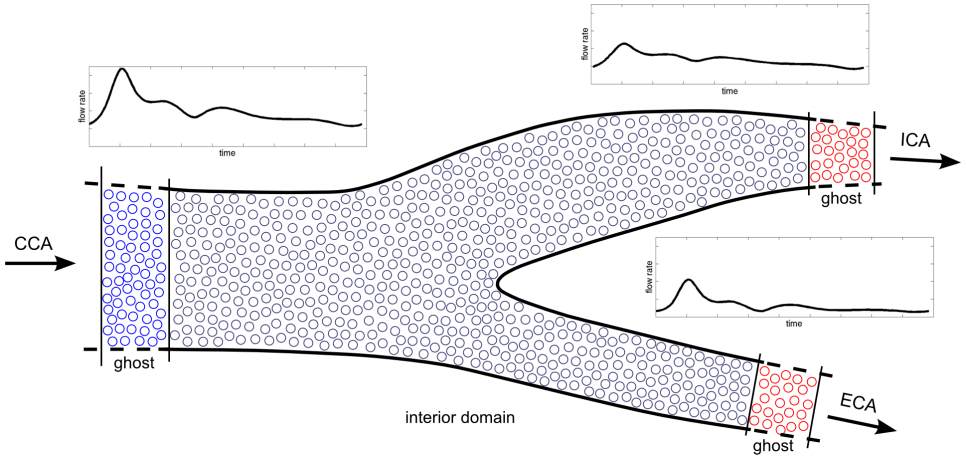


Figure 5.1: Ghost particles at inlet (blue) and outlet (red). Interior particles are colored in gray. Average flow rate waveforms are shown above each ghost boundary.

Generally, two mechanisms are required to implement such boundary conditions. The first mechanism is responsible for imposing a condition in a boundary. It was mentioned in the previous section that, in the context of cardiovascular flows, a *known* condition could significantly differ based on the specifics of the application under study. As the challenges in that regard are already discussed, it is assumed here that information regarding physics of boundary, e.g. velocity profile, pressure values, etc. are available. Consequently, the first mechanism prescribes known values for particles in the buffer zone. Furthermore, it defines the kind of interactions between ghost and real particles to impose the desired boundary condition in a stable manner. A second mechanism must be employed to insert and remove particles at inlets and outlets. Depending on the overall design of the boundary treatment, this step could preserve particles' mass on average or strictly at any moment. The difference between the ghost particle methods proposed in literature is mainly how

they implement these mechanisms.

Lastiwka et al. (2009) developed a non-reflecting boundary condition for SPH. They introduced an inlet buffer larger than the support radius of the kernel function. According to the method of characteristics for the subsonic flow, particle at inlet need to values prescribed. Therefore, they suggest to set velocity explicitly and extrapolate pressure (density) from only the interior particles. To account for inaccuracies due to insufficient kernel for such extrapolation, they use reproducing kernel particle method (Liu et al., 1995). When an inlet ghost particles enters the real domain, a copy of it is created by shifting it position upstream of the inlet buffer. At outlet, they suggest prescribing pressure or density and extrapolating velocity. Outflow ghost particles are integrate according to SPH formulation until the are removed.

Lei et al. (2011) proposed a DPD outflow condition by prescribing mass flow at outlet, assuming velocity and pressure are in-phase in a fully developed flow. To impose this condition, they introduced *adaptive* forces to maintain mass flow and eliminate velocity differences in regions adjacent to the outlet. Particle leaving the buffer region are then simply removed from the simulation. At inlet new DPD particles, with prescribed velocities, are inserted randomly. They mentioned random insertions position did not cause any large disturbances in their simulations. Otherwise each new insertion must be carried out in a way to minimize the local thermal disturbances.

Shahriari et al. (2012) used a regular grid of particles at inlet to simplify the insertion problem. They imposed mass flow by inserting a new particles only after one has left the domain through outlet. The new particle has a prescribed velocity, but its pressure and density is computed by SPH. The downside is that the result scheme is not non-reflecting. Additionally, they only showcased their work for geometries with one inlet and one outlet with similar shapes. In a similar work by by Federico et al. (2012), interaction between particles is one-way, i.e. only from ghost to real particles. At inlet, they impose both velocity and pressure on a regular grid of particles. Once a particle enter the outflow buffer, all its physical properties with the exception of position are frozen.

Lykov et al. (2015) developed a general particle open boundary method for cardiovascular networks. Assuming a fully developed flow at inlet, they introduced two regions at the beginning and two at the end of the inlet buffer region to form a periodic box (see Fig. 2 in (Lykov et al., 2015)). Consequently, used a particle shifting scheme to impose the fully developed assumption. Similar to the previous works, interaction between ghost and real particles is one-way. Their approach for outflow boundary is similar to that of Lei et al. (2011). However, instead of adaptive

force, they reflect back outflow ghost particle into the domain to maintain a density. The probability of reflection is computed from target and current densities. If a particle is not reflected, they are removed from the simulation.

More recently, Khorasanizade and Sousa (2016) developed inflow/outflow boundary condition for incompressible SPH. At inlet, velocities are prescribed and pressure in taken from interior SPH particles normal to the boundary. When an inlet ghost particle enters the domain, a new inlet ghost particle is created by shifting the position to the beginning of the inlet buffer. At the outlet, particle velocities are frozen once a particle enters the outlet buffer; however, their pressure is still updated in the same way inlet ghost particles are treated. Finally, to enforce mass flow conservation, they added a time-dependent driving force based on the ratio of mass flow at inlet and outlet. Consequently, they avoid explicit manipulation of particle velocities which could cause instabilities.

## 5.3 Influence of pulsatility on cell adhesion

As mentioned in the previous chapter, we come back to the stenosed sudden expansion model to study a time-dependent flow. For the transient case, appropriate boundary conditions must be applied to the SPH particles for desirable results. Wall boundary conditions are already well-established in SPH simulations and several modifications are proposed to handle special cases. In this work, we use a standard approach to model wall no-slip boundary condition by introducing frozen particles at the boundaries. For the rest of this section, inflow and outflow boundary conditions and the corresponding SPH handling will be discussed.

### 5.3.1 Time-dependent boundary conditions in sudden expansion model

The three-dimensional stenosed sudden expansion geometry, presented in Fig. 4.3, allows using a periodic boundary condition at the inlet and outlet for steady flow cases. Therefore, when a particle leaves the domain, it is re-inserted from the other end. The flow is driven by an external force that is regulated to enforce the desired inlet Reynolds number. The advantage of this approach is that it requires no extra treatment of SPH particles other than the normal calculation of density and pressure. Specifically, domain periodicity results in uniform density for SPH particles at the inlet and outlet, where incomplete kernel support typically requires additional work to maintain accuracy. This approach was used for results presented in chapter 4.

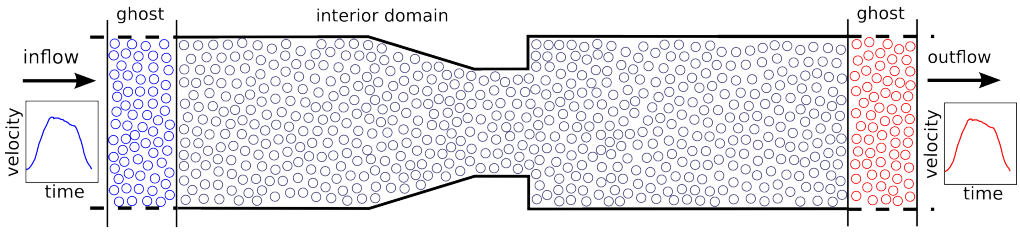


Figure 5.2: Introduction of inflow (blue) and outflow (red) ghost particles. SPH particles in the interior domain are colored in grey. Width of the ghost buffers is in the range of SPH cutoff distance. Average flow rate waveforms are shown above each ghost boundary. Data is extracted from the work of Lee et al. (2008).

Modeling unsteady flow is, however, not as straightforward. One approach would be to use a time-dependent body force to simulate pulsatility of the flow. The drawback of such an approach is that it cannot be extended to realistic cardiovascular conditions. In such environments, the velocity profile over the inlet cross-section is assumed to be fully developed flow i.e. Womersley flow. This is motivated by a number of previous studies that have deemed this to influence the downstream haemodynamics to a limited degree providing sufficient upstream length (Moyle et al., 2006). As this is the case for the pulsatile flow in Hinds et al. (2001), we developed suitable boundary conditions that can impose velocity profile at boundaries.

In the context of SPH, such inflow/outflow boundaries are typically handled by introduction of buffer zones (ghost particles) at the inlet and outlet, respectively (see Fig. 5.2). Each buffer zone extends the physical domain with a few layers of SPH particles. This approach was outlined in the previous section.

For the inlet and outlet boundaries we utilize pulsatile waveform data presented in literature and scale them to out geometry. This process is described in detail in a review paper (Sazonov et al., 2011). Following this approach, velocity time profiles can be independently computed and applied to each boundary. We start by calculating complex velocity amplitudes by applying a FFT to the velocity waveform data given in Hinds et al. (2001). Accurate resolution of the waveform requires a sufficient number of harmonic components which could differ from case to case. Next, all harmonic components are calculated by solving a boundary value problem on a mesh at the boundary plane. The velocity profile at each time is represented by a Fourier series and can now be computed using the normalized harmonic components and the complex amplitudes.

An example of the final result is shown in Fig. 5.3. A sinusoidal wave over half

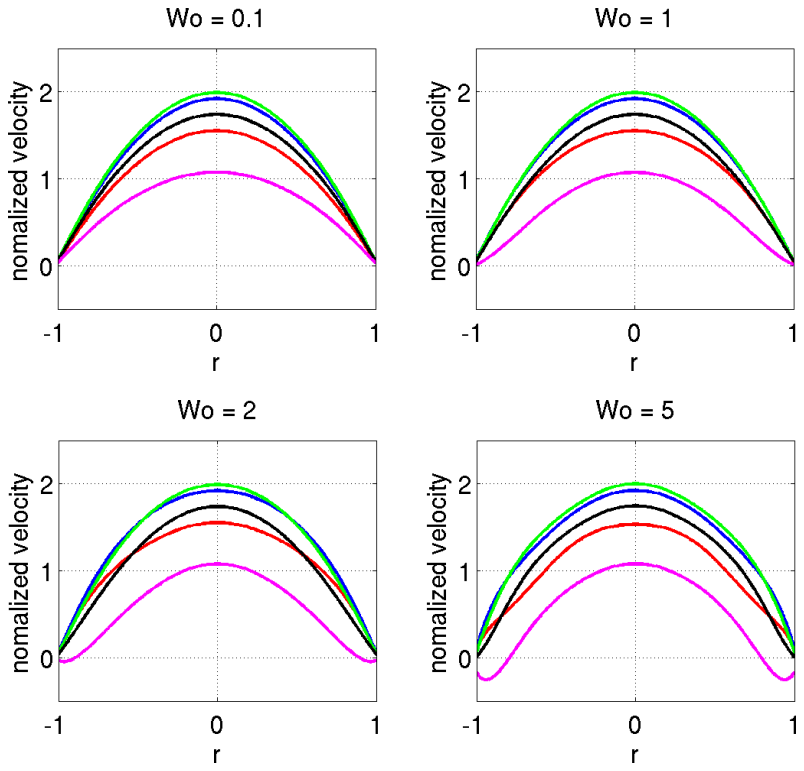


Figure 5.3: Velocity profile evolution at a circular boundary for a sinusoidal waveform is calculated using Womersley profiles. The impact of the Womersley number on the instantaneous velocity profile is shown.

of its period is chosen as an example waveform. Velocity profiles over a circular boundary are calculated at identical instances of time for different Womersley numbers. It is clear that as the Womersley number increases, the lag between the pressure gradient and the mean flow causes the profile to deviate from the Poiseuille profile. This information is already enough for imposing the SPH pulsatile boundary condition as described earlier.

Although the correct enforcement of inflow/outflow boundary conditions does not pose any problem in practice, we should mention a difficulty which could arise in the implementation mentioned above. Due to the intrinsically compressible nature of SPH, traveling pressure waves generated within the domain (or physically realized at the outflow) should be able to escape from the open boundaries without producing artificial back scattering. This represents an open area of research within the particle-methods community. Characteristic-based non-reflecting boundary conditions for

mesh-based methods have been recently implemented into the SPH framework (Lastiwka et al., 2009) and mesoscopic particle methods (Delgado-Buscalioni and Dejoan, 2008) showing good results. Modifications of our implementation of the inflow/outflow boundary conditions to have a fully non-reflecting boundary condition will follow these guidelines.

### 5.3.2 Cell adhesion pattern in sudden expansion model

It is now well established that in cardiovasular blood flow problems (as presented here) a purely hydrodynamic analysis is not sufficient to accurately predict the behavior of the system. Hence, a complete model must take into account the interplay between cell transport and local wall interactions. As the results in chapter 4 suggest, the outcome could alter significantly by small changes in biomechanics of the system. In order to explore this further, a case with pulsatile flow, using identical adhesion parameters presented in Table 4.2, is simulated. The pulsatile velocity waveform (Fig. 5.4a) is extracted from data presented in Hinds et al. (2001). The flow is characterized by a Womersley number of about 3, which is typical of some larger arteries such as Femoral and Carotid arteries. Similarly to the experiment, the simulation is run for 20 cycles, and results are compared in Fig. 5.4b.

Firstly, Fig. 5.4a shows that the inflow/outflow boundary condition is performing well. At the beginning of the simulation, a fraction of the pulse time is spent on bringing SPH particles to the non-zero initial velocity over the entire domain. After the initialization period, the solution follows the prescribed pulsatile profile very closely. In Fig. 5.4b cell adhesion at the walls is compared after 20 cycles. Wall profiles agree very well for most of the domain and stay within the bounds of the experimental data for the region of interest. Pulsatility has caused the adhesion profile to be noticeably flatter that the $\mathrm{Re} = 100$ case. Considering that the average Reynolds number in the pulsatile case is 107, this seeming discrepancy emphasizes the pulsatile flow could be a crucial factor when studying cell adhesion.

Fig. 5.5 shows the three-dimensional evolution of cell adhesion over the course of the simulation. After 5 cycles, the maximum adhesion occurs in the taper region and is only around 7 cells/mm$^2$. However, after 10 cycles the profiles are better established and even some adhesion has taken place after the sudden expansion. This trend goes on with the simulation, but it is clear that the adhesion front after the sudden expansion advances very slowly, to the extent that by the end of 20 cycles it is just around 2 cells/mm$^2$.

Previously a number of groups have considered pulsatile flow through the present geometry (Worth Longest and Kleinstreuer, 2003, Kim et al., 2006). In these studies

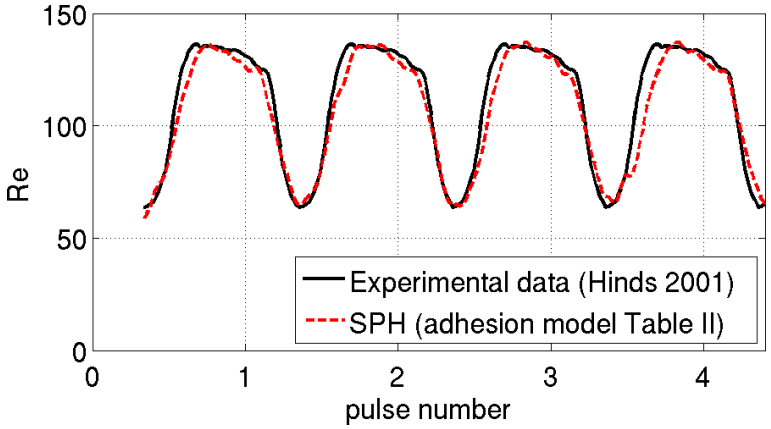


(a) pulsatile flow waveform

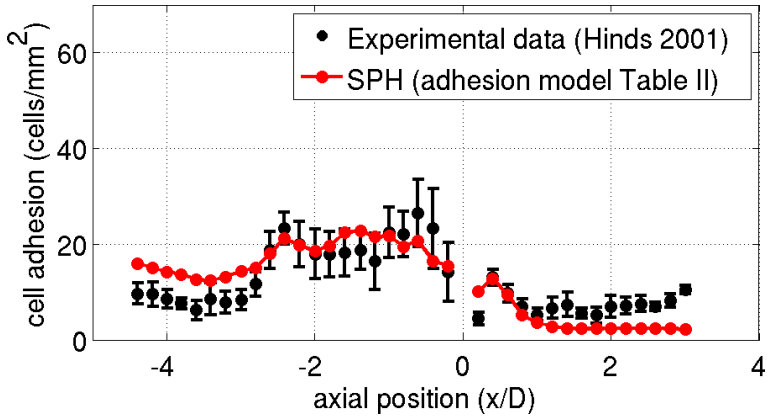


(b) cell adhesion

Figure 5.4: Comparison of cell adhesion data between simulation and the experimental data of Hinds et al. (2001) for pulsatile flow

an Eulerian-Lagrangian approach to was used to calculate secondary parameters; near wall residence time (NWRT) and near-wall deposition probability (NWDP), respectively. They are defined to incorporate factors that contribute to the likelihood of particle deposition. After solving the flow field, these parameters are calculated along the particle trajectories. Even though the actual deposition profiles, e.g. Fig. 9 in Worth Longest and Kleinstreuer (2003), do not fit the experiment, these secondary parameters are tuned to fit the cell adhesion profile, Fig. 5.4b. However, it should be pointed out that we can accurately reproduce a physical quantity, deposition rate, without changing the adhesion model, i.e. once we estimate the adhesion parameters for the $\mathrm{Re} = 100$ case, we do not adapt it any more. Hence, Figs. 4.11b and 5.4b prove the ability of our model to capture the physiological nature of the problem. On the contrary, same conclusion could not be made for those articles. Instead of only tuning the adhesion model, they tune their results to fit them to the experiment. Such an approach lacks a clear description of the haemodynamics versus adhesion.

## 5.4 Towards patient-specific hemodynamics

Numerical modeling of arterial blood flow presents itself as a powerful and insightful research tool allowing for the identification of numerous hemodynamic parameters, that are impossible or complicated to measure *in vivo*. Additionally it allows for the progression of *in vitro* studies by identifying pertinent parameters that require *in vivo* testing thus allowing the disease initiation to be understood in more detail.

To that end, modeling the complex environment in arteries requires realistic artery geometries. These geometries are obtained via segmentation of standard medical images, such as Computed Tomography (CT) or Magnetic Resonance Imaging (MRI) data. In the next step, using segmentation software, the arterial lumen can be identified and a realistic 3D reconstruction of the geometry can be produced. An example result of utilizing such a procedure is indicated in Fig. 5.6, where a carotid artery bifurcation surface is shown. Data is segmented from standard CT data. Finally this geometry can be prepared for simulation by cutting outlets perpendicular to the flow direction. This process is explained in detail in Sazonov et al. (2011).

Surface data can be consequently used to model the transport of leukocytes using the particle method explained earlier. The code is written in a generic way to accommodate modeling of arbitrary geometry, similar to those in Fig. 5.6. Additionally, it allows specifying inlet and outlet conditions by extending the

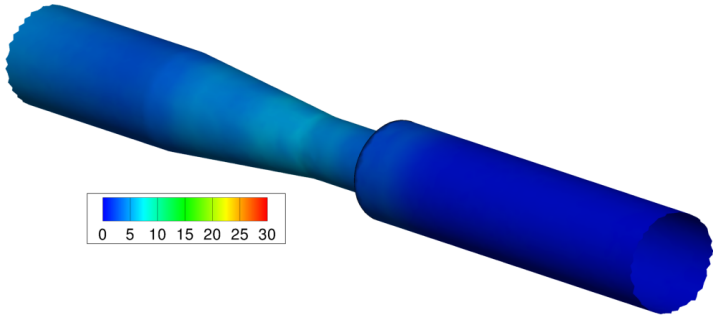


(a) pulse 5

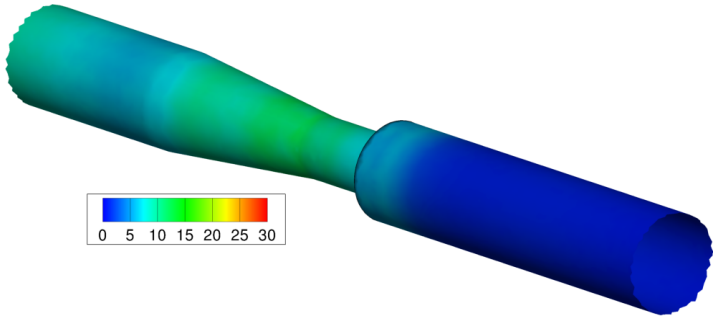


(b) pulse 10

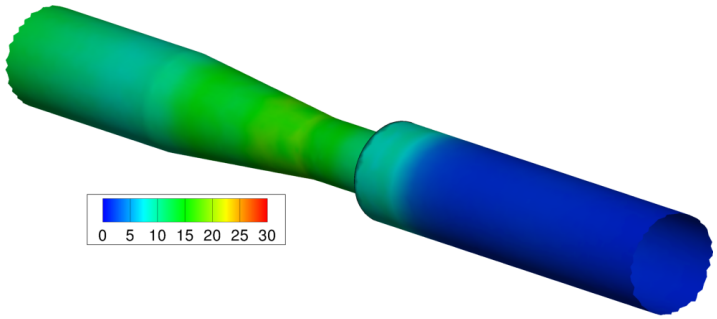


(c) pulse 15

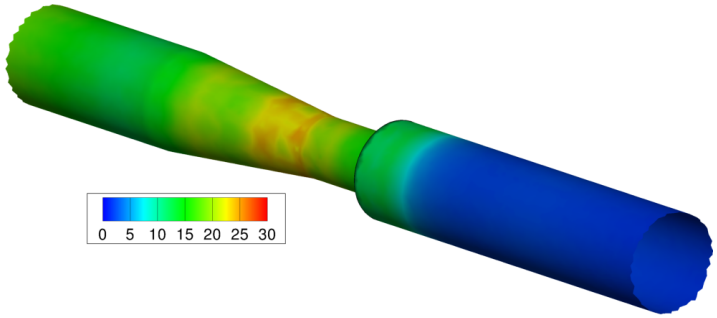


(d) pulse 20

Figure 5.5: Evolution of cell adhesion contours on walls of 3D taper geometry over time

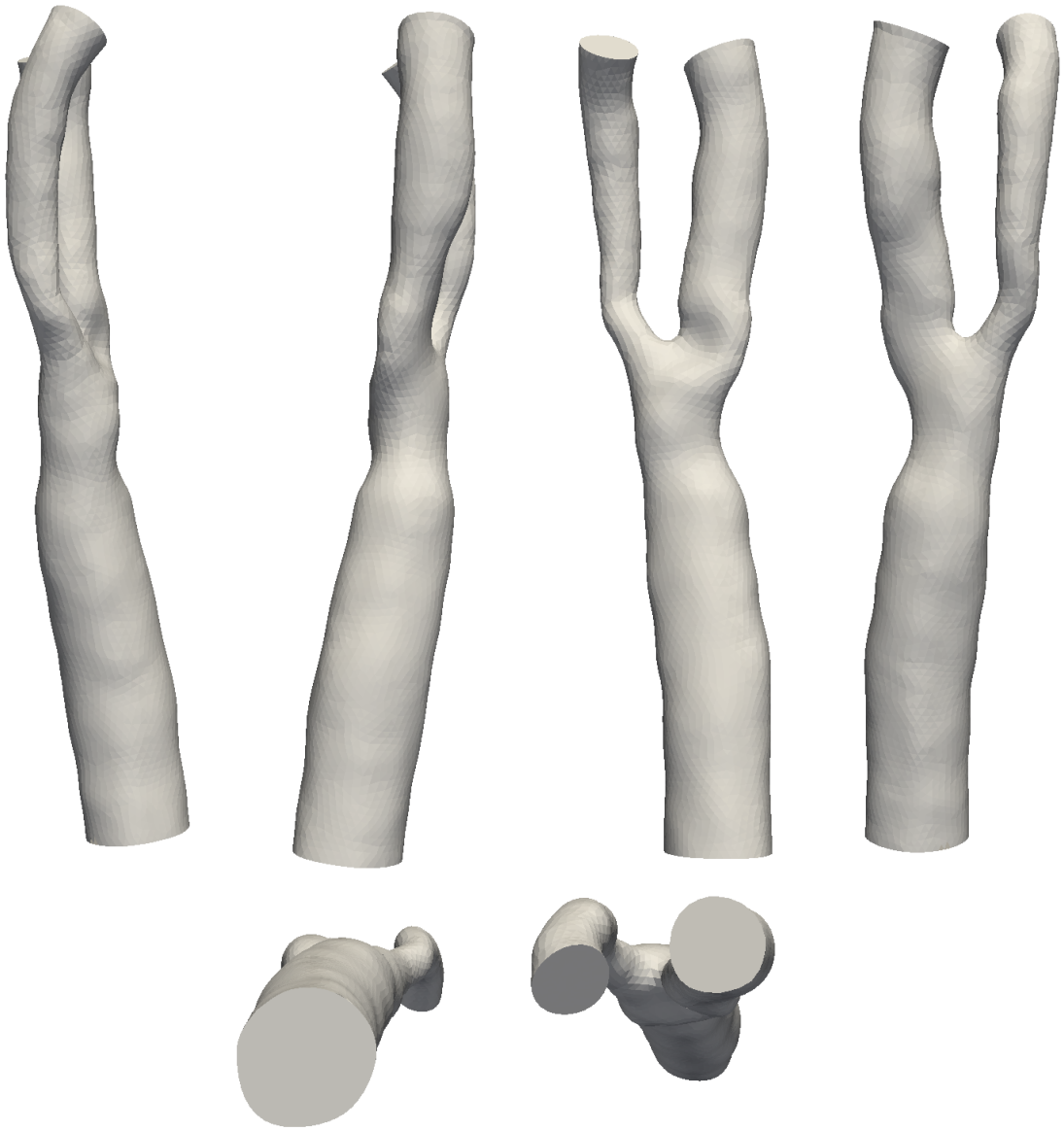

Figure 5.6: Three-dimensional surface data of a carotid artery bifurcation shown in six coordinate directions. Common carotid artery, internal carotid artery, and external carotid artery are visible. Surface data is provided by Sazonov and others, see Sazonov and Nithiarasu (2012), Sazonov et al. (2017), Yeo et al. (2011).

computational domain beyond the supplied geometry. Looking at the larger picture, this brings the developed framework to a realistic setting, i.e. a model of leukocyte transport coupled to a cell adhesion model of the leukocyte-receptor interaction kinetics at realistic endothelial surface.

In addition to patient-specific arterial geometries, delivering a truly realistic model requires realistic inflow and outflow boundary conditions. In particular, the vasculature represents a very large closed network and the modeling of only a small part of the system can yield incorrect solutions, hence the effect of the downstream vessels should be taken into account. Therefore, the ability to model multiple inlet/outlet boundaries with physiological and time-varying pressure and velocity conditions is crucial.

It was shown in the contest of SPH, such boundaries can be realized through the use of inflow/outflow buffers filled with ghost particles outside the domain that are created and removed as required. These particles interact with interior fluid particles like normal particles. Flow initialization with SPH for a patient-specific arterial geometry is shown is Fig. 5.7. Particularly, it is clear how inlet buffer particles are initialized on a regular grid to enable imposition of inlet velocities. Similarly, outlet buffers particles are interior particles that leave the domain. Their position is now determined by the velocity condition imposed on them.

Difficulties in modeling these boundaries are already discussed. In particular, a robust implementation of pulsatile flow in a geometry with multiple inlets and/or outlets proved challenging. Due to the intrinsically compressible nature of SPH, traveling pressure waves generated within the domain (or physically realized at the outflow) that do not escape from the open boundaries produce artificial back scattering. Proper implementation of such permeable non-reflecting boundary conditions would be the next step in this project.

In completing a truly realistic patient-specific model, one additional remark should be made. A relevant extension of the model would be to include the motion of the arterial wall coupled with dynamics of blood flow. Complex rigid/deformable boundary conditions are easily implemented in SPH. In blood flow *in vivo*, the effects of arterial wall movements are expected to significantly impact the local hemodynamic environment in the vicinity of the arterial wall. Hence this change in dynamics will inherently change the binding properties of leukocytes. It is therefore necessary consider the problem of fluid-structure interaction (FSI). Conventionally, structures are mostly simulated in a Lagrangian framework whereas the Eulerian formulation is preferred for the fluid flow. SPH has emerged as an alternative approach and has been considered to simulate the problem of elastic plate deformation (Antoci et al., 2007) and pulsatile flow through flexible walls (Farahani et al., 2009). The

Figure 5.7: Patient-specific modeling of blood flow using SPH. On left, tessellated three-dimensional surface of the CAB is shown. Surface data can be used to simulation flow in arbitrary geometries. On right, initialized SPH domain to model flow in CAB is shown. Inlet and outlet particle buffers extend the computational domain beyond those of the geometry.

solid material in both cases was modeled as a linear elastic solid. The advantage of using SPH in these situations is that it permits to easily follows fluid-solid interface without the need to perform remeshing or repeated interpolations. Moreover, it allows using the same numerical framework to simulate both solid and fluid phases, therefore eliminating the need for developing coupling schemes between two methods. This is realized by introducing two kind of particles (solid boundary particles and fluid particles) whose properties evolve according to the same SPH equations but with distinct closure relations for the stress tensor. The enforcement of the continuity of the normal component of the velocity and normal stress requires the computation of the position of the interface and normal direction which can be done in a straightforward way by considering neighboring SPH solid particles (Antoci et al., 2007) or, more generally, via SPH estimates of the gradient of a color function (Hu and Adams, 2006b).

Taking a step back and abstracting the details, the developed framework can be viewed as a black box solver that takes patient-specific input, i.e. geometry and blood parameters, and quantifies initiation and progress of atherosclerosis through modeling deposition patterns. By performing enough simulations and matching with many more sets of experimental data, this goal is certainly within reach. This was clearly demonstrated in the course of this work. However, atherosclerosis is only one example where the role of hemodynamics and short-range cell interactions is significant. As a result, the application of the framework could go beyond what is discussed in this work. For example, circulating tumor cells (CTCs) undergo very similar dynamics as white blood cells. Their size is roughly the same and they share many adhesion properties. Detachment of a cell from tumor and entering into the blood stream is an important stage in development and spreading of cancer. Therefore, the ability to detect this event early to adapt the treatment could save many lives. The problem is, due to low concentration of CTCs in blood, it is very difficult to detect them in time before they spread. To develop devices that detect low concentration of CTCs, this framework can allow plugging in of cell dynamics similar to those of CTCs. This example is one of many very exciting areas of research where this framework can be utilized.

# 6 Conclusions

In this work, a multiscale SPH framework for modeling WBC transport in the near region coupled with a stochastic adhesion method to capture realistic receptor-ligand adhesion is developed. The framework comes with a number of key benefits, namely accuracy and efficiency. Modeling the adhesion-deposition of cells in macroscopic scales typically presents many difficulties. Firstly, transport phenomenon takes place at considerably different temporal scales in the bulk and in the near-wall region. Secondly, near-wall cell transport behavior is largely affected by low-range adhesive forces between the cells and endothelium. Formation and dissolution of bonds that exert such forces occur in scales dictated mainly by characteristics of the receptor-ligand pair (rather than flow). Finally, even though there are several mathematical frameworks that address cell adhesion in depth, there are no well-established models that correlate physical quantities with model parameters. This is partly due to lack of consistency between the experimental setups and partly due to the complexity of the problem.

It was demonstrated that this framework is capable of addressing these two issues. Firstly, a multiscale Lagrangian model based on SPH which uses a discrete representation of cells only in the vicinity of walls was introduced. This approach results in significant reduction in number of cells. In order to address the second problem, adhesive forces through application of a Monte-Carlo acceptance-rejection method was prescribed. Experimental studies suggest that formation of a single bond is a significant event in determining the fate of the cell. Thus, existence of discrete cells near walls allows very accurate treatment of each cell as a stochastic process characterized by the type of cell. This approach allows for the development of adhesion parameter sets for each cell-receptor pair and to utilized this information in any simulation.

Moreover, it was demonstrated that this framework is capable of modeling a complex physiological phenomenon such as the adhesion of U937 monocytic human cell to an E-selectin coated geometry. In particular, it was shown that despite the large spatial scales of the problem (e.g. cell adhesion only occurs in the vicinity of the wall) we can accurately reproduce in-vitro results presented by Hinds et al. (2001). Additionally, we reaffirmed that adhesion under pulsatile flow conditions is

different from the equivalent Reynolds number steady flow adhesion.

Comparison of simulation results with experiment demonstrated that the framework provides a good platform for the investigation of WBC (and other cells) transport and adhesion under physiological flow conditions. Nevertheless an additional mention must be made about the accuracy of the adhesion results. The presented adhesion model offers several degrees of freedom to be able to match adhesion behavior of each cell type as accurately as possible. Hence, multiple parameter sets could give similar results for specific flow conditions. In order to make sure the final model is truly representative of a adhesion behavior of a particular adhesion molecule and cell, in the present study E-selectin-U937, additional experiments under different flow conditions, even in vivo animal models, are needed to validate and refine the parameters. Additionally, with the computational gain that the method delivers, it is possible to utilized our SPH framework in realistic arterial geometries. This flexibility will allow different *in vivo* flow environments to be assessed, in which natural geometric variations (see for example Thomas et al. (2005)) may highlight important aspects of WBC adhesion due to altered haemodynamics.

To close this chapter, published findings of this work are summarized in two sections.

## 6.1 Multiscale particle model

In this section, a summary of the published article (Gholami et al., 2014) is presented. This paper, titled *A multiscale SPH particle model of the near-wall dynamics of leukocytes in flow*, is published in the peer-reviewed *International Journal for Numerical Methods in Biomedical Engineering* [1]. It was submitted in January 2013 and accepted in July 2013. I was the first author [2].

The importance of WBC deposition patterns in the initiation of atherosclerosis has been demonstrated be several studies. In this paper, transport of leukocytes in large arteries is addressed with regard to large separation of spatio-temporal scales. Such a difference is the outcome of transport mechanisms in bulk and near-wall region being of different natures. While in bulk it is admissible to consider transport of leukocytes as passive scalar concentrations, their near-wall dynamics is by far more complex. In reality, it is virtually impossible to model transport of leukocytes in large arteries in any time scale that is relevant for the problem at hand. To

[1] http://onlinelibrary.wiley.com/journal/10.1002/(ISSN)2040-7947
[2] doi: http://dx.doi.org/10.1002/cnm.2591

address this issue, a multiscale model based on Lagrangian particles of SPH is proposed.

To simulate the complex near-wall dynamics of leukocytes, they are modeled as discrete particles which undergo specific lubrication, and potentially cell adhesion, forces. Such expression of leukocytes is however limited to regions in the vicinity of arterial walls where these forces are of significance. As mentioned, their bulk motion is tracked as a continuum passive concentration field. This arrangement leads to considerable gains in computational effort required to accurately capture long-term deposition patterns of WBCs in large arteries.

The bulk motion of leukocyte is modeled by advection/diffusion of a concentration field *mounted* on SPH particles. It should be noted that even though leukocyte Péclet number in large arteries is extremely large, on cell-size scale, their motion is affected by RBC-induced random motions resulting in an increased effective diffusion. Considering two possibilities to model this effective diffusion, i.e. treating the concentration as an independent SPH variable or incorporating momentum fluctuations for SPH particles, the second approach following the so-called smoothed dissipative particle dynamics method (SDPD) is used.

In the near-wall region, a Lagrangian particle tracking approach is used to model the motion of discrete tracers, representing leukocytes. Following finding of similar studies, stokes drag, lubrication forces, Saffman lift, and a random RBC-collision force are taken into account in this region. As accurate calculation of near-wall trajectories is feasible only with very small time steps, a first-order Euler scheme proved to be sufficient for avoiding trajectory instability. An intermediate study was carried out to ensure all relevant forces are being considered in calculating particle trajectories. Particle deposition is considered solely on the basis of wall distance. For particles closer than a minimum distance, chosen to be one tracer diameter, deposition probability of 1. Otherwise, probability of deposition is considered zero. It is worth noting that this criterion is chosen to isolate influence of blood flow on deposition pattern. In next steps, this condition needs to be modified to fit the complex dynamics of cell-endothelium adhesion.

Finally, a particle-tracer coupling scheme is introduced to couple bulk and near-wall solutions at the interface between the two domains. This scheme imposes conservation of mass at the interface. In *initialization*, each SPH particle is assigned a number of tracers based on local concentration. Therefore, a non-uniform bulk concentration of leukocytes, e.g. due to margination effects, is straightforward to impose. Through *extraction*, SPH particles entering the near-wall region convert the tracers they carry to discrete particles controlled by the LPT scheme. The reverse phenomenon is modeled in *insertion* steps where tracers that leave the

near-wall region are inserted in a nearby SPH particle. Considering these steps, it was demonstrated that the additional computation costs of this scheme is by far less that performing a full domain LPT.

Results were compared for case of backward-facing step (BFS) with a reference *validation* results that used full domain LPT. Despite the simplicity of the BFS geometry, it incorporates interesting flow features, such as sudden expansion and recirculating region, which are highly relevant for large arterial geometries like that carotid artery bifurcation. It was clearly demonstrated that after correct evaluation of the diffusion factor, result of the proposed method match those of the reference code very closely. These result are in agreement with other studies in that particle deposition is enhanced in regions of localized flow. Additionally, for the presented case, a minimum computational gain factor of 47 was consistently observed for different particles resolutions.

As a final demonstration of the capabilities of the proposed multiscale method, a local lesion was simulated by increasing the chance of deposition in a locality that otherwise has a low rate of deposition. This condition aims to model upregulation of adhesion molecules in dyfunctional endothelium. Results of validation LPT and the multiscale method consistently showed increased deposition rate at the lesion site almost as high as the reattachment point. This points out to the conclusion that studying leukocyte deposition purely based on hydrodynamics is not sufficient for realistic scenarios.

## 6.2 Stochastic adhesion model

In this section, a summary of the published article (Gholami et al., 2015) is presented. This paper, titled *SPH simulations of WBC adhesion to the endothelium: the role of haemodynamics and endothelial binding kinetics*, is published in the peer-reviewed journal of *Biomechanics and Modeling in Mechanobiology* [3]. It was submitted in December 2014 and accepted in April 2015. I was the first author [4].

In this paper, the extension of the multiscale Lagrangian particle solver to physiologically realistic near-wall cell dynamics is presented. In particular, this work approached the problem from three aspects. Firstly, extending the existing model to three-dimensional cases to capture full flow effects. This steps is the prerequisite of modeling patient-specific arterial geometries. Secondly, a stochastic cell adhesion model was introduced to model realistic receptor–ligand adhesion behavior. It

[3] http://www.springer.com/engineering/mechanics/journal/10237
[4] doi: http://dx.doi.org/10.1007/s10237-015-0676-y

was demonstrated in the previous work that even though hydrodynamics play an important role in deposition of leukocytes, it is far from sufficient in accurately predicting deposition patterns. The simple distance-based approach in the previous work is replaced by a detailed probabilistic model capable of simulation complete cell interactions in the vicinity of the endothelium. Finally, as influence of pulsatility is mentioned in a number of studies, appropriate inflow/outflow boundary conditions were implemented to capture effect of transient flow on leukocyte deposition.

As anticipated, one potential challenge when simulation in 3D is having to use an unfeasibly large number of tracers in the domain. However, after running preliminary convergence studies on simple three-dimensional models, it was clear that the multiscale model is capable of keeping the overall tracer count in a reasonable range while delivering descent accuracy. It was additionally decided to model bulk diffusion of tracer by treating the bulk concentration as an independent SPH variable. Even though the SDPD approach showed very good results in the previous work, the additional flexibility that this approach bring was considered necessary. Hence, each SPH particle carries a meaningful number of tracer at any time. This property is preferred in events such as wall restructuring due to particle accumulation. Overall, we considered this method more suiting for future extension of this work.

Experimental observations have shown that adhesion behavior of a cell is could radically change by flow conditions. Moreover, different cells exhibit very different adhesion characteristics. As a result, incorporating a proper model capable of counting these effects into account was absolutely necessary. An advanced approach in formulating binding affinity, i.e. ratio of bond formation to resolution, was adopted that adds bond force as a parameter. The advantage of the chosen model is that it allows simple to complex dependencies of biological parameters, flow conditions, and bond force with a unified formulation. This advantage is demonstrated in detail by studying parameter space of the binding affinity in the paper.

An important factor in implementing the adhesion model was a key observation by a number of experimental studies that formation of a single bond, regardless of current number of bonds, is a significant event in determining the adhesion of cells. Therefore, the adhesion process must be considered a stochastic process in small scales. As a result, a stochastic adhesion model, based on a Monte Carlo (MC) acceptance–rejection method, replaced the simplistic distance-based deposition criterion from the previous work. Based on this definition, the physical domain is divided into three parts: the bulk modeled by SPH, near-wall region by LPT, and adhesion region by MC.

To test the model, residence time distribution was studies for a concentration of U937 cells flowing through a three-dimensional stenosed axisymmetric sudden

expansion geometry. The inner surface of the model is coated with E-selectin to facilitate binding of the U937 cells at higher flow rates. First of all, the flow condition for two cases of Re = 100 and 140, was reproduced in SPH and wall shear stress (WSS) profiles were matches at walls. To demonstrate deficiencies of distance-based deposition, the Re = 100 case was tested without the new adhesion model. Expectedly, results showed a meaningful difference compared to those of the experiment.

Next, parameters of the stochastic adhesion model where tuned to reproduce results of the case with Re = 100. After successfully reproducing wall adhesion profiles for this case, adhesion parameters were applied to the case with Re = 140. The success of this step was key to this approach. Since in the experimental setup, used cell and corresponding coating where kept the same, the adhesion parameters should be treated as properties of the receptor-ligand pair, and therefore, kept identical to the first case. Result were in good agreement with those of the experiment. Both cases show accurate result in regions close to the contraction and sudden expansion, while slightly differ from the experimental data as we move further downstream.

The final step was to repeat the test for a case with pulsatile flow to capture realistic cardiovascular environment conditions. Transient fully-developed flow profiles were used at inlet as sufficient upstream length was available in the geometry under study. Inlet and outlet boundary condition were implemented using introducing ghost particles in inlet and outlet buffers. While this approach does not provide a perfectly non-reflecting condition at the boundaries, it is quite common in the SPH field and has shown good results problems that are not too complicated. While experimental data was not available to compare results quantitatively, a qualitative inspection of results in shows good agreement with experimental observations.

# Bibliography

K Affeld, AJ Reininger, J Gadischke, K Grunert, S Schmidt, and F Thiele. Fluid mechanics of the stagnation point flow chamber and its platelet deposition. *Artificial Organs*, 19(7):597–602, 1995.

B. Alberts, A. Johnson, J. Lewis, M. Raff, K. Roberts, and P. Walter. *The Molecular Biology of the Cell*. New York: Garland, 4 edition, 2002.

Ronen Alon, Daniel A Hammer, Timothy A Springer, et al. Lifetime of the p-selectin-carbohydrate bond and its response to tensile force in hydrodynamic flow. *Nature*, 374(6522):539–542, 1995.

Ronen Alon, Shuqi Chen, Kamal D Puri, Erik B Finger, and Timothy A Springer. The kinetics of l-selectin tethers and the mechanics of selectin-mediated rolling. *The Journal of cell biology*, 138(5):1169–1180, 1997.

Carla Antoci, Mario Gallati, and Stefano Sibilla. Numerical simulation of fluid–structure interaction by sph. *Computers & Structures*, 85(11):879–890, 2007.

Toshihisa Asakura and Takeshi Karino. Flow patterns and spatial distribution of atherosclerotic lesions in human coronary arteries. *Circulation research*, 66(4): 1045–1066, 1990.

K.M. Barber, A. Pinero, and G.A. Truskey. Effects of recirculating flow on u-937 cell adhesion to human umbilical vein endothelial cells. *American Journal of Physiology-Heart and Circulatory Physiology*, 275(2):H591, 1998.

IE Barton. Computation of particle tracks over a backward-facing step. *Journal of aerosol science*, 26(6):887–901, 1995.

IE Barton. Computation of dilute particulate laminar flow over a backward-facing step. *International journal for numerical methods in fluids*, 22(3):211–221, 1996.

G.K. Batchelor. *An introduction to fluid mechanics*. Cambridge University Press, Cambridge, 1967.

G.I. Bell. Models for the specific adhesion of cells to cells. *Science*, 200(4342):618, 1978.

G.I. Bell, M. Dembo, and P. Bongrand. Cell adhesion. competition between non-specific repulsion and specific bonding. *Biophysical journal*, 45(6):1051–1064, 1984.

Xin Bian, Sergey Litvinov, Rui Qian, Marco Ellero, and Nikolaus A Adams. Multiscale modeling of particle in suspension with smoothed dissipative particle dynamics. *Physics of Fluids*, 24:012002, 2012.

PJ Blanco, RA Feijóo, and SA Urquiza. A unified variational approach for coupling 3d–1d models and its blood flow applications. *Computer Methods in Applied Mechanics and Engineering*, 196(41):4391–4410, 2007.

R. Botnar, G. Rappitsch, M. Beat Scheidegger, D. Liepsch, K. Perktold, and P. Boesiger. Hemodynamics in the carotid artery bifurcation::: a comparison between numerical simulations and in vitro mri measurements. *Journal of biomechanics*, 33(2):137–144, 2000. ISSN 0021-9290.

JR Buchanan, C. Kleinstreuer, S. Hyun, and GA Truskey. Hemodynamics simulation and identification of susceptible sites of atherosclerotic lesion formation in a model abdominal aorta. *Journal of biomechanics*, 36(8):1185–1196, 2003.

RK Calay, Jutarat Kurujareon, and Arne Erik Holdø. Numerical simulation of respiratory flow patterns within human lung. *Respiratory physiology & neurobiology*, 130(2):201–221, 2002.

C. G. Caro, J. M. Fitz-Gerald, and R. C. Schroter. Atheroma and arterial wall shear observation, correlation and proposal of a shear dependent mass transfer mechanism for atherogenesis. *Proceedings of the Royal Society of London. Series B. Biological Sciences*, 177(1046):109–133, 1971.

Kai-Chien Chang and Daniel A Hammer. The forward rate of binding of surface-tethered reactants: effect of relative motion between two surfaces. *Biophysical journal*, 76(3):1280–1292, 1999.

Kai-Chien Chang, David FJ Tees, and Daniel A Hammer. The state diagram for cell adhesion under flow: leukocyte rolling and firm adhesion. *Proceedings of the National Academy of Sciences*, 97(21):11262–11267, 2000.

Gary B Chapman and Giles R Cokelet. Flow resistance and drag forces due to multiple adherent leukocytes in postcapillary vessels. *Biophysical journal*, 74(6): 3292–3301, 1998.

Phapanin Charoenphol, Ryan B Huang, and Omolola Eniola-Adefeso. Potential role of size and hemodynamics in the efficacy of vascular-targeted spherical drug carriers. *Biomaterials*, 31(6):1392–1402, 2010.

Shuqi Chen and Timothy A Springer. An automatic braking system that stabilizes leukocyte rolling by an increase in selectin bond number with shear. *The Journal of cell biology*, 144(1):185–200, 1999.

Yong Chen, Gaurav Girdhar, and Jin-Yu Shao. Single membrane tether extraction from adult and neonatal dermal microvascular endothelial cells. *American Journal of Physiology-Cell Physiology*, 292(4):C1272–C1279, 2007.

P. Cherukat and J.B. McLaughlin. The inertial lift on a rigid sphere in a linear shear flow field near a flat wall. *Journal of Fluid Mechanics*, 263(-1):1–18, 1994.

Scott E Chesla, Periasamy Selvaraj, and Cheng Zhu. Measuring two-dimensional receptor-ligand binding kinetics by micropipette. *Biophysical journal*, 75(3): 1553–1572, 1998.

J-J. Chiu and S. Chien. Effects of disturbed flow on vascular endothelium: pathophysiological basis and clinical perspectives. *Physiological reviews*, 91(1):327–387, 2011.

J-J. Chiu, S. Usami, and S. Chien. Vascular endothelial responses to altered shear stress: pathologic implications for atherosclerosis. *Annals of Medicine*, 41(1): 19–28, 2009.

J.J. Chiu, C.N. Chen, P.L. Lee, C. Tsair Yang, H. Sheng Chuang, S. Chien, and S. Usami. Analysis of the effect of disturbed flow on monocytic adhesion to endothelial cells. *Journal of biomechanics*, 36(12):1883–1895, 2003.

R Clift, JR Grace, and ME Weber. Bubbles, drops and particles. *Academic Press, New York*, 346, 1978.

A. Comerford and T. David. Computer model of nucleotide transport in a realistic porcine aortic trifurcation. *Annals of Biomedical Engineering*, 36(7):1175–1187, 2008.

Andrew Comerford, Sophie Rausch, Lena Wiechert, Michael W Gee, and Wolfgang A Wall. Computational modelling of the respiratory system for improvement of mechanical ventilation strategies. In *High Performance Computing in Science and Engineering, Garching/Munich 2009*, pages 267–277. Springer, 2010.

R.G. Cox and H. Brenner. The slow motion of a sphere through a viscous fluid towards a plane surface–ii small gap widths, including inertial effects. *Chemical Engineering Science*, 22(12):1753–1777, 1967.

Cindi Cozens-Roberts, Douglas A Lauffenburger, and John A Quinn. Receptor-mediated cell attachment and detachment kinetics. i. probabilistic model and analysis. *Biophysical journal*, 58(4):841, 1990a.

Cindi Cozens-Roberts, John A Quinn, and Douglas A Lauffenburger. Receptor-mediated cell attachment and detachment kinetics. ii. experimental model studies with the radial-flow detachment assay. *Biophysical journal*, 58(4):857, 1990b.

Mark A Crowther. Pathogenesis of atherosclerosis. *ASH Education Program Book*, 2005(1):436–441, 2005.

T David, S Thomas, and PG Walker. Platelet deposition in stagnation point flow: an analytical and computational simulation. *Medical engineering & physics*, 23 (5):299–312, 2001.

G. De Fabritiis, R. Delgado-Buscalioni, and PV Coveney. Multiscale modeling of liquids with molecular specificity. *Physical review letters*, 97(13):134501, 2006.

P Decuzzi and M Ferrari. The adhesive strength of non-spherical particles mediated by specific interactions. *Biomaterials*, 27(30):5307–5314, 2006.

Paolo Decuzzi and Mauro Ferrari. Design maps for nanoparticles targeting the diseased microvasculature. *Biomaterials*, 29(3):377–384, 2008.

Walter Dehnen and Hossam Aly. Improving convergence in smoothed particle hydrodynamics simulations without pairing instability. *Monthly Notices of the Royal Astronomical Society*, 425(2):1068–1082, 2012.

R. Delgado-Buscalioni and PV Coveney. Continuum-particle hybrid coupling for mass, momentum, and energy transfers in unsteady fluid flow. *Physical Review E*, 67(4):046704, 2003.

R Delgado-Buscalioni and A Dejoan. Nonreflecting boundaries for ultrasound in fluctuating hydrodynamics of open systems. *Physical Review E*, 78(4):046708, 2008.

M Dembo, DC Torney, K Saxman, and D Hammer. The reaction-limited kinetics of membrane-to-surface adhesion and detachment. *Proceedings of the Royal Society of London B: Biological Sciences*, 234(1274):55–83, 1988.

Micah Dembo. On peeling an adherent cell from a surface. *Lect. Math. Life Sci*, 24: 51–77, 1994.

José M Domínguez, Alejandro JC Crespo, Angelantonio Tafuni, Iskender Sahin, and Renato Vacondio. Open boundary conditions for large-scale sph simulations.

Cheng Dong, Jian Cao, Erika J Struble, and Herbert H Lipowsky. Mechanics of leukocyte deformation and adhesion to endothelium in shear flow. *Annals of biomedical engineering*, 27(3):298–312, 1999.

Michael L Dustin, Laura M Ferguson, Po-Ying Chan, Timothy A Springer, and David E Golan. Visualization of cd2 interaction with lfa-3 and determination of the two-dimensional dissociation constant for adhesion receptors in a contact area. *The Journal of cell biology*, 132(3):465–474, 1996.

Eugene C Eckstein and Fethi Belgacem. Model of platelet transport in flowing blood with drift and diffusion terms. *Biophysical journal*, 60(1):53–69, 1991.

M. Ellero and NA Adams. Sph simulations of flow around a periodic array of cylinders confined in a channel. *International Journal for Numerical Methods in Engineering*, 86(8):1027–1040, 2011.

M. Ellero and RI Tanner. Sph simulations of transient viscoelastic flows at low reynolds number. *Journal of Non-Newtonian Fluid Mechanics*, 132(1-3):61–72, 2005. ISSN 0377-0257.

M. Ellero, M. Kröger, and S. Hess. Viscoelastic flows studied by smoothed particle dynamics. *Journal of non-newtonian fluid mechanics*, 105(1):35–51, 2002.

Marco Ellero, Pep Espanol, and Eirik G Flekkøy. Thermodynamically consistent fluid particle model for viscoelastic flows. *Physical Review E*, 68(4):041504, 2003.

Pep Espanol and Mariano Revenga. Smoothed dissipative particle dynamics. *Physical review. E, Statistical, nonlinear, and soft matter physics*, 67(2 Pt 2):026705, 2003.

Pep Espanol and Patrick Warren. Statistical mechanics of dissipative particle dynamics. *EPL (Europhysics Letters)*, 30(4):191, 1995.

C.R. Ethier and C.A. Simmons. *Introductory biomechanics: from cells to organisms*. Cambridge University Press, Cambridge, 2007.

Evan Evans and Ken Ritchie. Dynamic strength of molecular adhesion bonds. *Biophysical journal*, 72(4):1541–1555, 1997.

Evan Evans, D Berk, and A Leung. Detachment of agglutinin-bonded red blood cells. i. forces to rupture molecular-point attachments. *Biophysical journal*, 59(4): 838–848, 1991.

EVAN A Evans. Detailed mechanics of membrane-membrane adhesion and separation. i. continuum of molecular cross-bridges. *Biophysical journal*, 48(1):175, 1985.

Mehrdad H Farahani, Nima Amanifard, and S Majid Hosseini. A fluid-structure interaction simulation by smoothed particle hydrodynamics. *Engineering Letters*, 17(1), 2009.

I Federico, S Marrone, A Colagrossi, F Aristodemo, and M Antuono. Simulating 2d open-channel flows through an sph model. *European Journal of Mechanics-B/Fluids*, 34:35–46, 2012.

D.A. Fedosov and G.E. Karniadakis. Triple-decker: interfacing atomistic-mesoscopic-continuum flow regimes. *Journal of Computational Physics*, 228(4):1157–1171, 2009.

DA Fedosov, B. Caswell, S. Suresh, and GE Karniadakis. Quantifying the biophysical characteristics of plasmodium-falciparum-parasitized red blood cells in microcirculation. *Proceedings of the National Academy of Sciences*, 108(1):35, 2011.

D.A. Fedosov, J. Fornleitner, and G. Gompper. Margination of white blood cells in microcapillary flow. *Physical Review Letters*, 108(2):028104, 2012.

Martin Ferrand, DR Laurence, BD Rogers, Damien Violeau, and Christophe Kassiotis. Unified semi-analytical wall boundary conditions for inviscid, laminar or turbulent flows in the meshless sph method. *International Journal for Numerical Methods in Fluids*, 71(4):446–472, 2013.

E.G. Flekkøy, R. Delgado-Buscalioni, and P.V. Coveney. Flux boundary conditions in particle simulations. *Physical Review E*, 72(2):026703, 2005.

Ernst-Ludwig Florin, Vincent T Moy, and Hermann E Gaub. Adhesion forces between individual ligand-receptor pairs. *Science*, 264(5157):415–417, 1994.

Luca Formaggia, Jean-Frédéric Gerbeau, Fabio Nobile, and Alfio Quarteroni. Numerical treatment of defective boundary conditions for the navier–stokes equations. *SIAM Journal on Numerical Analysis*, 40(1):376–401, 2002.

Luca Formaggia, Daniele Lamponi, Massimiliano Tuveri, and Alessandro Veneziani. Numerical modeling of 1d arterial networks coupled with a lumped parameters description of the heart. *Computer methods in biomechanics and biomedical engineering*, 9(5):273–288, 2006.

Luca Formaggia, Alexandra Moura, and Fabio Nobile. On the stability of the coupling of 3d and 1d fluid-structure interaction models for blood flow simulations. *ESAIM: Mathematical Modelling and Numerical Analysis*, 41(4):743–769, 2007.

Bernard Fox, Keith James, Barbara Morgan, and Anthony Seed. Distribution of fatty and fibrous plaques in young human coronary arteries. *Atherosclerosis*, 41 (2):337–347, 1982.

Rainhill K Freitas and Wolfgang Schröder. Numerical investigation of the three-dimensional flow in a human lung model. *Journal of Biomechanics*, 41(11): 2446–2457, 2008.

David A Fulk and Dennis W Quinn. An analysis of 1-d smoothed particle hydrodynamics kernels. *Journal of Computational Physics*, 126(1):165–180, 1996.

Diego Gallo, David A Steinman, Payam B Bijari, and Umberto Morbiducci. Helical flow in carotid bifurcation as surrogate marker of exposure to disturbed shear. *Journal of biomechanics*, 2012.

T Gemci, Valery Ponyavin, Y Chen, H Chen, and R Collins. Computational model of airflow in upper 17 generations of human respiratory tract. *Journal of Biomechanics*, 41(9):2047–2054, 2008.

Babak Gholami, Andrew Comerford, and Marco Ellero. Multiscale modeling of leukocyte dynamics in large arteries. In *Proceedings of 9th European Fluid Mechanics Conference - EFMC9, Rome, Italy September 9-13, 2012*, 2012.

Babak Gholami, Andrew Comerford, and Marco Ellero. A multiscale sph modeling of near-wall dynamics of leukocytes in flow. In *Proceedings of the 8th INTERNATIONAL SPHERIC SPH Workshop, Sintef, Trondheim, Norway June 4-6, 2013*, 2013.

Babak Gholami, Andrew Comerford, and Marco Ellero. A multiscale sph particle model of the near-wall dynamics of leukocytes in flow. *International journal for numerical methods in biomedical engineering*, 30(1):83–102, 2014.

Babak Gholami, Andrew Comerford, and Marco Ellero. Sph simulations of wbc adhesion to the endothelium: the role of haemodynamics and endothelial binding kinetics. *Biomechanics and modeling in mechanobiology*, pages 1–17, 2015.

Michael A. Gimbrone, James N Topper, Tobi Nagel, Keith R Anderson, and Guillermo Garcia-Cardeña. Endothelial dysfunction, hemodynamic forces, and atherogenesisa. *Annals of the New York Academy of Sciences*, 902(1):230–240, 2000.

M. A. Gimbrone Jr, T. Nagel, and J. N. Topper. Biomechanical activation: an emerging paradigm in endothelial adhesion biology. *Journal of Clinical Investigation*, 99(8):1809, 1997.

R.A. Gingold and J.J. Monaghan. Smoothed particle hydrodynamics-theory and application to non-spherical stars. *Monthly Notices of the Royal Astronomical Society*, 181:375–389, 1977.

S. Glagov, C. Zarins, D. P. Giddens, and D. N. Ku. Hemodynamics and atherosclerosis. insights and perspectives gained from studies of human arteries. *Archives of pathology & laboratory medicine*, 112(10):1018–1031, 1988.

AJ Goldman, RG Cox, and H. Brenner. Slow viscous motion of a sphere parallel to a plane wall–i motion through a quiescent fluid. *Chemical Engineering Science*, 22(4):637–651, 1967a.

AJ Goldman, RG Cox, and H. Brenner. Slow viscous motion of a sphere parallel to a plane wall–ii couette flow. *Chemical Engineering Science*, 22(4):653–660, 1967b.

Harry L Goldsmith and Samira Spain. Margination of leukocytes in blood flow through small tubes. *Microvascular research*, 27(2):204–222, 1984.

H.L. Goldsmith and T. Karino. Microscopic considerations: The motions of individual particles. *Annals of the New York Academy of Sciences*, 283(1):241–255, 1977.

Leopold Grinberg and George Em Karniadakis. Outflow boundary conditions for arterial networks with multiple outlets. *Annals of biomedical engineering*, 36(9): 1496–1514, 2008.

Leopold Grinberg, T Anor, JR Madsen, A Yakhot, and GE Karniadakis. Large-scale simulation of the human arterial tree. *Clinical and Experimental Pharmacology and Physiology*, 36(2):194–205, 2009.

Robert D Groot and Patrick B Warren. Dissipative particle dynamics: Bridging the gap between atomistic and mesoscopic simulation. *Journal of Chemical Physics*, 107(11):4423, 1997.

Daniel A Hammer and Sachin M Apte. Simulation of cell rolling and adhesion on surfaces in shear flow: general results and analysis of selectin-mediated neutrophil adhesion. *Biophysical Journal*, 63(1):35–57, 1992.

DANIEL A Hammer and DOUGLAS A Lauffenburger. A dynamical model for receptor-mediated cell adhesion to surfaces. *Biophysical journal*, 52(3):475, 1987.

J. Hanzlik, E. Cretekos, and KA Lamkin-Kennard. Biomimetic leukocyte adhesion: A review of microfluidic and computational approaches and applications. *Journal of Bionic Engineering*, 5(4):317–327, 2008.

Jered B Haun and Daniel A Hammer. Quantifying nanoparticle adhesion mediated by specific molecular interactions. *Langmuir*, 24(16):8821–8832, 2008.

Robert A Hegele. The pathogenesis of atherosclerosis. *Clinica Chimica Acta*, 246 (1):21–38, 1996.

S.E. Hieber, J.H. Walther, and P. Koumoutsakos. Remeshed smoothed particle hydrodynamics simulation of the mechanical behavior of human organs. *Technology and Health Care-European Society for Engineering and Medicine*, 12(4):305–314, 2004.

M.T. Hinds, Y.J. Park, S.A. Jones, D.P. Giddens, and B. Rita Alevriadou. Local hemodynamics affect monocytic cell adhesion to a three-dimensional flow model coated with e-selectin. *Journal of Biomechanics*, 34(1):95–103, 2001.

Manuel Hirschler, Philip Kunz, Manuel Huber, Friedemann Hahn, and Ulrich Nieken. Open boundary conditions for isph and their application to micro-flow. *Journal of Computational Physics*, 307:614–633, 2016.

DW Holdsworth, CJD Norley, R Frayne, DA Steinman, and BK Rutt. Characterization of common carotid artery blood-flow waveforms in normal human subjects. *Physiological measurement*, 20(3):219, 1999.

PJ Hoogerbrugge and JMVA Koelman. Simulating microscopic hydrodynamic phenomena with dissipative particle dynamics. *EPL (Europhysics Letters)*, 19(3): 155, 1992.

S. S. Hossain, T. J. R. Hughes, and P. Decuzzi. Vascular deposition patterns for nanoparticles in an inflamed patient-specific arterial tree. *Biomechanics and Modeling in Mechanobiology*, 13(3):585–597, 2014.

S Majid Hosseini and James J Feng. Pressure boundary conditions for computing incompressible flows with sph. *Journal of Computational physics*, 230(19):7473–7487, 2011.

S.M. Hosseini and J.J. Feng. A particle-based model for the transport of erythrocytes in capillaries. *Chemical Engineering Science*, 64(22):4488–4497, 2009.

Q Hou, ACH Kruisbrink, FR Pearce, AS Tijsseling, and T Yue. Smoothed particle hydrodynamics simulations of flow separation at bends. *Computers & Fluids*, 90: 138–146, 2014.

Tzung K Hsiai, Sung K Cho, Pak K Wong, Mike Ing, Adler Salazar, Alex Sevanian, Mohamad Navab, Linda L Demer, and Chih-Ming Ho. Monocyte recruitment to endothelial cells in response to oscillatory shear stress. *The FASEB Journal*, 17 (12):1648–1657, 2003.

XY Hu and NA Adams. Angular-momentum conservative smoothed particle dynamics for incompressible viscous flows. *Physics of Fluids*, 18:101702, 2006a.

XY Hu and NA Adams. A multi-phase sph method for macroscopic and mesoscopic flows. *Journal of Computational Physics*, 213(2):844–861, 2006b. ISSN 0021-9991.

M Ismail, V Gravemeier, A Comerford, and WA Wall. A stable approach for coupling multidimensional cardiovascular and pulmonary networks based on a novel pressure-flow rate or pressure-only neumann boundary condition formulation. *International Journal for Numerical Methods in Biomedical Engineering*, 2013a.

Mahmoud Ismail, Michael W Gee, and Wolfgang A Wall. Cfd challenge: hemodynamic simulation of a patient-specific aortic coarctation model with adjoint-based calibrated windkessel elements. In *Statistical Atlases and Computational Models of the Heart. Imaging and Modelling Challenges*, pages 44–52. Springer, 2013b.

R. Issa. Numerical assessment of the smoothed particle hydrodynamics gridless method for incompressible flows and its extension to turbulent flows. *UMIST*, 2005.

Sameer Jadhav, Charles D Eggleton, and Konstantinos Konstantopoulos. A 3-d computational model predicts that cell deformation affects selectin-mediated leukocyte rolling. *Biophysical journal*, 88(1):96–104, 2005.

Woowon Jeong, Moon June Kim, and Kyehan Rhee. Computational study of particle size effects on selective binding of nanoparticles in arterial stenosis. *Computers in biology and medicine*, 43(5):417–424, 2013.

Gilles Kaplanski, C Farnarier, O Tissot, A Pierres, AM Benoliel, MC Alessi, S Kaplanski, and P Bongrand. Granulocyte-endothelium initial adhesion. analysis of transient binding events mediated by e-selectin in a laminar shear flow. *Biophysical journal*, 64(6):1922, 1993.

T Karino and HL Goldsmith. Flow behaviour of blood cells and rigid spheres in an annular vortex. *Philosophical Transactions of the Royal Society of London. B, Biological Sciences*, 279(967):413–445, 1977.

C Kassiotis, D Violeau, and M Ferrand. Semi-analytical conditions for open boundaries in smoothed particle hydrodynamics. In *Proceedings of 8th international SPHERIC workshop, paper*, pages 1–4, 2013.

Damir B Khismatullin. The cytoskeleton and deformability of white blood cells. *Leukocyte adhesion*, 64:47–111, 2009.

Damir B Khismatullin and George A Truskey. Three-dimensional numerical simulation of receptor-mediated leukocyte adhesion to surfaces: Effects of cell deformability and viscoelasticity. *Physics of Fluids (1994-present)*, 17(3):031505, 2005.

Sh Khorasanizade and JMM Sousa. An innovative open boundary treatment for incompressible sph. *International Journal for Numerical Methods in Fluids*, 80 (3):161–180, 2016.

Sh Khorasanizade, JF Pinto, and JMM Sousa. On the use of inflow/outflow boundary conditions in incompressible internal flow problems using smoothed particle hydrodynamics. In *Proceedings of ECCOMAS*, 2012.

Hyun Jin Kim, CA Figueroa, TJR Hughes, KE Jansen, and CA Taylor. Augmented lagrangian method for constraining the shape of velocity profiles at outlet boundaries for three-dimensional finite element simulations of blood flow. *Computer Methods in Applied Mechanics and Engineering*, 198(45):3551–3566, 2009a.

Hyun Jin Kim, Irene E Vignon-Clementel, C Alberto Figueroa, John F LaDisa, Kenneth E Jansen, Jeffrey A Feinstein, and Charles A Taylor. On coupling a lumped parameter heart model and a three-dimensional finite element aorta model. *Annals of biomedical engineering*, 37(11):2153–2169, 2009b.

Min-Cheol Kim, Jin Hyun Nam, and Chong-Sun Lee. Near-wall deposition probability of blood elements as a new hemodynamic wall parameter. *Annals of biomedical engineering*, 34(6):958–970, 2006.

Moon June Kim and Kyehan Rhee. Computational analysis of nanoparticle adhesion to endothelium: effects of kinetic rate constants and wall shear rates. *Medical & biological engineering & computing*, 49(7):733–741, 2011.

Michael R King and Daniel A Hammer. Multiparticle adhesive dynamics: hydrodynamic recruitment of rolling leukocytes. *Proceedings of the National Academy of Sciences*, 98(26):14919–14924, 2001a.

Michael R King, Volkmar Heinrich, Evan Evans, and Daniel A Hammer. Nano-to-micro scale dynamics of p-selectin detachment from leukocyte interfaces. iii. numerical simulation of tethering under flow. *Biophysical journal*, 88(3):1676–1683, 2005.

M.R. King and D.A. Hammer. Multiparticle adhesive dynamics. interactions between stably rolling cells. *Biophysical journal*, 81(2):799–813, 2001b.

P. Koumoutsakos. Multiscale flow simulations using particles. *Annu. Rev. Fluid Mech.*, 37:457–487, 2005. ISSN 0066-4189.

D.N. Ku. Blood flow in arteries. *Annual Review of Fluid Mechanics*, 29(1):399–434, 1997. ISSN 0066-4189.

D.N. Ku, D.P. Giddens, C.K. Zarins, and S. Glagov. Pulsatile flow and atherosclerosis in the human carotid bifurcation. positive correlation between plaque location and low oscillating shear stress. *Arteriosclerosis, Thrombosis, and Vascular Biology*, 5 (3):293–302, 1985.

Sivakumar Kulasegaram, Javier Bonet, RW Lewis, and M Profit. A variational formulation based contact algorithm for rigid boundaries in two-dimensional sph applications. *Computational Mechanics*, 33(4):316–325, 2004.

Mads J Kunov, DA Steinmass, and C Ross Ethier. Particle volumetric residence time calculations in arterial geometries. *Journal of biomechanical engineering*, 118(2):158–164, 1996.

Martin Lastiwka, Mihai Basa, and Nathan J Quinlan. Permeable and non-reflecting boundary conditions in sph. *International journal for numerical methods in fluids*, 61(7):709–724, 2009.

Sang-Wook Lee, Luca Antiga, J David Spence, and David A Steinman. Geometry of the carotid bifurcation predicts its exposure to disturbed flow. *Stroke*, 39(8): 2341–2347, 2008.

H. Lei, D.A. Fedosov, and G.E. Karniadakis. Time-dependent and outflow boundary conditions for dissipative particle dynamics. *Journal of Computational Physics*, 2011. ISSN 0021-9991.

M Lei, C Kleinstreuer, and GA Truskey. A focal stress gradient-dependent mass transfer mechanism for atherogenesis in branching arteries. *Medical engineering & physics*, 18(4):326–332, 1996.

A Leroy, D Violeau, M Ferrand, L Fratter, and A Joly. A new open boundary formulation for incompressible sph. *Computers & Mathematics with Applications*, 2016.

Ping Li, Periasamy Selvaraj, and Cheng Zhu. Analysis of competition binding between soluble and membrane-bound ligands for cell surface receptors. *Biophysical journal*, 77(6):3394–3406, 1999.

Peter Libby, Paul M Ridker, and Attilio Maseri. Inflammation and atherosclerosis. *Circulation*, 105(9):1135–1143, 2002.

S. Litvinov, M. Ellero, X. Hu, and N.A. Adams. Self-diffusion coefficient in smoothed dissipative particle dynamics. *The Journal of chemical physics*, 130:021101, 2009.

G.R. Liu and MB Liu. *Smoothed particle hydrodynamics: a meshfree particle method*. World Scientific Pub Co Inc, 2003. ISBN 9812384561.

MB Liu and GR Liu. Smoothed particle hydrodynamics (sph): an overview and recent developments. *Archives of computational methods in engineering*, 17(1): 25–76, 2010.

Wing Kam Liu, Sukky Jun, and Yi Fei Zhang. Reproducing kernel particle methods. *International journal for numerical methods in fluids*, 20(8-9):1081–1106, 1995.

Mian Long, Harry L Goldsmith, David FJ Tees, and Cheng Zhu. Probabilistic modeling of shear-induced formation and breakage of doublets cross-linked by receptor-ligand bonds. *Biophysical journal*, 76(2):1112–1128, 1999.

P. Longest and C. Kleinstreuer. Particle-hemodynamics modeling of the distal end-to-side femoral bypass: effects of graft caliber and graft-end cut. *Medical engineering & physics*, 25(10):843–858, 2003.

P. Longest, C. Kleinstreuer, and J.R. Buchanan. Efficient computation of micro-particle dynamics including wall effects. *Computers & Fluids*, 33(4):577–601, 2004. ISSN 0045-7930.

P.W. Longest. *Computational analyses of transient particle hemodynamics with applications to femoral bypass graft designs*. PhD thesis, MAE Dept., NC State University, Raleigh, NC, 2002.

P.W. Longest, C. Kleinstreuer, G.A. Truskey, and J.R. Buchanan. Relation between near-wall residence times of monocytes and early lesion growth in the rabbit aorto–celiac junction. *Annals of biomedical engineering*, 31(1):53–64, 2003.

E. Loth. Numerical approaches for motion of dispersed particles, droplets and bubbles. *Progress in Energy and Combustion Science*, 26(3):161–223, 2000. ISSN 0360-1285.

L.B. Lucy. A numerical approach to the testing of the fission hypothesis. *The Astronomical Journal*, 82:1013–1024, 1977. ISSN 0004-6256.

HY Luo, Y Liu, and XL Yang. Particle deposition in obstructed airways. *Journal of Biomechanics*, 40(14):3096–3104, 2007.

A. J. Lusis. Atherosclerosis. *Nature*, 407:233–241, 2000.

R.W. Lyczkowski, B.R. Alevriadou, M. Horner, C.B. Panchal, and S.G. Shroff. Application of multiphase computational fluid dynamics to analyze monocyte adhesion. *Annals of biomedical engineering*, 37(8):1516–1533, 2009.

Kirill Lykov, Xuejin Li, Huan Lei, Igor V Pivkin, and George Em Karniadakis. Inflow/outflow boundary conditions for particle-based blood flow simulations: Application to arterial bifurcations and trees. *PLoS Comput Biol*, 11(8):e1004410, 2015.

A Cristiano I Malossi, Pablo J Blanco, Simone Deparis, and Alfio Quarteroni. Algorithms for the partitioned solution of weakly coupled fluid models for cardiovascular flows. *International Journal for Numerical Methods in Biomedical Engineering*, 27(12):2035–2057, 2011.

Bryan T Marshall, Krishna K Sarangapani, Jizhong Lou, Rodger P McEver, and Cheng Zhu. Force history dependence of receptor-ligand dissociation. *Biophysical journal*, 88(2):1458–1466, 2005.

M.R. Maxey and J.J. Riley. Equation of motion for a small rigid sphere in a nonuniform flow. *Physics of Fluids*, 26:883–889, 1983.

V. Z. McKinney, K. D. Rinker, and G. A. Truskey. Normal and shear stresses influence the spatial distribution of intracellular adhesion molecule-1 expression in human umbilical vein endothelial cells exposed to sudden expansion flow. *Journal of Biomechanics*, 39(5):806–817, 2006.

Donald A McQuarrie. Kinetics of small systems. i. *The journal of chemical physics*, 38(2):433–436, 1963.

Robert J Melder, Elizabeth Walker, Ronald B Herberman, and Theresa L Whiteside. Adhesion characteristics of human interleukin 2-activated natural killer cells. *Cellular immunology*, 132(1):177–192, 1991.

R Merkel, P Nassoy, A Leung, K_ Ritchie, and E Evans. Energy landscapes of receptor–ligand bonds explored with dynamic force spectroscopy. *Nature*, 397 (6714):50–53, 1999.

Mahdi Esmaily Moghadam, Yuri Bazilevs, Tain-Yen Hsia, Irene E Vignon-Clementel, Alison L Marsden, et al. A comparison of outlet boundary treatments for prevention of backflow divergence with relevance to blood flow simulations. *Computational Mechanics*, 48(3):277–291, 2011.

J. J. Monaghan. Smoothed particle hydrodynamics. *Annual Review of Astronomy and Astrophysics*, 30:543–574, 1992. doi: 10.1146/annurev.aa.30.090192.002551.

J.J. Monaghan. Simulating free surface flows with sph. *Journal of computational physics*, 110(2):399–406, 1994.

J.J. Monaghan. Smoothed particle hydrodynamics. *Reports on Progress in Physics*, 68:1703, 2005.

J.J. Monaghan. Smoothed particle hydrodynamics and its diverse applications. *Annual Review of Fluid Mechanics*, 44(1), 2012.

Joseph J Monaghan and John C Lattanzio. A refined particle method for astrophysical problems. *Astronomy and astrophysics*, 149:135–143, 1985.

Kathryn J Moore, Frederick J Sheedy, and Edward A Fisher. Macrophages in atherosclerosis: a dynamic balance. *Nature Reviews Immunology*, 13(10):709–721, 2013.

Kevin L Moore, Kamala D Patel, Richard E Bruehl, F Li, David A Johnson, Henri S Lichenstein, Richard D Cummings, Dorothy F Bainton, and Rodger P McEver. P-selectin glycoprotein ligand-1 mediates rolling of human neutrophils on p-selectin. *The Journal of cell biology*, 128(4):661–671, 1995.

J.P. Morris, P.J. Fox, and Y. Zhu. Modeling low reynolds number incompressible flows using sph. *Journal of Computational Physics*, 136(1):214–226, 1997. ISSN 0021-9991.

Keri R Moyle, Luca Antiga, and David A Steinman. Inlet conditions for image-based cfd models of the carotid bifurcation: is it reasonable to assume fully developed flow? *Journal of biomechanical engineering*, 128(3):371–379, 2006.

M. Müller, S. Schirm, and M. Teschner. Interactive blood simulation for virtual surgery based on smoothed particle hydrodynamics. *Technology and Health Care-European Society for Engineering and Medicine*, 12(1):25–32, 2004a.

M. Müller, S. Schirm, M. Teschner, B. Heidelberger, and M. Gross. Interaction of fluids with deformable solids. *Computer Animation and Virtual Worlds*, 15(3-4): 159–171, 2004b.

L.L. Munn, R.J. Melder, and R.K. Jain. Role of erythrocytes in leukocyte-endothelial interactions: mathematical model and experimental validation. *Biophysical journal*, 71(1):466–478, 1996. ISSN 0006-3495.

R. M. Nerem and J. F. Cornhill. The role of fluid mechanics in atherogenesis. *Journal of Biomechanical Engineering*, 102(3):181–189, 1980.

R. M. Nerem, R. W. Alexander, D. C. Chappell, R. M. Medford, S. E. Varner, and W. R. Taylor. The study of the influence of flow on vascular endothelial biology. *The American journal of the medical sciences*, 316(3):169–175, 1998.

KE Norman, KL Moore, RP McEver, and K Ley. Leukocyte rolling in vivo is mediated by p-selectin glycoprotein ligand-1. *Blood*, 86(12):4417–4421, 1995.

Natalya Nowak, Prashant P Kakade, and Ananth V Annapragada. Computational fluid dynamics simulation of airflow and aerosol deposition in human lungs. *Annals of biomedical engineering*, 31(4):374–390, 2003.

Mette S Olufsen. Structured tree outflow condition for blood flow in larger systemic arteries. *American journal of physiology-Heart and circulatory physiology*, 276(1): H257–H268, 1999.

H. Ounis and G. Ahmadi. Analysis of dispersion of small spherical particles in a random velocity field. *Journal of fluids engineering*, 112(1):114–120, 1990.

R. Packard and P. Libby. Inflammation in atherosclerosis: from vascular biology to biomarker discovery and risk prediction. *Clinical chemistry*, 54(1):24–38, 2008.

Eric YH Park, McRae J Smith, Emily S Stropp, Karen R Snapp, Jeffrey A DiVietro, William F Walker, David W Schmidtke, Scott L Diamond, and Michael B Lawrence. Comparison of psgl-1 microbead and neutrophil rolling: microvillus elongation stabilizes p-selectin bond clusters. *Biophysical Journal*, 82(4): 1835–1847, 2002.

Sean Peterson and Michael Plesniak. Experimental study of the effect of a skewed inlet flow profile on stenotic flow development. In *APS Division of Fluid Dynamics Meeting Abstracts*, volume 1, 2006.

Anne Pierres, Anne-Marie Benoliel, and Pierre Bongrand. Measuring the lifetime of bonds made between surface-linked molecules. *Journal of Biological Chemistry*, 270(44):26586–26592, 1995.

James Wilson Piper. Force dependence of cell bound e-selectin/carbohydrate ligand binding characteristics. 1997.

J.W. Piper, R.A. Swerlick, and C. Zhu. Determining force dependence of two-dimensional receptor-ligand binding affinity by centrifugation. *Biophysical journal*, 74(1):492–513, 1998.

Sujata Prakash and C Ross Ethier. Requirements for mesh resolution in 3d computational hemodynamics. *Journal of biomechanical engineering*, 123(2):134–144, 2001.

W.F. Pritchard, P.F. Davies, Z. Derafshi, D.C. Polacek, R. Tsao, R.O. Dull, S.A. Jones, and D.P. Giddens. Effects of wall shear stress and fluid recirculation on the localization of circulating monocytes in a three-dimensional flow model. *Journal of biomechanics*, 28(12):1459–1469, 1995.

Vishwanath Ramachandran, Marcie Williams, Tadayuki Yago, David W Schmidtke, and Rodger P McEver. Dynamic alterations of membrane tethers stabilize leukocyte rolling on p-selectin. *Proceedings of the National Academy of Sciences of the United States of America*, 101(37):13519–13524, 2004.

K.D. Rinker, V. Prabhakar, and G.A. Truskey. Effect of contact time and force on monocyte adhesion to vascular endothelium. *Biophysical Journal*, 80(4):1722–1732, 2001.

Russell Ross. The pathogenesis of atherosclerosis: a perspective for the 1990s. 1993.

Russell Ross. Atherosclerosis - an inflammatory disease. *New England Journal of Medicine*, 340(2):115–126, 1999. doi: 10.1056/NEJM199901143400207. URL http://www.nejm.org/doi/full/10.1056/NEJM199901143400207.

Leonie Rouleau, Ian B Copland, Jean-Claude Tardif, Rosaire Mongrain, and Richard L Leask. Neutrophil adhesion on endothelial cells in a novel asymmetric stenosis model: effect of wall shear stress gradients. *Annals of biomedical engineering*, 38(9):2791–2804, 2010.

P.G. Saffman. The lift on a small sphere in a slow shear flow. *Journal of Fluid Mechanics*, 22(02):385–400, 1965.

I. Sazonov and P. Nithiarasu. Semi-automatic surface and volume mesh generation for subject-specific biomedical geometries. *International Journal for Numerical Methods in Biomedical Engineering*, 2012.

Igor Sazonov, Si Yong Yeo, Rhodri LT Bevan, Xianghua Xie, Raoul van Loon, and Perumal Nithiarasu. Modelling pipeline for subject-specific arterial blood flow—a review. *International Journal for Numerical Methods in Biomedical Engineering*, 27(12):1868–1910, 2011.

Igor Sazonov, Xianghua Xie, and Perumal Nithiarasu. An improved method of computing geometrical potential force (gpf) employed in the segmentation of 3d and 4d medical images. *Computer Methods in Biomechanics and Biomedical Engineering: Imaging & Visualization*, 5(4):287–296, 2017.

IF Sbalzarini, J.H. Walther, M. Bergdorf, SE Hieber, EM Kotsalis, and P. Koumoutsakos. Ppm-a highly efficient parallel particle-mesh library for the simulation of continuum systems. *Journal of Computational Physics*, 215(2):566–588, 2006. ISSN 0021-9991.

Isaac Jacob Schönberg. Contributions to the problem of approximation of equidistant data by analytic functions. *Quart. Appl. Math*, 4(2):45–99, 1946.

S. Shahriari. *Computational Modeling of Cardiovascular Flows using Smoothed Particle Hydrodynamics*. PhD thesis, Concordia University, 2011.

S Shahriari, L Kadem, BD Rogers, and I Hassan. Smoothed particle hydrodynamics method applied to pulsatile flow inside a rigid two-dimensional model of left heart cavity. *International journal for numerical methods in biomedical engineering*, 28 (11):1121–1143, 2012.

Jin-Yu Shao, Hie Ping Ting-Beall, and Robert M Hochmuth. Static and dynamic lengths of neutrophil microvilli. *Proceedings of the National Academy of Sciences*, 95(12):6797–6802, 1998.

SJ Sherwin, V Franke, J Peiró, and K Parker. One-dimensional modelling of a vascular network in space-time variables. *Journal of Engineering Mathematics*, 47(3-4):217–250, 2003.

Scott I Simon and Harry L Goldsmith. Leukocyte adhesion dynamics in shear flow. *Annals of biomedical engineering*, 30(3):315–332, 2002.

MD Sinnott, P.W. Cleary, and M. PRAKASH. An investigation of pulsatile blood flow in a bifurcation artery using a grid-free method. In *Proc. Fifth International Conference on CFD in the Process Industries*, page 6 pp. CSIRO Minerals, Clayton South, Vic., Australia, 2006.

C. Skilbeck, S.M. Westwood, P.G. Walker, T. David, and G.B. Nash. Population of the vessel wall by leukocytes binding to p-selectin in a model of disturbed arterial flow. *Arteriosclerosis, thrombosis, and vascular biology*, 21(8):1294, 2001.

C.A. Skilbeck, P.G. Walker, T. David, and G.B. Nash. Disturbed flow promotes deposition of leucocytes from flowing whole blood in a model of a damaged vessel wall. *British journal of haematology*, 126(3):418–427, 2004.

B. Soni and D. Thompson. Effects of temporally varying inlet conditions on flow and particle deposition in the small bronchial tubes. *International Journal for Numerical Methods in Biomedical Engineering*, 2012.

Ryan L Spilker, Jeffrey A Feinstein, David W Parker, V Mohan Reddy, and Charles A Taylor. Morphometry-based impedance boundary conditions for patient-specific modeling of blood flow in pulmonary arteries. *Annals of biomedical engineering*, 35(4):546–559, 2007.

Volker Springel. Smoothed particle hydrodynamics in astrophysics. *Annual Review of Astronomy and Astrophysics*, 48:391–430, 2010.

Daniel Steinberg. Low density lipoprotein oxidation and its pathobiological significance. *Journal of Biological Chemistry*, 272(34):20963–20966, 1997.

DA Steinman, DA Vorp, and CR Ethier. Computational modeling of arterial biomechanics: Insights into pathogenesis and treatment of vascular disease. *Journal of vascular surgery*, 37(5):1118–1128, 2003.

C. Sun, C. Migliorini, and L.L. Munn. Red blood cells initiate leukocyte rolling in postcapillary expansions: a lattice boltzmann analysis. *Biophysical journal*, 85 (1):208–222, 2003. ISSN 0006-3495.

Chenghai Sun and Lance L Munn. Particulate nature of blood determines macroscopic rheology: a 2-d lattice boltzmann analysis. *Biophysical journal*, 88(3): 1635–1645, 2005.

Prithu Sundd, Maria K Pospieszalska, Luthur Siu-Lun Cheung, Konstantinos Konstantopoulos, and Klaus Ley. Biomechanics of leukocyte rolling. *Biorheology*, 48(1):1–35, 2011.

M. Tambasco, D.A. Steinman, et al. On assessing the quality of particle tracking through computational fluid dynamic models. *TRANSACTIONS-AMERICAN SOCIETY OF MECHANICAL ENGINEERS JOURNAL OF BIOMECHANICAL ENGINEERING*, 124(2):166–175, 2002.

N. Tanaka and T. Takano. Microscopic-scale simulation of blood flow using sph method. *International Journal of Computational Methods*, 2(04):555–568, 2004.

Charles A Taylor and Mary T Draney. Experimental and computational methods in cardiovascular fluid mechanics. *Annu. Rev. Fluid Mech.*, 36:197–231, 2004.

DF Tees, Olivier Coenen, and Harry L Goldsmith. Interaction forces between red cells agglutinated by antibody. iv. time and force dependence of break-up. *Biophysical journal*, 65(3):1318–1334, 1993.

D.F.J. Tees and D.J. Goetz. Leukocyte adhesion: an exquisite balance of hydrodynamic and molecular forces. *News in physiological sciences*, 18:186–190, 2003.

Jonathan B Thomas, Luca Antiga, Susan L Che, Jaques S Milner, Dolores A Hangan Steinman, J David Spence, Brian K Rutt, and David A Steinman. Variation in the carotid bifurcation geometry of young versus older adults implications for geometric risk of atherosclerosis. *Stroke*, 36(11):2450–2456, 2005.

K. Tsubota, S. Wada, and T. Yamaguchi. Particle method for computer simulation of red blood cell motion in blood flow. *Computer methods and programs in biomedicine*, 83(2):139–146, 2006.

SA Urquiza, PJ Blanco, MJ Vénere, and RA Feijóo. Multidimensional modelling for the carotid artery blood flow. *Computer Methods in Applied Mechanics and Engineering*, 195(33):4002–4017, 2006.

Sergei L Vasin, Igor A Titushkin, and Viktor I Sevastianov. Mathematical model of static platelet adhesion on a solid surface. *Journal of Biomedical Materials Research Part A*, 67(2):582–590, 2003.

A. Vázquez-Quesada and M. Ellero. Sph simulations of a viscoelastic flow around a periodic array of cylinders confined in a channel. *Journal of Non-Newtonian Fluid Mechanics*, 167-168:1–8, 2012. doi: 10.1016/j.jnnfm.2011.09.002.

Adolfo Vázquez-Quesada, Marco Ellero, and Pep Español. Consistent scaling of thermal fluctuations in smoothed dissipative particle dynamics. *The Journal of chemical physics*, 130:034901, 2009.

A Veneziani and C Vergara. Flow rate defective boundary conditions in haemodynamics simulations. *International Journal for Numerical Methods in Fluids*, 47 (8-9):803–816, 2005.

Irene E Vignon-Clementel, C Alberto Figueroa, Kenneth E Jansen, and Charles A Taylor. Outflow boundary conditions for three-dimensional finite element modeling of blood flow and pressure in arteries. *Computer methods in applied mechanics and engineering*, 195(29):3776–3796, 2006.

Wolfgang A Wall and Timon Rabczuk. Fluid–structure interaction in lower airways of ct-based lung geometries. *International Journal for Numerical Methods in Fluids*, 57(5):653–675, 2008.

D Keith Walters and William H Luke. A method for three-dimensional navier–stokes simulations of large-scale regions of the human lung airway. *Journal of Fluids Engineering*, 132(5):051101, 2010.

Thomas Werder, Jens H Walther, and Petros Koumoutsakos. Hybrid atomistic–continuum method for the simulation of dense fluid flows. *Journal of Computational Physics*, 205(1):373–390, 2005.

P. Worth Longest and C. Kleinstreuer. Comparison of blood particle deposition models for non-parallel flow domains. *Journal of biomechanics*, 36(3):421–430, 2003. ISSN 0021-9290.

Guohua Xia, Merryn H Tawhai, Eric A Hoffman, and Ching-Long Lin. Airway wall stiffening increases peak wall shear stress: a fluid–structure interaction study in rigid and compliant airways. *Annals of biomedical engineering*, 38(5):1836–1853, 2010.

WW Yan, B Cai, Y Liu, and BM Fu. Effects of wall shear stress and its gradient on tumor cell adhesion in curved microvessels. *Biomechanics and modeling in mechanobiology*, 11(5):641–653, 2012.

XL Yang, Y Liu, RMC So, and JM Yang. The effect of inlet velocity profile on the bifurcation copd airway flow. *Computers in biology and medicine*, 36(2):181–194, 2006.

Si Yong Yeo, Xianghua Xie, Igor Sazonov, and Perumal Nithiarasu. Geometrically induced force interaction for three-dimensional deformable models. *IEEE Transactions on Image Processing*, 20(5):1373–1387, 2011.

Youbing Yin, Jiwoong Choi, Eric A Hoffman, Merryn H Tawhai, and Ching-Long Lin. Simulation of pulmonary air flow with a subject-specific boundary condition. *Journal of biomechanics*, 43(11):2159–2163, 2010.

C.K. Zarins, D.P. Giddens, BK Bharadvaj, V.S. Sottiurai, R.F. Mabon, and S. Glagov. Carotid bifurcation atherosclerosis. quantitative correlation of plaque localization with flow velocity profiles and wall shear stress. *Circulation Research*, 53(4):502, 1983.

Xiaohui Zhang, Susan E Craig, Hishani Kirby, Martin J Humphries, and Vincent T Moy. Molecular basis for the dynamic strength of the integrin $\alpha$ 4 $\beta$ 1/vcam-1 interaction. *Biophysical journal*, 87(5):3470–3478, 2004.

Z Zhang and C Kleinstreuer. Transient airflow structures and particle transport in a sequentially branching lung airway model. *Physics of Fluids (1994-present)*, 14 (2):862–880, 2002.

Zhe Zhang, C Kleinstreuer, James F Donohue, and CS Kim. Comparison of micro- and nano-size particle depositions in a human upper airway model. *Journal of aerosol science*, 36(2):211–233, 2005.

C. Zhu. Kinetics and mechanics of cell adhesion. *Journal of Biomechanics*, 33(1): 23–33, 2000. ISSN 0021-9290.

C. Zhu, T. Yago, J. Lou, V.I. Zarnitsyna, and R.P. McEver. Mechanisms for flow-enhanced cell adhesion. *Annals of biomedical engineering*, 36(4):604–621, 2008.

# List of Figures

# Acronyms

**BBO** Basset-Boussinesq-Oseen.

**BC** Boundary condition.

**BFS** Backward-facing step.

**CAB** Carotid artery bifurcation.

**CFD** Computational fluid dynamics.

**CTC** Circulating tumor cell.

**DPD** Dissipative particle dynamics.

**DPM** Discrete particle model.

**EC** Endothelial cell.

**ECM** Extracellular matrix.

**ICAM-1** Intracellular adhesion molecule-1.

**IL-1** interleukin-1beta.

**ISPH** Incompressible smoothed particle hydrodynamics.

**LDL** Low density lipoprotein.

**LPT** Lagrangian particle tracking.

**MC** Monte Carlo.

**MCP-1** Monocyte-chemoattractive protein-1.

**OSI** Oscillatory shear index.

**RBC** Red blood cell.

**SDPD** Smoothed dissipative particle dynamics.

**SMC** Smooth muscle cell.

**SPH** Smoothed particle hydrodynamics.

**TNF** Tumor necrosis factor.

**VCAM-1** Vascular cell adhesion molecule-1.

**WBC** White blood cell.

**WSS** Wall shear stress.

**WSSG** Wall shear stress gradient.